Università degli Studi di Trieste

Dipartimento di Fisica
Corso di Laurea Magistrale in Fisica

REAL - TIME MONITORING IN HADRONTHERAPY

Measurement of Secondary Charged Particles Emitted by Oxygen Beams

Candidate:
Anna Baratto Roldán

Supervisor:
Prof. Giuseppe Battistoni
Co-supervisor:
Dr. Ilaria Mattei

Academic Year 2014–2015

Università degli Studi di Trieste

Dipartimento di Fisica
Corso di Laurea Magistrale in Fisica

MONITORAGGIO REAL - TIME IN ADROTERAPIA

Misura di Particelle Cariche Secondarie Emesse da Fasci di Ossigeno

Laureanda:
Anna Baratto Roldán

Relatore:
Prof. Giuseppe Battistoni
Correlatrice:
Dr. Ilaria Mattei

Anno Accademico 2014–2015

(...) porque ves allí, amigo Sancho Panza,
donde se descubren treinta o pocos más desaforados gigantes,
con quien pienso hacer batalla (...)

El Quijote (I, VIII)

Contents

Introduction

According to the estimates by the World Health Organization (WHO), cancer figures among the leading causes of mortality worldwide, with a number of new cases expected to rise by about 70% over the next two decades [1]. Although surgery is the most widespread treatment approach for the cure of solid tumours, approximately 2/3 of all patients diagnosed with cancer receive curative or palliative radiation treatments, most of the time performed with photon or electron beams. However, the rapid evolution experienced in recent years by radiation oncology techniques has led to the establishment of an alternative technique, *hadrontherapy* or *charged particle therapy*, which shows many advantages with respect to the traditional radiotherapy, especially for deep seated, solid and non moving tumours. Hadrontherapy exploits accelerated charged hadrons (from the greek *adrós*, strong), such as protons and heavier ions, for the treatment of both early and advanced solid tumours. Clinical interest in hadrontherapy resides in the fact that it is able to deliver precision treatment to tumours, taking advantage of the peculiar energy loss mechanism that characterises the interaction of protons and other ions with matter. Indeed, these particles have the typical feature of releasing almost all their energy at the end of their path in tissues, in correspondence to the so called Bragg peak position, making it possible to achieve a high irradiation accuracy and dose conformity while minimising the damage to surrounding healthy tissues and organs at risk.

In the last decade, hadrontherapy has gained a great interest in the medical community for its excellent clinical results, leading to the construction and installation of dedicated accelerators in hospital-based clinical centres around the world. Protons are by far the most largely used particles in hadrontherapy centres, followed by carbon ions. However, an intense discussion has arisen in recent years concerning the possibility of optimising the clinical potential of hadrontherapy by extending the spectrum of therapeutic ions beyond protons and carbon ions. Indeed, light ions, with respect to protons, are characterised by a higher biological effectiveness, strictly connected to the higher ionisation density induced by light ions in their slowing down path through matter. This leads to a higher capability of producing direct damages to the DNA of tumour cells, markedly increasing cell killing efficiency. On the other hand, with increasing mass of light ions, fragmentation occurs inside the patient, resulting in an unwanted dose tail behind the Bragg peak, which worsens the quality of the depth dose profile. Among the new ions proposed for hadrontherapy, helium and lithium have been considered in light of their improved lateral dose distributions compared with protons, while oxygen appears to be a good candidate for the irradiation of deep-seated hypoxic tumours, in combined treatments with photons or other ions. In view of their potential in improving radiation treatment effectiveness and selectiveness, experimental data on particles other than protons and carbon ions are needed, in order to consistently describe their physical and biological properties to a level of accuracy high enough to allow their clinical use.

Even if, nowadays, hadrontherapy has reached a good degree of perfection in clinical use, there is still large space for improvements in what concerns quality assurance and treatment planning verifications. Indeed, to fully take advantage of the improved spatial selectiveness of particle therapy, monitoring devices are necessary in order to provide high precision feedbacks on the position of the maximum dose release during the treatment. Unfortunately, standard radiotherapy monitoring techniques cannot be used in this context, since the fraction of primary beam transmitted through the patient is negligible. At present, existing techniques are based on the detection of different secondary particles produced in the beam interaction with matter: gammas from e^+e^- annihilation, prompt nuclear de-excitation gammas and charged particles. The latest, in particular, are the particles of interest of this thesis, which is part of a broader experiment that took place at the Heidelberg Ion Therapy Center (HIT) in Germany.

Among its many objectives, the experiment performed at HIT had the purpose of studying monitoring techniques in charged particle therapy, based on the detection of secondary particles emitted by helium, carbon and oxygen beams impinging on a tissue equivalent polymethyl methacrylate (PMMA) target. The aim of this thesis work is that of analyse secondary charged particles, mainly protons and other hydrogen isotopes, emitted by oxygen beams impinging on PMMA, detected at large angles with respect to the primary beam direction (90° and 60°). The longitudinal emission distribution of secondary charged particles is related to the energy deposited by oxygen ions inside the PMMA target, and to the Bragg peak position itself. The analysis performed in this thesis has focused on the evaluation of secondary proton production yields and on the calculation of some longitudinal distribution parameters to be correlated with the peak of the oxygen beam depth-dose distribution, in order to determine whether secondary charged products are feasible particles for the purpose of monitoring hadrontherapy treatments. Following this preliminary study, an experimental campaign should start in order to optimise a dedicated monitoring detector and find a valid parametrisation of the relation between emission profiles and the Bragg peak position, in order to apply this technique in clinical practice.

This thesis is divided in four chapters. In Chapter 1, the basics of radiation interaction with matter, for the particles of interest of this work, will be presented, followed by a description of the relevant radiobiological parameters for particle therapy as well as of the state of the art in hadrontherapy technology. Chapter 2 will be devoted to the description of secondary particles produced in hadrontherapy treatments, focusing on their detection techniques and potentialities for beam monitoring purposes. In Chapter 3 the set-up of the experiment performed at HIT will be presented, and a detailed description of the detectors of interest for the analysis of secondary charged particles will be given. Finally, Chapter 4 will be dedicated to the actual analysis carried out in this thesis project. The energy spectrum of secondary charged particles and secondary protons production yields have been measured. Furthermore, a clear correlation between charged particles longitudinal emission profiles and the Bragg peak position has been observed. Experimental results have been compared with a Monte Carlo (MC) simulation developed with the FLUKA Monte Carlo code.

Chapter 1

Principles of Hadrontherapy

Radiation therapy is a clinical practice that takes advantage of ionising radiation, such as photons, electrons, protons, light ions and neutrons, for the treatment of neoplastic diseases. The main goal of radiotherapy is therefore the treatment and cure of cancer pathologies which, according to the World Health Organization (WHO), are one of the major causes of death in the high-income countries, following cardiovascular diseases. Epidemiological data about mortality show that in the last years cancer-related deaths have been continuously decreasing for both men and women worldwide, as emerges from Figure 1.1.

These data reflect the progressive development experienced by diagnosis techniques and technologies in the treatment of many oncological pathologies, improvements that have led to a radical change of radiation therapy instrumentations and methods. Nowadays, nearly 2/3 of cancer patients receive radiation therapy during their illness, and for most cancer types treated with radiation therapy, at least 75% of the patients undergo radiotherapy with the intent to cure the cancer, rather than to control the growth or relieve symptoms like pain [3]. Nevertheless, radiation therapy is not the only clinical approach available for tumour cure, being surgery and chemotherapy equally important and widespread. Treatment options depend on the type of cancer, stage of development, cancer spread over the patient body and on the patient general health. Combined therapy modalities can also be applied: for example chemo-radiotherapy can be used to treat metastatic tumours, with which radiotherapy can't deal alone, while radio-surgery applications are mainly adopted to shrink the tumour volume before radiation or to reduce local relapse onset probability after operation.

Since the aim of each treatment modality is to kill as many cancerous cells as possible, while minimising the damage to healthy-tissue cells, sometimes surgery, as well as conventional radiotherapy, is not feasible due to the tumour localisation close to organs at risk. The *Intensity Modulated Radiation Therapy* (IMRT) is, at present, the pioneering technology in traditional radiotherapy with X-rays. IMRT is an advanced

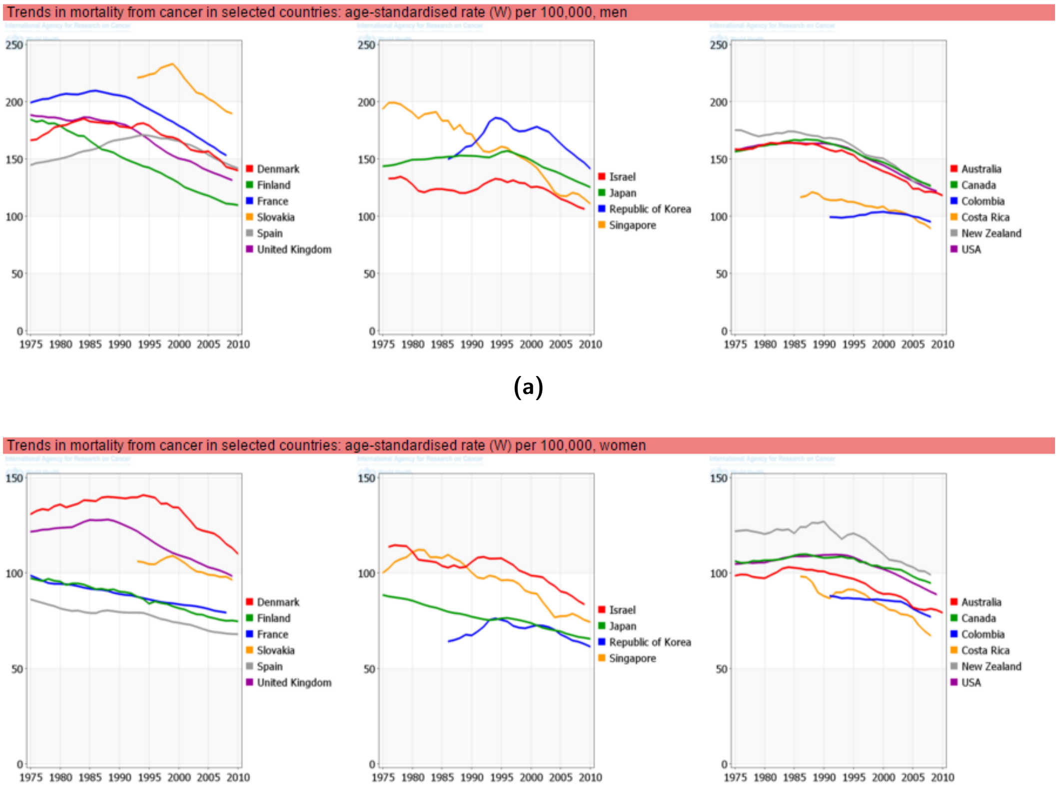

(a)

(b)

Figure 1.1: Trends in mortality from cancer in selected coutries for men (a) and women (b). [2].

mode of high-precision radiotherapy that allows for the radiation dose to conform more precisely to the three-dimensional shape of the tumour by modulating the intensity of the radiation beam in multiple small volumes [4]. Typically, combinations of multiple intensity-modulated fields coming from different beam directions produce a custom tailored radiation dose, that maximises tumour dose while minimising the dose to adjacent normal tissues. The impressive developments in technologies, encountered by conventional photon therapy in the improvement of target definition, meticulous treatment planning and highly accurate delivery systems, have stimulated in the last twenty years renewed interest in the use of particle beams for radiation therapy, which could not be fully exploited before these advances were achieved [5].

In 1946, accelerator pioneer Robert Wilson laid the foundation for hadrontherapy with his article in *Radiology* about the therapeutic interest of protons for treating cancer [6] and, less than ten years later, in 1954, the first treatments with protons took place in the Lawrence Berkeley Laboratory. Today, proton therapy has grown into an advanced, cutting-edge clinical modality: around 100 000 patients worldwide have been treated with protons since the establishment of the first hospital-based treatment centre in Loma Linda, California, in 1990, and more than 10 000 have been treated with heavier ions, generally carbon [7]. The benefits of hadrontherapy are based both on physical as well as biological reasons, as will be presented in the next sections, resulting in a more accurate and efficient irradiation of the tumour.

Generally, radiation therapy has two major goals: controlling disease and reducing side effects. In clinics, these goals are described by two curves, which determine the probability of success of a treatment: the *Tumour Control Probability Curve* and the *Normal Tissue Complication Probability Curve*, shown in Figure 1.2.

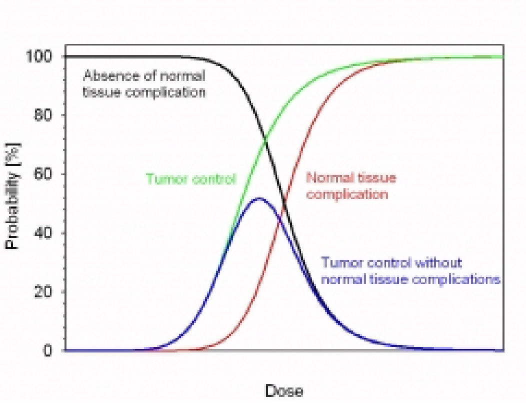

Figure 1.2: *Tumour Control Probability* (TCP - green) and *Normal Tissue Complication Probability* (NTCP - red). As TCP and NTCP increase with increasing dose, there is a dose range, or therapeutic window, where the probability for tumour control without complications (blue curve) reaches its maximum [8].

These curves usually have a sigmoidal shape, determined by tissue-dependent radiobiological factors, and the best radiation treatment should be the one that maximises the distance between them. The rationale to use hadrons for radiotherapy is precisely to achieve this goal, delivering the dose on the target volume with a much better localisation than with conventional therapy with electrons and photon beams. Indeed, clinical interest in hadrontherapy resides in the fact that it delivers precision treatments to tumours, exploiting the characteristic shape of the energy deposition as a function of depth of traversed matter for hadrons.

While X-rays lose energy slowly and mainly exponentially as they penetrate tissue, charged particles release more energy at the end of their path in matter, making it possible to target a well-defined region at a depth in the body that can be tuned by adjusting the energy of the incident particle beam. The high-dose region at the end of the particle range, visible in Figure 1.3, is known as the Bragg peak, and its characteristics will be described in Section 1.1.1.

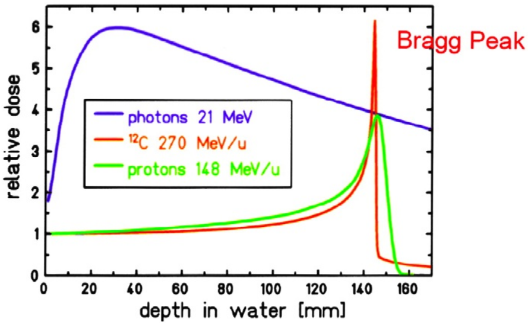

Figure 1.3: Depth dose distribution for photons and monoenergetic Bragg curves for carbon ions and protons [9].

1.1 Radiation interaction with matter

The phenomena associated with the radiation interaction in matter include a wide variety of physical effects, whose knowledge is of fundamental importance to allow the widespread of new techniques and applications. Indeed, the detailed study of these interactions and their properties constitutes the theoretical fundamental basis for designing novel radiation detection systems, optimizing radiation shielding material, implementing new radiation techniques for tumour treatments and many other applications.

Radiation interacts with matter in terms of its fundamental elements: atoms, nuclei and their individual constituents, with a probability that is governed by quantum mechanics and depends on radiation nature, energy and type of material. The processes corresponding to each type of radiation define its propagation through matter, its detection characteristics as well as its effects on biological organisms. The most common processes which take place when charged particles or photons pass through matter are the electromagnetic interactions. Particles heavier than electrons, which in the following will be pointed as heavy charged particles, will undergo energy losses mainly due to excitation and ionisation of atoms of the medium, close to their trajectory. Electrons and positrons will also lose energy by radiating photons. Finally photons can be fully absorbed in matter by a single scattering or by few subsequent interactions mainly governed by photoelectric effect, Compton scattering and pair production [10].

In this Section, the physical principles of the interaction of heavy charged particles with matter, relevant to therapeutic application, are discussed. Two are the main processes that characterise the passage of heavy charged particles through a material: energy loss and deflection from the particle original direction. Heavy charged particles interact with matter primarily through Coulomb forces between their positive charge and the negative charge of the electrons of the absorber atoms. Depending on the closeness of such interactions, the impulse felt by the electrons from the attractive Coulomb force may be sufficient either to raise the electron to a higher-lying shell within the atom (*excitation*) or to remove it completely from the atom (*ionisation*) [11]. In the slowing down process, the path of heavy charged particles tends to be quite straight and no significant deflections of the primary particle trajectory are observed, as the electron mass is much smaller than the heavy charged particle mass. This is no more true when heavy charged particles collide with the absorber nuclei, whose mass is much bigger. Although such interactions occur rarely, when they take place the target nucleus absorbs a very little amount of energy while the incident particle is scattered, causing a deflection of its trajectory that is anyhow confined to small angles. In any case, since heavy charged particles lose their energy almost entirely in the electron-collisions, which are statistical in nature, it is possible to define the average energy loss per unit path length, the so called *Stopping Power*.

1.1.1 The Bethe-Bloch formula and the Bragg Peak

Consider a heavy charged particle of charge ze and mass M which interacts with an atomic electron of mass m_e at some distance b from the particle trajectory, as shown in Figure 1.4. Assuming the particle velocity v to be greater than the electron orbital velocity, the bound atomic electron can be treated as free and initially at rest. Furthermore, the atomic electron only moves very slightly during the interaction, so that the electric field acting on it may be taken at its initial position. Finally, supposing $M \gg m_\mathrm{e}$, the momentum transfer can be assumed to be sufficiently small so that the heavy particle trajectory is essentially non-deviated from its original path [12].

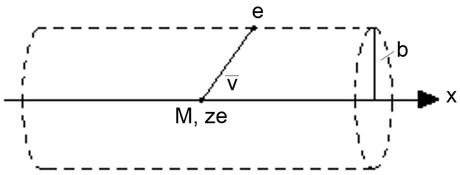

Figure 1.4: Collision of a heavy charged particle (M, ze, v) with an atomic electron (e) at a distance b [12].

With these approximations, we can obtain essentially the Bohr's classical formula, as calculated by Jackson [13], given by the following equation:

$$-\frac{\mathrm{d}E}{\mathrm{d}x} = \frac{4\pi z^2 e^4}{m_\mathrm{e} v^2} Z N_0 \ln \frac{\gamma^2 m_\mathrm{e} v^3}{z e^2 \overline{\nu}} \tag{1.1}$$

where E is the particle energy, x the particle's travelled distance in the medium and $\overline{\nu}$ indicates an orbital frequency averaged over all the bound states. $ZN_0 = ZN_\mathrm{A}\rho/A$

is the electron density, with N_A the Avogadro constant. Z and A are respectively the atomic and mass number, and ρ is the density of the absorber material. Finally $\gamma = (\sqrt{1-\beta^2})^{-1}$ is the Lorentz factor, where $\beta = v/c$ with v the particle velocity and c the speed of light.

Equation (1.1) gives a reasonable description of the energy loss for heavy charged particles such as the α-particles or heavier nuclei at sufficiently large β. However, for lighter particles, the formula breaks down because of quantum effects. The correct quantum-mechanical calculation was first performed by Bethe, Bloch and other authors, giving the following formula [14]:

$$-\frac{\mathrm{d}E}{\mathrm{d}x} = 2\pi N_\mathrm{a} {r_\mathrm{e}}^2 m_\mathrm{e} c^2 \rho \frac{Z}{A}\frac{z^2}{\beta^2}\left[\ln\left(\frac{2m_\mathrm{e}\gamma^2 v^2 W_\mathrm{max}}{I^2}\right) - 2\beta^2 - \delta - 2\frac{C}{Z}\right] \tag{1.2}$$

where $r_\mathrm{e} = e^2/(m_\mathrm{e}c^2)$ is the classical electron radius, I is the mean ionising potential of the target, W_max is the maximum energy transfer in a single collision, δ is the density effect correction and C is the shell correction. Equation (1.2) is commonly known as the Bethe-Bloch formula, and is the basic expression used for energy loss calculations. The density effect correction δ and the shell correction C intervene at high and low energy respectively. The density effect originates from the electric field produced by the heavy charged particle, which tends to polarise the electrons of the medium along its path. This effect increases with the increasing of particle energy, meaning that further electrons will feel a shielded electric field and give a lower contribution to the energy loss. Figure 1.5 shows a comparison of the Bethe-Bloch formula with and without density correction. The shell correction, instead, arises for low energies of the incident particle, when the assumption of free and initially at rest atomic electrons is no more valid. In this energy region, many complex phenomena take place, the most important of them being the electronic capture by the incident particle, which determines a decrease of its charge and consequently of its stopping power. For very low energies, below about $10\,\mathrm{MeV\,u^{-1}}$ for light ions, the corrections to the Bethe-Bloch are no more valid, and an effective charge Z_eff has to be introduced. To extend the validity of the Bethe-Bloch to the low energy region, *Barkas* [15] proposed a parametrisation of Z_eff as a function of β and Z of the incident particle, given by the following empirical formula:

$$Z_\mathrm{eff} = Z[1 - \exp(-125\beta Z^{-2/3})]. \tag{1.3}$$

Ignoring the logarithmic dependence of the stopping power on I and assuming no changes on the medium parameters, Equation (1.2) appears as an universal function of the "velocity" $\beta\gamma$, due to the independence of $-\mathrm{d}E/\mathrm{d}x$ from the mass of the

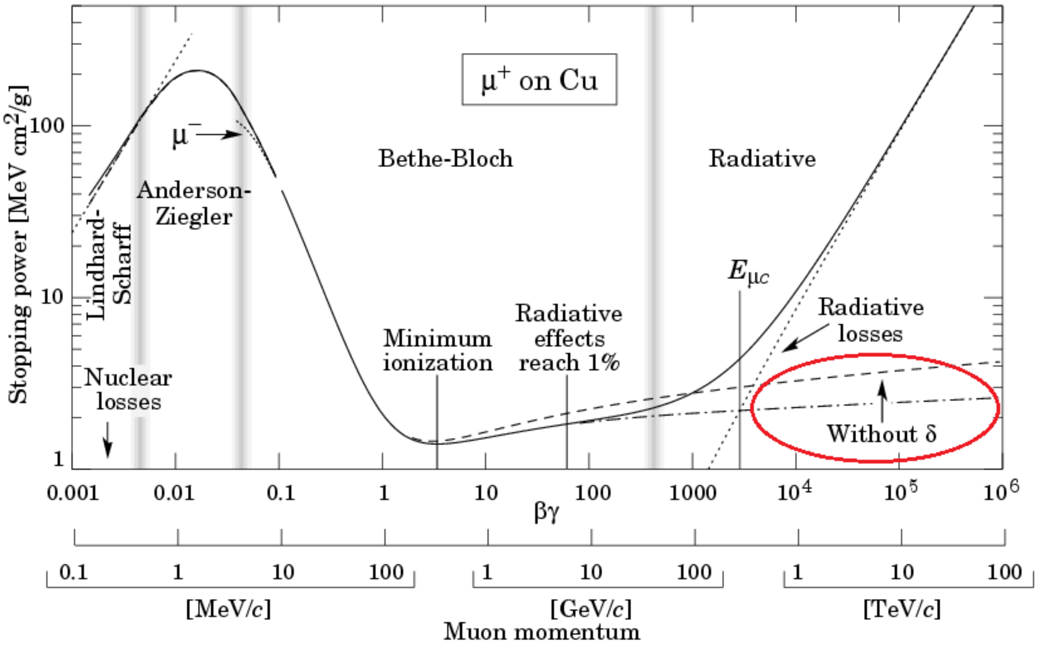

Figure 1.5: Example of Stopping Power distribution as a function of the energy. The dotted part on the right indicates the behaviour of $-\mathrm{d}E/\mathrm{d}x$ for heavy charged particles, with or without density correction.

incident particle. Furthermore, it should be noticed that:

- For small values of β the energy loss is dominated by the multiplicative factor $1/\beta^2$ until a minimum is reached. After the minimum, when $\beta \rightarrow 1$ and $\beta\gamma > 1$, the energy loss grows again logarithmically as $\ln \gamma^2$.
- The energy loss corresponding to the minimum of the stopping power distribution normalised to the material density is equal to $1 \div 2\,\mathrm{MeV\,g^{-1}\,cm^2}$. At this point, particles are usually referred to as *Minimum Ionising Particles* or MIP.
- When comparing different charged particles of the same velocity, the only factor that may change is z^2, which occurs in the numerator of the expression. Therefore, particles with the greatest charge will have the largest specific energy loss.

Taking into account the aforementioned considerations, as a heavy charged particle slows down inside matter, its rate of energy loss will change, determining a greater amount of energy deposited per unit length at the end of its path rather than at its beginning. This effect is shown in Figure 1.6, which represents the amount of energy deposited by a heavy charged particle as a function of its position along its slowing-down path. The maximum energy-loss rate is reached at a projectile velocity of:

$$\beta \approx Z^{2/3}\beta_0 \tag{1.4}$$

where $\beta_0 = e^2/\hbar c = 1/137$ is the Bohr velocity. From Equation (1.4), it emerges that the energy corresponding to the maximum energy deposition depends only on the charge of the incident particle. For ^{12}C ions, for example, this maximum occurs at a specific energy of $\approx 350\,\mathrm{keV\,u^{-1}}$. The curve depicted in Figure 1.6 is known as *Bragg Curve* and its maximum is usually indicated as *Bragg Peak* (BP).

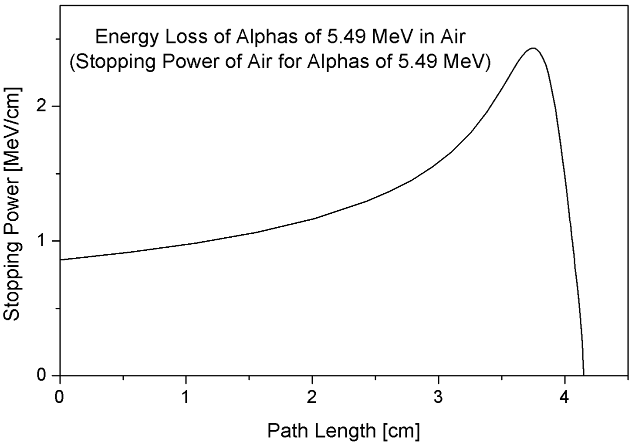

Figure 1.6: A typical Bragg curve, showing the variation of $-\mathrm{d}E/\mathrm{d}x$ as a function of the penetration depth for 5.49 MeV α particles in air.

When the energy of the incident particle slows down under $10\,\mathrm{keV\,u^{-1}}$, interactions with atomic nuclei start to become relevant. This effect is known as *Nuclear Stopping Power*, and is outlined with dotted lines in Figure 1.7.

In the clinical practice, the aim is usually to obtain an irradiation profile broader than the individual Bragg peak, in order to achieve a better coverage of the tumour volume. This is done superimposing different beams with slightly different energies and weights, as depicted in Figure 1.8, generating a *Spread out Bragg Peak* (SOBP) that deposits the required dose in the treatment volume (see Section 1.2.1 for the definition of the dose).

1.1.2 Range and energy straggling

The peculiar shape of the stopping power distribution as a function of the material penetration depth has led to the conception, and later on the development, of hadrontherapy as a technique in cancer research and therapy. Since the specific ionisation is many times lower where the heavy charged particles enter the tissue than in the last centimetres of the path, the exact knowledge of the total penetration

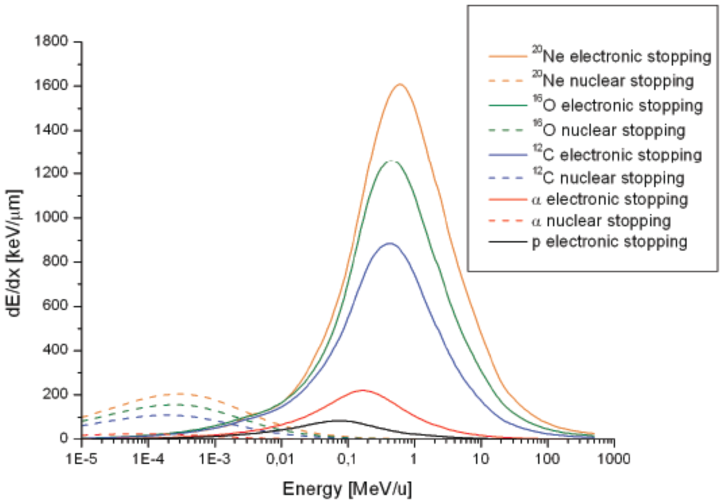

Figure 1.7: Electronic energy loss (continuous line) and Nuclear energy loss (dotted line) for different ions in water [16]. dE/dx values have been calculated with the SRIM code [17].

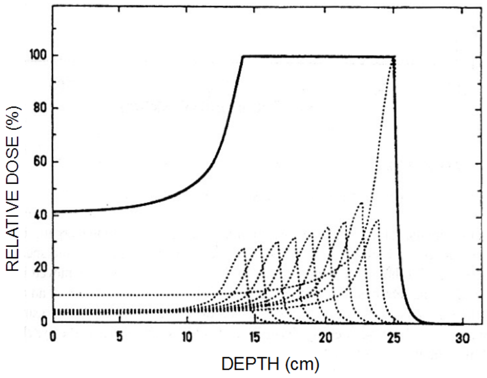

Figure 1.8: Example of the method of summing different Bragg peaks with different energies and weights, to form the *Spread Out Bragg Peak* or SOBP.

depth should allow to perform precision exposures of well defined small volumes within the body [6]. The key aspect of this innovative technique is therefore the precise knowledge of the beam *range*, a distance beyond which no primary particle will penetrate.

Assuming the energy loss to be continuous, this distance should be a well defined number, the same for all identical particles with the same initial energy in the same medium. Experimentally, the range can be determined measuring the ratio of transmitted to incident particles (I/I_0), coming from a mono-energetic and collimated beam impinging on different thickness of the same material. A typical curve, depicted in Figure 1.9, shows this ratio as a function of the absorber thickness.

Figure 1.9, however, indicates that the ratio I/I_0 does not drop immediately to zero, as expected from a well defined quantity, but it slopes down within a certain

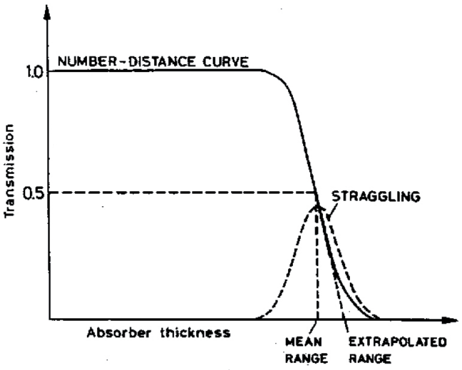

Figure 1.9: Typical curve of the ratio I/I_0 as a function of the absorber thickness. The distribution of ranges is approximately Gaussian in form. The mean and extrapolated ranges are highlighted.

thickness interval. This behaviour, known as *Range Straggling*, is due to the fact that the energy loss has a statistical nature, which leads to an approximately Gaussian distribution of the range. As shown in Figure 1.10, the range straggling is responsible for the broadening of the Bragg peak, and for the reduction of its height.

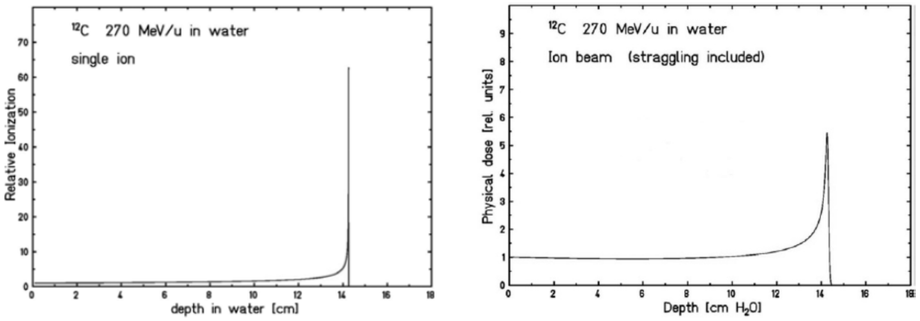

Figure 1.10: Dose deposition by a carbon ion beam impinging on water without (left) and with (right) energy straggling [18].

Bearing in mind the previous considerations and considering the hypothesis of Continuous Slowing Down Approximation (CSDA), from a theoretical point of view the mean range $R(E_0)$ of an incident particle with energy E_0 can be calculated integrating the Bethe-Bloch formula as follows:

$$R(E_0) = \int_0^R \mathrm{d}x(E) = \int_{E_0}^0 \frac{\mathrm{d}x}{\mathrm{d}E}\,\mathrm{d}E = \int_{E_0}^0 \left(\frac{\mathrm{d}E}{\mathrm{d}x}\right)^{-1} \mathrm{d}E. \tag{1.5}$$

Since energy and range are strictly related, the range straggling problem may be faced from a different point of view: instead of observing the fluctuations of a path-length as a function of crossed material thickness for a fixed energy loss, we may observe the fluctuations in energy loss for a fixed thickness of absorber. For any given particle, in fact, the amount of energy lost will not, in general, be equal to its mean value due to the statistical fluctuations in the number of collisions and in the energy transferred. These fluctuations are described by the asymmetric Vavilov distribution [19], which is characterised by a long tail deriving from the non zero probability of having large energy transfers in a single collision. For relatively thick absorbers, in the limit of many collisions, the Vavilov energy loss distribution can be easily shown to become a Gaussian, following the statement of the *Central Limit Theorem* in statistics. Assuming the number N of the primary ion collisions to be big enough, the distribution of the energy loss will have the following shape:

$$f(\Delta E) \propto \exp\left[\frac{-(\Delta E - \overline{\Delta E})^2}{2\sigma_{\mathrm{E}}^2}\right] \tag{1.6}$$

where ΔE is the energy lost, $\overline{\Delta E}$ is the mean energy loss and $\sigma_{\mathrm{E}}^2 = \alpha x$ is the variance, which is proportional to the thickness of traversed matter x. According to *Bohr* [20], α does not depend on the particle velocity, being $\alpha = 4\pi Z^2 e^4 n$ with Z the particle charge and n the number of electrons per unit volume. Since, in principle, range straggling imposes a limit on the accuracy with which the particle energy can be determined from its range [21], the variance σ_{R}^2 of the range distribution is related to the variance σ_{E}^2 of the energy loss straggling distribution. Taking into account Lindhard and Scharff relativistic corrections, range variance is given by the following formula:

$$\sigma_{\mathrm{R}}^2 \propto \alpha \int_0^{E_0} \left(\frac{\mathrm{d}E}{\mathrm{d}x}\right)^{-3} \frac{1-\beta^2/2}{1-\beta^2}\,\mathrm{d}E \tag{1.7}$$

where β is the particle velocity and E_0 is the particle initial energy. Therefore, a measure of the range straggling can be obtained from the ratio of the square root of the range variance σ_{R}^2 by the mean range R (see Equation (1.5)). This ratio is nearly constant and can be described by [22]:

$$\frac{\sigma_{\mathrm{R}}}{R} = \frac{1}{\sqrt{M}} f\left(\frac{E_0}{Mc^2}\right) \tag{1.8}$$

where f is a slowly varying function depending on the absorber [23] and E_0 and M are the particle energy and mass.

Table 1.1 collects the computed range and range straggling in water for some ions interesting for therapeutic purposes. These values have been calculated with the SRIM code [17], which computes the projected range, i.e. the CSDA range projected on a straight line corresponding to the particle direction.

Table 1.1: Projected range R_P and longitudinal straggling $\sigma_\mathrm{R}^\mathrm{P}$ in water for some ions potentially applicable in hadrontherapy. Values have been calculated with the SRIM code (2013). The range of different particles having the same energy scales with a factor A/Z^2, therefore hydrogen and helium ions have almost the same range in water.

Ion	50 MeV/u		100 MeV/u		150 MeV/u		200 MeV/u	
	R_P (cm)	$\sigma_\mathrm{R}^\mathrm{P}$ (cm)	R_P (cm)	$\sigma_\mathrm{R}^\mathrm{P}$ (cm)	R_P (cm)	$\sigma_\mathrm{R}^\mathrm{P}$ (cm)	R_P (cm)	$\sigma_\mathrm{R}^\mathrm{P}$ (cm)
^{1}H	2.19	0.09	6.8	0.3	14.0	0.6	23.1	0.9
^{4}He	1.97	0.07	6.9	0.3	14.1	0.6	23.2	0.9
^{12}C	0.67	0.03	2.33	0.09	4.8	0.2	7.8	0.3
^{16}O	0.49	0.02	1.72	0.06	3.5	0.2	5.8	0.2

1.1.3 Multiple Coulomb Scattering

While the depth of the Bragg peak depends on the particle initial energy, its width is modulated by the energy dispersion in both the longitudinal and the transverse direction. The first is due to the energy straggling, as described in Section 1.1.2, while the second is mainly due to the elastic Coulomb collisions experienced by the primary particles when impinging into the target nuclei. Neglecting spin effects and screening, these collisions are individually governed by the well known Rutherford formula for the differential cross section of the elastic Coulomb interaction:

$$-\frac{\mathrm{d}\sigma}{\mathrm{d}\Omega} = {Z_\mathrm{p}}^2 {Z_\mathrm{t}}^2 {r_\mathrm{e}}^2 \frac{(m_\mathrm{e}c/\beta p)^2}{4\sin^4\left(\dfrac{\theta}{2}\right)} \tag{1.9}$$

where Z_p and Z_t are respectively the particle and target atomic numbers, p is the momentum of the incident particle and θ is the scattering angle with respect to the beam direction. Equation (1.9) shows that the cross section grows with the square power of the charge of the incident particle, while it decreases inversely with the energy. Furthermore, assuming the target nuclei mass to be much greater than the incident particle mass, the majority of such elastic scattering results in small angular deflections, due to the $\sin^{-4}(\theta/2)$ dependence. When the average number of collision is $N > 20$, and the energy loss is small or negligible, the problem of Coulomb scattering can be treated statistically to obtain the probability distribution for the net deflection angle as a function of the thickness of crossed material. This is what is generally known as *Multiple Coulomb Scattering*.

The angular distribution of particles traversing a medium of thickness d has been described by Molière in the small-angle approximation, generally valid for all particles up to angles of $\theta \simeq 30°$ [12]. In the formulation by Molière, the polar angle distribution is expressed as a series. If the target thickness is big enough, in the first approximation, the greater order terms of this series may be excluded, and the angular distribution function is approximately Gaussian in form:

$$P(\theta)\mathrm{d}\Omega \simeq \frac{2\theta}{\langle\theta^2\rangle}\exp\left(\frac{-\theta^2}{\langle\theta^2\rangle}\right)\mathrm{d}\theta \tag{1.10}$$

where the parameter $\langle\theta^2\rangle$ represents the variance of the scattering angle distribution, being $\sqrt{\langle\theta^2\rangle}$ the RMS of the scattering angle (σ). A better estimation of this quantity, however, is obtained using the empirical formula proposed by *Highland* [24], which is valid for target atomic numbers $Z > 20$ and for target thickness $10^{-3}L_{\mathrm{rad}} < d < 10L_{\mathrm{rad}}$:

$$\sigma = \frac{14.1\,\mathrm{MeV}}{p\beta c}Z\sqrt{\frac{d}{L_{\mathrm{rad}}}}\left(1+\frac{1}{9}\log_{10}\frac{d}{L_{\mathrm{rad}}}\right). \tag{1.11}$$

In this formula, L_{rad} is the material radiation length, d the material thickness and p the particle momentum.

Equation (1.11) tells us that, independently of their mass, particles with the same kinetic energy, which can be derived from $p\beta c$, undergo the same deflection. At the same time, the term $p\beta c$ in the denominator of Equation (1.11) influences the behaviour of the lateral spread, which grows inversely with the energy. This is of particular importance for the purpose of hadrontherapy, where the smaller lateral dispersion of heavier ions, as shown in Figure 1.11, determines a better control of the dose distribution.

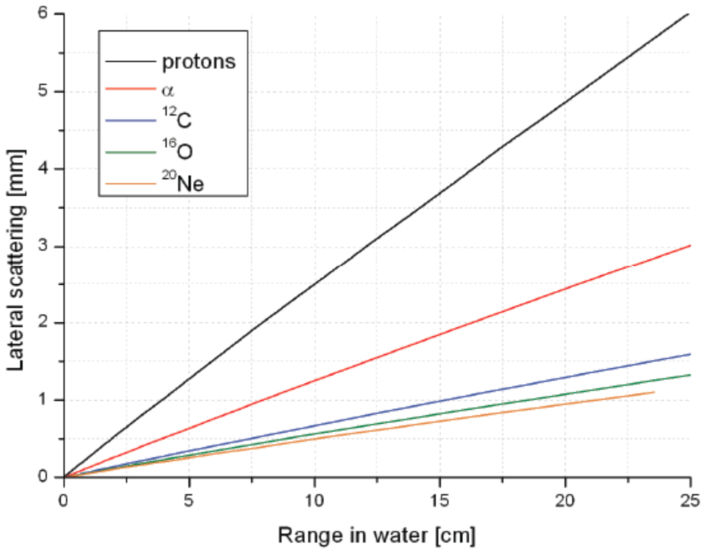

Figure 1.11: Lateral dispersion for some potentially therapeutic ions with the same range in water [16]. Values have been calculated with the SRIM code [17].

Finally it might be noticed that, in a statistical process, high deflections due to a single scattering are not excluded: they are visible as non-Gaussian tails of the distribution.

1.1.4 Nuclear interactions

Up to now only the electromagnetic aspects of the interaction between ions and matter have been considered. Even if the probability of nuclear reactions is much smaller than the probability of collisions with atomic electrons, it leads to significant effects at large penetration depths, that must be taken into account. Furthermore, these interactions are highly relevant for the development of range verification methods [25], as will be described in Chapter 2. Two qualitatively different types of collisions can be clearly distinguished:

- Elastic collisions: these interactions are not very frequent and conserve kinetic energy. They are similar to multiple Coulomb scattering, leading to a certain amount of beam broadening.
- Inelastic collisions: these interactions do not conserve kinetic energy. They may result in partial fragmentation or in a complete disintegration of both projectile and target nuclei.

A complete and satisfactory analytical model of nuclear interactions does not exist. However, many numerical models have been proposed, which can be used to develop Monte Carlo simulations. Since these nuclear interaction models show some differences for protons and heavier ions, it is better to discuss the two cases separately.
The many processes that take place following a **proton** interaction with the atomic nucleus can be modelled as a sequence of three stages [26], schematically displayed in Figure 1.12:

1. (Generalised) Intra-Nuclear Cascade (INC). This model is commonly used to describe nuclear interactions of nucleons with energies above 50 MeV to hundreds of GeV. It is based on the assumption that the incident particle interacts with quasi-free nucleons in the target nucleus, which is modelled as a cold Fermi gas of nucleons. Therefore, free nucleon-nucleon cross sections are used for calculations, being the Pauli principle the only incorporated quantum-mechanical concept. This "free" nucleon approach is valid as long as the wavelength associated to the incident particle motion is smaller than the average distance between neighbouring nucleons, and also much shorter than the mean free path inside the target nucleus. Furthermore, collisions must take place independently, meaning that the time between collisions has to be greater

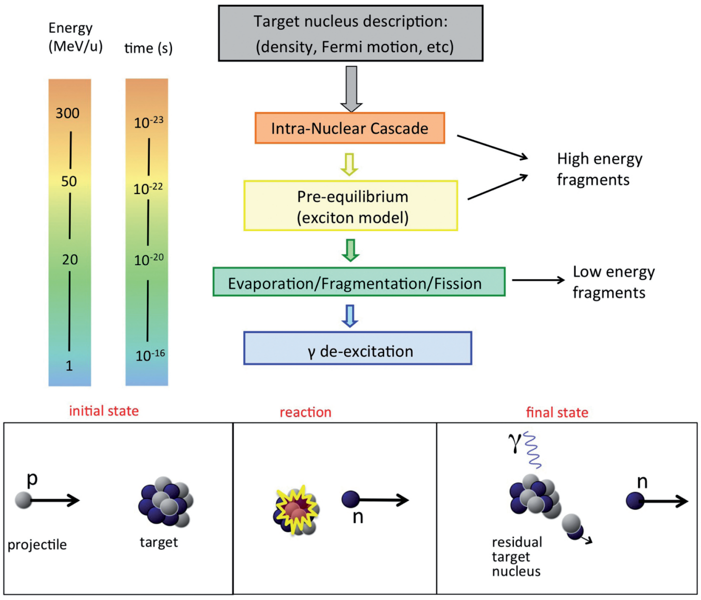

Figure 1.12: Top: relevant stages for radiotherapy of a modelled nucleon-nucleus interaction, together with time scale and energy of interacting particle. Bottom: sketch of a possible nucleon-nucleus reaction in proton therapy [25].

than the time in which a collision happens. Once a nuclear interaction happens, a certain number of final state particles is produced inside the nucleus. These high energy "secondaries" can scatter again in the same nucleus or escape, through a process called intra-nuclear cascade.

2. Pre-equilibrium. When all the interacting nucleons reach energies below 50 MeV the INC step ends. At this stage, a few particles may have been emitted, and the nuclear configuration is not yet in thermal equilibrium. The pre-equilibrium process is described as a chain of steps in which successive nucleon-nucleon collisions occur within a particle-hole, or exciton, state. In this formalism, the residual excitation energy is partitioned among the nucleons, which are excited from within the Fermi sea leaving a hole. Therefore, protons, neutrons and light fragments are emitted until the excitation energy decreases below any emission threshold.

3. De-excitation. At the end of the pre-equilibrium stage, the residual nucleus is left in an equilibrium state in which the remaining excitation energy is shared by a large number of nucleons. Depending on the mass of the target nucleus and on the energy left, the following processes might take place:

    - Nuclear evaporation: emission of light fragments, with kinetic energies of a few MeV, following a process similar to the evaporation from a hot system.

- Fission: breakage of the excited nucleus into two fragments. Applies only to high Z nuclei (roughly $Z \geq 65$) which are not found in human body apart from implants.
- Fermi-breakup: if the excitation energy is larger than the binding energy of some fragmentation channels, the nucleus disassembles into smaller fragments. This mechanism applies to light nuclei (usually $A \leq 16$).
- Gamma emission: the energy left after the previous stages is given off through the emission of γ rays.

The first two steps have a time scale of the order of 10^{-22} s and are referred to as "dynamic" stages. The last step has a time scale of about $10^{-18} - 10^{-16}$ s, and is referred to as "slow".

When considering nuclear interactions concerning **heavy ions**, the fundamental difference is that the incoming nucleons are not free. Physical models describing nucleus-nucleus interactions are mainly variants of the "abrasion-ablation" model [27] [28], schematically shown in Figure 1.13. In the first step (abrasion), the composition of the reaction partners may be modified in the overlapping interaction zone introducing a certain amount of excitation energy. Therefore, an excited quasi-projectile (fireball) with much of the initial velocity, a quasi-target fragment at rest and several excited light fragments are formed. In the second step the remaining projectile and target de-excite, converting the excess of energy in the ways already described for proton interactions. It must be noticed that, in this case, both target an projectile nuclei can lead to the production of fragments.

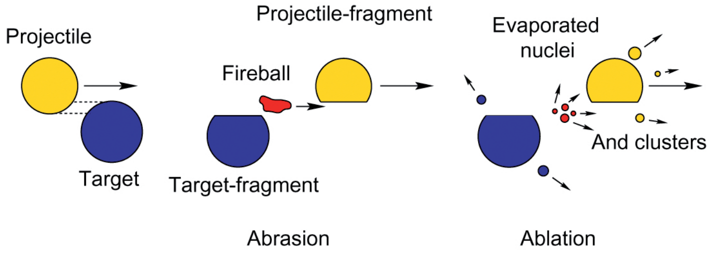

Figure 1.13: Simplified model of the nuclear fragmentation due to peripheral collisions of projectile and target nucleus [29].

Some important conclusions can be drawn for the effects of fragmentation relevant to radiotherapy with high energy ion beams [22]:

- Nuclear fragmentation reactions lead to an attenuation of the primary beam flux and a build-up of lower Z fragments, these effects becoming more and more important with increasing penetration depth.

- The secondary projectile-like fragments are moving with about the same velocity as the primary ions. They have in general longer ranges, as the range of particles scales with A/Z^2, and produce a dose tail beyond the Bragg peak.
- The angular distributions of fragments are determined by kinematic relations: projectile-like fragments appear forward peaked in the laboratory frame, target-like fragments are emitted isotropically and particles ablated from the fireball cover the range in between. Finally the lateral spread of secondary products produced by nuclear reactions appears to be much broader than the dispersion caused by the Multiple Coulomb Scattering.

1.2 Biological effects

As already discussed in Section 1.1, high energy protons and carbon ions exhibit a depth-dose profile which allows for increased energy deposition with penetration depth. In addition, heavy ions offer an even larger biological effectiveness for tumour treatments, due to enhanced ionisation density in the individual tracks of the heavy particles. Since the capabilities of radiations to destroy a tumour are related to the induced biological damage in cancer cells, some basic concepts about radiobiology need to be introduced.

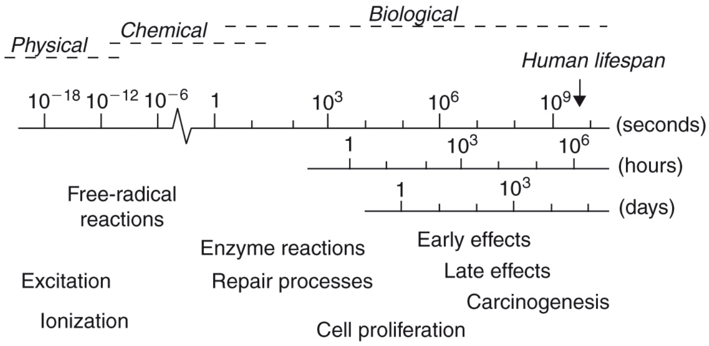

Figure 1.14: Time-scale of the effects of radiation exposure on biological systems [30].

The irradiation of any biological system generates a succession of processes that differ enormously in time-scale [30]. This is illustrated in Figure 1.14, in which these processes are divided into three phases:

- **Physical Phase**

  During the physical phase, charged particles interact with the atoms and molecules of which the tissue is composed. A high-speed electron, for example, takes about 10^{-18} s to traverse the DNA molecule and about 10^{-14} s to pass across a mammalian cell, inducing ionisation or excitation of the atoms.

- **Chemical Phase**

  The chemical phase describes the period in which damaged atoms and molecules react with other cellular components in rapid chemical reactions. ionisation and excitation lead to the formation of highly reactive molecules known as free radicals.

- **Biological Phase**

  The biological phase includes all subsequent processes: the vast majority of lesions are successfully repaired, while some rare lesions fail to be repaired and may eventually lead to cell death. At later times the so-called late reactions appear, which may finally lead to the formation of second tumours.

In the first step, during the physical phase, radiation can ionise biological cells in two different ways: indirectly or directly, as depicted in Figure 1.15. In the former case, ionising radiation interacts with water molecules inside the tissue, producing free radicals. These can diffuse throughout the tissue and react with the DNA or other molecules of the cell, damaging them. In the latter case, the DNA of the exposed cell is directly ionised, inducing a more severe damage. In both situations the DNA appears to be the principal target for radiation induced cell killing, due to its central role in all cellular functions, such as cell division and gene expression. Because of the importance of DNA, cells and organisms have developed a complex series of processes and pathways for DNA-damage repair. Specialised repair systems have therefore evolved for detecting and repairing damage to bases, Single-Strand Breaks (SSB) and Double-Strand Breaks (DSB), the latest being the most difficult and error-prone damages to repair. The main radiobiological difference between photons and heavy ions lies in their different direct ionisation capability: while photon ionisation density can be assumed to be homogeneous, heavy ion ionisation density is very localised. This implies a higher probability, with respect to photons, for double-strand breaks, inducing a more severe damage to the cell.

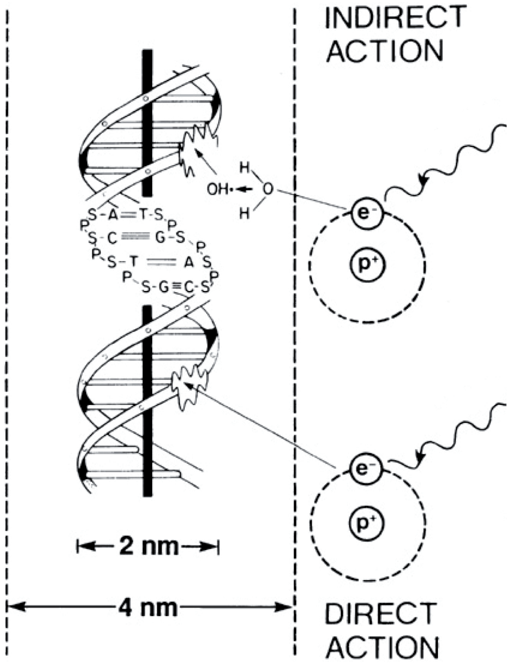

Figure 1.15: Direct and indirect radiation-induced damage to the DNA double-helix.

1.2.1 Absorbed dose and radiation damage

To characterise the amount of radiation-induced damage during a radiotherapy treatment, one of the most important physical quantities is the dose deposited in tissues. The *absorbed dose* is defined as the mean energy $\mathrm{d}E$ deposited by ionising radiation in a mass element $\mathrm{d}m$:

$$D = \frac{\mathrm{d}E}{\mathrm{d}m} \tag{1.12}$$

The International System unit for the absorbed dose is the Gray (Gy), where $1\,\mathrm{Gy} = 1\,\mathrm{J\,kg^{-1}}$. The absorbed dose, though, is not enough to determine the biological effect of different radiation qualities, as the most striking difference between photons and ions concerns their microscopic spatial energy distribution. A physical quantity which better describes the radiobiological effect of different types of radiation is the *Linear Energy Transfer* or LET. From a practical point of view, the linear energy transfer is the same as the stopping power, but focuses on the energy locally given to the medium, rather than on the energy loss by the incident particle. The LET is defined as the energy deposited in the target medium by a slowing-down particle, measured in $\mathrm{keV\,\mu m^{-1}}$:

$$\mathrm{LET}_{\Delta} = \left(\frac{\mathrm{d}E}{\mathrm{d}l}\right)_{\Delta} \tag{1.13}$$

In Equation (1.13) $\mathrm{d}E$ is the energy locally deposited by a charged particle in a track-segment of length $\mathrm{d}l$. In some practical cases it can be useful to exclude interactions that carry energy far away from the original track, imposing an upper threshold Δ for the energy of secondary electrons. This is usually referred as *Restricted* LET. If the threshold tends to infinity, the quantity is called *Unrestricted* LET and it equals the electronic stopping power.

The secondary electrons produced in the Coulomb interaction of the heavy ions with the target are defined as δ-rays. Those liberated electrons are scattered and subsequently transported in the medium by elastic and inelastic collisions, possibly generating further excitations and ionisations. Most of the induced secondary electrons deposit the dose in the center of the primary ions tracks, whose typical diameter is on the order of nanometres. As shown in Figure 1.16, this leads to a larger probability of correlated nearby DNA damages like single or double-strand breaks, inducing the increased heavy ion cell killing capability.

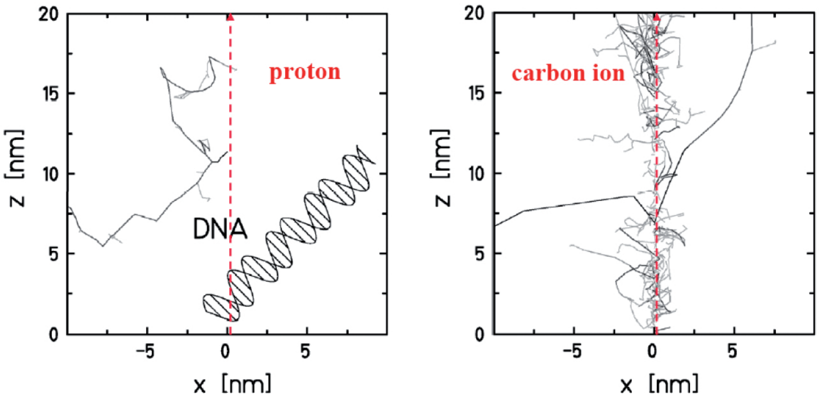

Figure 1.16: Structure of a proton and a carbon ion track in nanometre resolution compared with a schematic representation of a DNA molecule. The higher density of secondary electrons produced by carbon ions creates a larger amount of clustered DNA damage with respect to protons [31].

1.2.2 Surviving curves and Relative Biological Effectiveness

As indicated in Section 1.2.1, for high-LET radiation the contribution to the total damage induced by direct hits to the DNA is slightly increased. A common way to analyse the different effects of photons and heavy ions is by means of cell survival curves.

A cell survival curve describes the relationship between the radiation dose and the proportion of cells that survive. The word *survival* may mean different things in different context, and usually refers to the preservation of a specific function depending on the cell type. For proliferating cells, the ability of maintain their reproductive integrity is an appropriate definition. Experiments on cell survival are relatively easy to perform: cells from an actively growing stock culture are irradiated and then incubated for 1 or 2 weeks before being fixed and stained [32]. Then cell proliferation is analysed, counting as survivors only those cells which have formed colonies with more than 50 daughter cells. Finally the surviving fraction is given by normalisation to the number of seeded cells.

Survival curves are usually presented with the dose plotted on a linear scale and the surviving fraction on a logarithmic scale, as shown in Figure 1.17. At low doses, for low-LET radiations, the survival curve starts with a finite initial slope, then bends for higher doses and finally straightens again at very high doses. By contrast, for densely ionising or high-LET radiations, the cell survival curve is a straight line from the origin. Therefore, the most common way to parametrise the cell survival curve is by means of an exponential function theorised in the frame of the *Linear Quadratic* (LQ) model.

$$S(D) = \exp(-\alpha D - \beta D^2) \tag{1.14}$$

where S is the survival fraction, D is the absorbed dose and α and β are experimentally determined parameters. The LQ model assumes that there are two components to cell killing by radiation, respectively proportional to the dose and to the square of the dose, which in some way depend on the severity of DNA damage. The ratio α/β determines the shoulder of the survival curve, i.e. the radiation sensitivity, and corresponds to the dose at which the linear and quadratic contributions to cell killing are equal. Even if the LQ model is rather accurate in the classical dose range of conventional radiotherapy, the picture just presented is greatly simplified, and a universal theory of radiation cell killing is not yet available [33].

As already stated in Section 1.2.1, and clearly shown in Figure 1.17, biological effects of irradiation cannot be predicted only by means of the absorbed dose. A coefficient of *Relative Biological Effectiveness*, or RBE, needs to be introduced in order to take into account the differences in the effect of various types of radiation for the same physical dose. The RBE is defined as the ratio between the absorbed dose of a reference radiation (typically X-rays) and that of the test radiation (for example heavy ions) required to produce the same biological effect (isoeffect):

$$\mathrm{RBE_{iso}} = \left.\frac{D_{\mathrm{ref}}}{D_{\mathrm{test}}}\right|_{\mathrm{iso}} . \tag{1.15}$$

Typically, the RBE is determined from cell survival curves, using for example the 10% survival fraction as isoeffect for cell inactivation, as depicted in Figure 1.17.

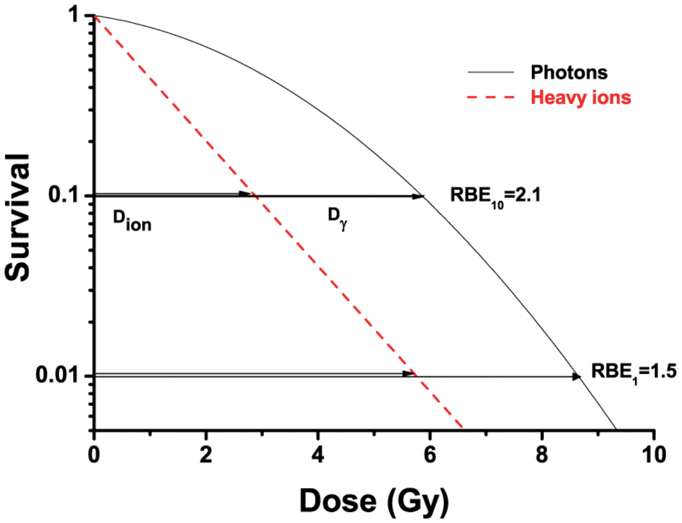

Figure 1.17: Survival curves for photons (solid black line) and heavy ions (red dashed line) and determination of RBE for cell inactivation [22].

In spite of its simple definition, the RBE is a very complicated radiobiological concept, which depends on several factors and variables.

Dependencies of RBE

While in proton therapy the low LET of protons allows the application of a single RBE factor throughout the entire radiation field, the situation in heavy-ion therapy is much more complex because of the large variations of LET. As emerges from Figure 1.18 the RBE increases with LET up to an ion-dependent maximum value, and then decreases for higher LET values.

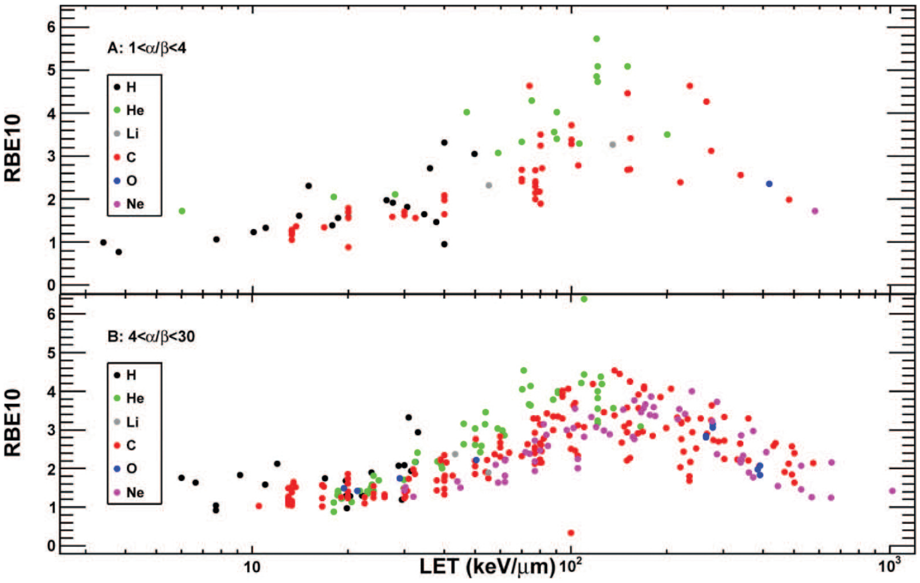

Figure 1.18: RBE at 10% survival of different monoenergetic particle beams as a function of LET, grouped in different sensitivity ranges (α/β) [35].

In fact, at a certain LET value, a single-particle traversal is sufficient to reduce cell survival probability, making further ionisations unnecessary. Moreover, the particle type influences the position of the RBE maximum, which is shifted toward higher LETs for heavier particles. Following the shape of the stopping power distribution as a function of the energy, for the same LET value, carbon ions appear to be much faster than protons, resulting in broader tracks with a reduce ionisation density in the track center. Therefore, for the same LET, the biological damage of carbon ions is smaller than for protons.

Finally, as emerges from Figure 1.18, the height of the RBE maximum depends on the biological system. Systems having a large repair capacity and consequently a large shoulder in the dose effect curves (small α/β ratio) have generally a larger RBE value.

Considering all the aspects discussed until now, the fact that an uniform biological effect is not obtained by requiring a constant physical dose over the target comes forward. As shown in Figure 1.19, since the beam characteristics change during tissue penetration, RBE must be computed in an efficient way in order to obtain a uniform biological effective dose over the target.

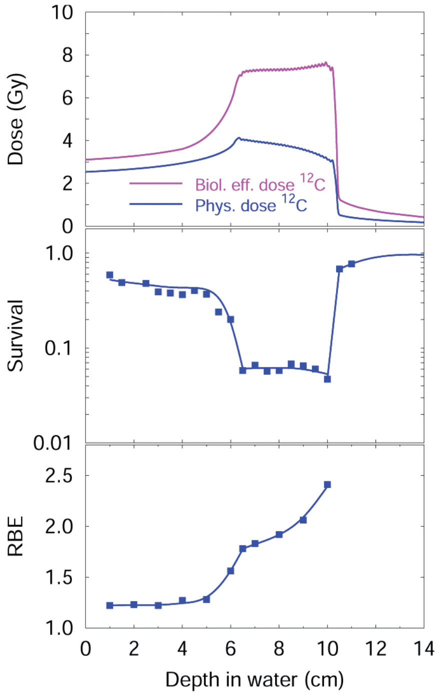

Figure 1.19: Correlation between dose, cell survival and RBE. In the top frame the physical and biological dose are shown for a SOBP between 6 and 10 cm. The corresponding survival fraction and RBE are shown respectively in the middle and bottom frames [36].

This is done by means of specific treatment planning systems based on different physical models. The most illustrative of them is currently used in carbon ion treatments at HIT (Heidelberg Ionenstrahl-Therapiezentrum, Germany) [33] and is called *Local Effect Model* or LEM. The basic idea of the LEM is that of exploiting the large database available for conventional radiation, to derive biological effects of ion radiation. This is done following the assumption that equal local doses determine equal biological effects, independently of the radiation quality. Therefore, the local effect model relates the response of biological systems following ion irradiation to the corresponding response after X-ray irradiation. Typically, the local dose around a single ion track is determined by an amorphous description of the radial dose distribution. Then, for a local dose in a given sub-volume of the cell nucleus, the biological effect is derived from photon survival curves known from experiments or clinical data, integrating the result over the entire volume of the cell nucleus. Some extensions of the local effect model exist, which consider other biological endpoints to be related with the response of the cells to radiation. For example, as the biological response of a cell to radiation is related to the initial DNA damage distribution [34], the assumption of similar double strand break densities leading to similar effects can be used for LEM calculations.

1.2.3 Oxygen Enhancement Ratio

The oxygen concentration in neoplastic tissues has turned out to be a determining factor for the biological effectiveness of radiation treatments. Tumour growth is always associated with an accelerated angiogenesis, which is necessary to supply oxygen to the cells in the tumour core. If new vessels are not generated fast enough, hypoxic regions may arise, posing a demanding challenge in tumour therapy. Hypoxic regions are known to be more radioresistant than normal oxygenated tissues, and this effect is quantified by the *Oxygen Enhancement Ratio*:

$$\mathrm{OER}_{\mathrm{iso}} = \left.\frac{D_{\mathrm{hypoxic}}}{D_{\mathrm{aerobic}}}\right|_{\mathrm{iso}} \tag{1.16}$$

where D_{hypoxic} and D_{aerobic} are the doses to tissues with reduce and normal oxygen supply respectively, resulting in the same biological effect. While the biological effect of low to medium LET radiation is highly dependent on the cell local oxygen concentration, high-LET radiation effect is almost completely uncorrelated with it. In fact, the OER is generally between 2 and 3 for low LET radiation, and decreases for heavy ions. These lower values are probably due to the higher amount of direct damages induced by heavy charged particles, which are less linked to the presence of oxygen and thus to the production of free-radicals.

1.3 Hadrontherapy technology

At the early stage of heavy-ion therapy, the technology needed to accelerate heavy-ions to kinetic energies of several MeV was not yet available. Years later, the historical evolution of accelerator technology, mainly guided by the needs of subatomic physics research, led to the development of two distinct types of accelerators suitable for particle therapy: cyclotrons and synchrotrons. However, while research machines should offer maximum flexibility, the design of medical machines has to focus on reliability and extreme care in beam control. Firstly, the choice of the accelerator type is an issue of fundamental importance: cyclotrons are considered as easy to operate, offering extremely stable and adjustable beam intensities, but no energy variation. On the other hand, synchrotrons offer fast energy variation but are more complex in operation. Secondly, hadron beams used for treatment require adjustable ranges

in order to cover the entire tumour volume width. This can be achieved depending on the accelerator type, by either changing the energy of the beam (synchrotron) or inserting absorbers in front of the patient (cyclotron).
Following these considerations, the general characteristics that a hadrontherapy centre should have are [7]:

- ability to treat most cancers at any depth;
- treatment times as short as possible;
- high ability to discriminate between the volume to be treated and the healthy tissue that surrounds it, and high dose uniformity in the treated volume;
- availability of treatment rooms with access for fixed and orientable beam lines;
- high accuracy in absolute and relative dosimetry;
- reliable control systems.

1.3.1 Accelerators

As addressed in the previous paragraph, one of the main questions in designing a hadrontherapy facility is the choice of the accelerator type. In this section the basic characteristics of cyclotrons and synchotrons will be discussed, comparing their different advantages and disadvantages.

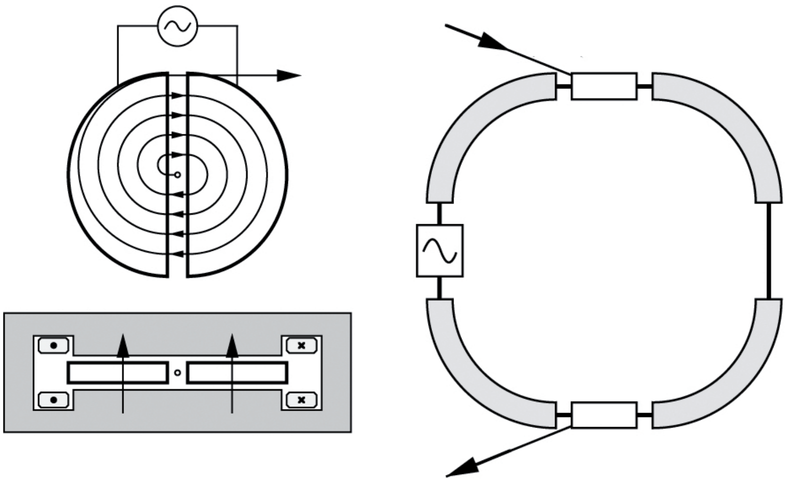

(a) (b)

Figure 1.20: (a) Schematic picture of a cyclotron. (b) Schematic picture of a synchrotron.

In Figure 1.20a a schematic picture of a **cyclotron** is depicted. Cyclotrons operate at fixed magnetic field and constant energy, and have a relatively simple and compact design. A cyclotron consists of dipole "D"-shaped magnets designed to produce a region of uniform magnetic field. These dipoles are placed face to face with a narrow gap between them. Particles are injected into the center of this gap, in which an electric field is produced by an oscillating voltage. The constant magnetic field region causes the particles to move on a semicircular path until they reach the gap, where they are accelerated. The particles increasing energy causes them to move in a larger radius with each rotation, maintaining the same angular velocity. The main disadvantage of cyclotrons is the fixed extraction energy, which can be varied only by means of passive degraders in the beam line. Furthermore, the size of the magnets and the strength of the magnetic field limit the particle energy that can be reached by a cyclotron, restricting the applications to treatment.

Figure 1.20b shows a schematic representation of a **synchrotron**. A synchrotron is a circular accelerator ring with electromagnetic resonant cavities in order to accelerate particles during each circulation. Since particles move always on the same radius increasing their energy, the strength of the magnetic field has to change with each turn. This technique allows for the production of heavy charged particle beams with a variety of extraction energies. A small linear accelerator is often used to pre-accelerate particles before they enter the ring.

While cyclotrons are widely used in proton therapy facilities, the synchrotron solution has been chosen for all heavy-ion therapy centres presently in operation or under construction. Cyclotrons produce continuous beams with high and easily controlled intensity and good stability, but have the main disadvantage that the energy of the extracted beam cannot be rapidly varied. On the other hand, synchrotrons produce a pulsed beam whose intensity is rather limited, but have the ability to vary the energies even within the spill structure. Compared to cyclotrons, the operation of synchrotrons is rather complex, although modern computer-based control systems have strongly mitigated this difficulty, and the cost of construction and operation are significantly higher.

1.3.2 Beam Delivery Systems

The beam delivery system transports the particle beam to the treatment area and distributes the beam over the planned target volume accurately and homogeneously with the desire dose distribution. There are two general methods to shape the beam to the tumour: the passive scattering technique and the active scanning technique.

In the **passive** approach, illustrated in Figure 1.21, the beam is shaped by putting specific mechanical devices in its trajectory. The monoenergetic Bragg peak is initially broadened by a scattering device, in order to generate a flat transversal

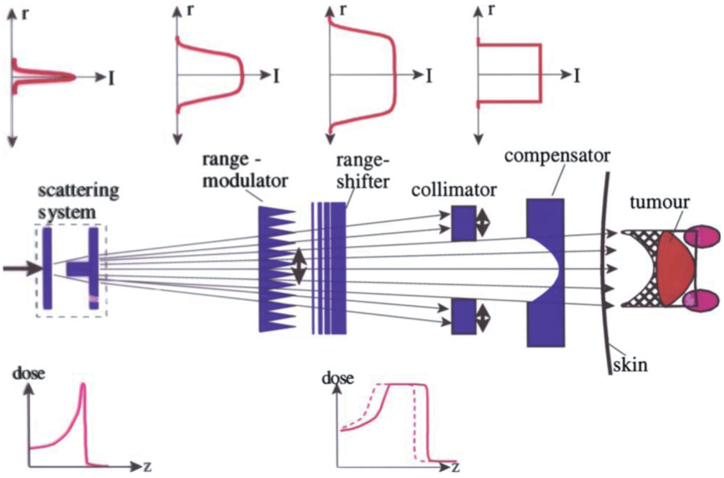

Figure 1.21: Passive beam delivery system. The initially narrow beam, entering from the left, is broadened by a scattering system and adapted to the target volume by various passive beam shaping devices (description in the text) [22].

profile, and then spread out by a range modulator and a range shifter to cover the entire length of the target volume. Finally some patient-specific collimators are used to cut out the irradiation field area defined by the largest target contour, and a compensator is used to adjust the distal depth pattern. The major limitation of the fully passive modulation system is that it is not optimal in terms of dose deposition conformity; moreover it adds an unwanted dose to the patient, due to neutrons and fragments produced in the beam interaction with the passive scanning materials.

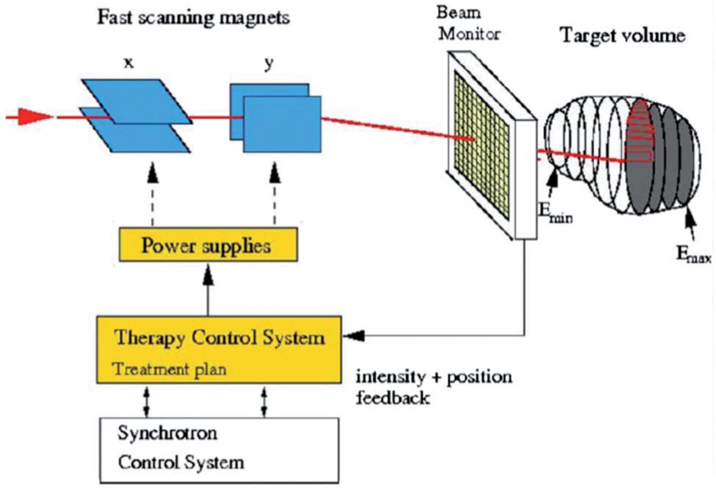

Figure 1.22: Active beam delivery system. The target volume is irradiated by moving a pencil-like ion-beam with fast magnets over thin slices in depth [22].

The **active** scanning technique exploits the physical property of charged particles of being deviated in presence of a magnetic field, as shown in Figure 1.22. The target volume is divided in layers of equal beam energy, and each layer is covered scanning its volume with a pencil beam. The depth scanning is obtained by modifying the beam energy in order to irradiate the different slices of the tumour. The active scanning system has several advantages: no patient-specific hardware is needed, the dose distribution can be better conformed to the target allowing for biological effectiveness compensation and, finally, the material in the beam path can be minimised reducing neutron contamination and other fragments.

1.4 New ions for therapy

As emerges from Figure 1.23, protons and carbon ions are nowadays the mainly used charged particle beams worldwide. Nevertheless, other particles species are still sitting on the bench [35], being already available in the most advanced particle therapy facilities around the world, but not introduced yet into clinical practice.

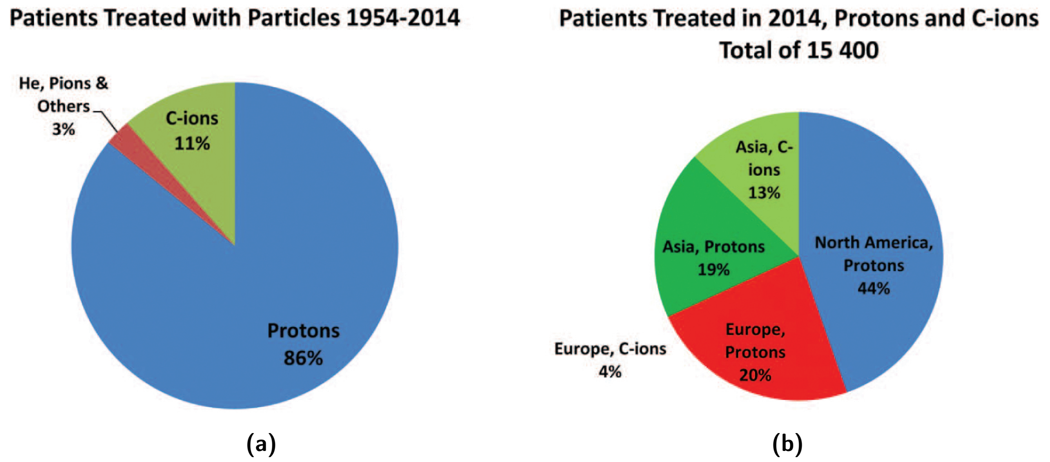

Figure 1.23: Pie charts depicting (a) patients treated with particles from 1954 to 2014 and (b) patients treated with protons and carbon ions in 2014 [37].

Protons and other ions are considered as competitive particles for radiotherapy techniques. In fact, the same physical and biological aspects that differentiate photon radiotherapy and charged particle therapy can be adopted to discuss the properties of different particle species. However, since experimental data are largely missing, studies on the physical properties of charged particles suitable for radiotherapy are mainly based on radiation transport simulations. As described in Chapter 3, this thesis work is inserted in the frame of an experimental measurement designed to study different ion types, trying in the first approach to cope with the the lack of experimental data.

The main aspects to be considered, when comparing different radiation qualities, are biological effectiveness, dose conformity and costs. As already discussed in Sections 1.2.1 and 1.2.2, LET is usually seen as a key parameter to explain the modulation of biological effects induced by heavy ions. The portion of the Bragg curve where high LET is released strongly depends on the particle type:

- Light particles, like protons and helium ions, release high LET radiation only at the very distal part of the Bragg peak.
- For intermediate particles, like carbon ions, the high LET region is nicely shaped to the Bragg peak. However considerably high LET is also released in the proximal part of the Bragg peak, in correspondence to healthy tissues.
- Heavy particles, like oxygen ions, release very high LET radiation along the whole peak, increasing the risk of normal tissue damage but being very effective in killing normally radioresistant cells.

Tumour hypoxia, as discussed in Section 1.2.3 is a critical limiting factor for radiation therapy, due to the fact that the cell response to ionising radiation depends strongly on the oxygenation level. From this point of view, oxygen ions appear to be a promising tool, as the OER becomes close to one only at LET values that are accessible for ions heavier than carbon. Recently, in fact, the idea of combining different radiation qualities to target hypoxia has started to develop. With this technique, called dose or LET painting, the high-LET radiation could be delivered only on radioresistant compartments within the tumour volume, minimising the volume of normal tissue exposed to high-LET radiation and thus radiation-induced toxicity [38]. An example of this technique is presented in Figure 1.24, in which the use of oxygen as a boost treatment for the irradiation of hypoxic cells is also shown. Obviously, in order to explain the different clinical properties of charged particles, RBE must also been considered. As shown in Figure 1.18 a dependence of RBE on particle species is observed, with the maximum RBE shifting toward higher LET for increasing particle charge. Nevertheless, the data set is really significant only for carbon ions, highlighting the fact that further experimental effort is needed to fill the gaps and implementing other ions in treatment planning software.

The dose conformity to the target is strongly related to the lateral and longitudinal beam straggling. In Sections 1.1.3 and 1.1.2 it has been shown that the lateral and range straggling are maximal for protons and reduced for increasing charge and atomic mass. Despite that, fragmentation has also to be considered, being responsible for the dose tail observed in the Bragg curves. However, since the tail contribution increases with particle range, heavier ions might be a good choice for small penetration depths.

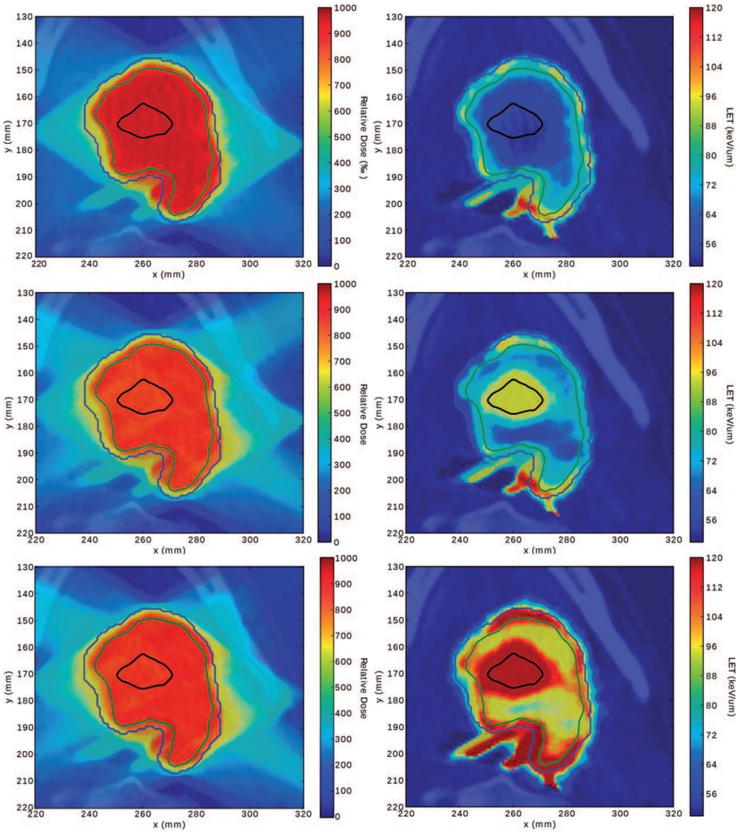

Figure 1.24: Dose and dose-averaged LET profiles are shown in left and right column respectively. Top row: ^{12}C ion plan with homogeneous dose. The highest LET is found at the rim of the SOBP, as seen in the upper right figure. Middle row: LET-painting allows for redistributing LET to cover the assumed hypoxic structure depicted as the black entity. Bottom row: LET-painting again, but with ^{16}O ions, resulting in a pronounced increase of LET in the hypoxic target volume [38].

Finally, when a comparison between protons and other ions is made, costs and equipment size need to be taken into account. One of the major advantages of proton therapy is the lower cost of proton facilities with respect to ion accelerators. Futhermore, ion accelerators need larger radius than proton ones due to the high magnetic rigidity ($R = p/q$ with p the particle momentum and q the charge) of ions.

1.5 Clinical application

According to statistics documented by the Proton Therapy Cooperative Group [39], 66 proton and carbon ion therapy centres were operational at the end of 2015. Generally speaking, being hadrontherapy a quite young technique, consolidate indications are still limited to deep seated, solid and non moving tumours, which are normally located in the vicinity of critical organs and/or extremely resistant to conventional radiotherapy. The main, well documented, indications for ion beam radiotherapy include chordomas and chondrosarcomas, uveal melanomas, sarcomas of the bone tissue, salivary gland tumours, head and neck cancers and tumours of pediatric patients [40], for whom the lower secondary cancers induction probability is definitely an issue.

The first step of the treatment configuration concerns the pre-simulation of the therapy treatment: to enable a 3D reconstruction of the treatment area, Computed Tomography (CT) or Magnetic Resonance (MR) images are necessary. Nowadays computed tomography is the basic imaging modality used in radiation oncology, due to the fact that it gives a conversion from grey scale to different physical parameters via the Hounsfield units. CTs should be performed with the patient immobilised in the treatment position. In fact, due to the high ballistic precision achievable with hadrontherapy, patient positioning is a fundamental step in the treatment planning process. To this end, imaging positioning aids and immobilisation devices are designed and made individually for each patient, before the beginning of any procedure. After the image acquisition, the radiotherapist defines the tumour and the volume to be irradiated, delimiting the organs at risk and other structures to be taken into account. Exploiting both the medical prescriptions and the informations from imaging, the treatment plan is computed by means of a complex software called Treatment Planning System or TPS. Finally, after the treatment plan has been assessed and reviewed, the underlying beam parameters and treatment geometry parameters are transferred to a database to be applied.

One of the main limits in hadrontherapy quality assurance concerns the impossibility to monitor the treatment real-time. While in photon therapy the patient positioning can be verified before and during the treatment by means of X-ray imaging, in particle therapy the charged particle beam stops inside the patient and cannot be used to take an image. Any mismatch between patient physiology at the CT time with respect to the treatment time may result in an overdosage to healthy tissues and underdosage to the tumour. Therefore, new radiation verification techniques, based on the detection of secondary particles produced by the interactions of the ion-beam with the tissues, should be soon developed and implemented in a clinical environment. In the next chapter, the dose monitoring problem will be presented and discussed, introducing some of the secondary particles which might be viable to this purpose.

Chapter 2

Monitoring in Hadronterapy

As already introduced at the end of Chapter 1, the quality of hadrontherapy treatments is closely connected with the ability to predict and achieve a determined beam range in the patient [25]. With respect to conventional treatments with photons, charged particle treatments are very sensitive to uncertainties, due to their steep dose profile. The sources of range uncertainties *in vivo* are of different nature: inherent limitations of CT image acquisition, approximations in the conversion from Hounsfield Units to stopping powers, variations in the delivered particle energy on a day-to-day basis, misplacements of patients in relation to the beam and, finally, anatomical changes [41]. Such sources are described in detail in Section 2.1. Because of these uncertainties, large safety margins around the tumour and conservative treatment plans are employed in particle therapy clinics, which might not be optimal for the patient and might impair the beneficial effects of charged particle therapy. Ionisation chamber can be used to check the transverse position and shape of the beam, but no informations can be directly retrieved about the longitudinal dose pattern [42]. An important part of the research in particle therapy is therefore aimed at developing new and improved dose monitoring techniques, possibly operating during the course of the treatment. At present, the proposed techniques are based on the detection of different secondary particles produced as a result of nuclear interactions of the incident beam with matter. There are three types of secondaries which can be used for range verification: β^+ emitters, prompt photons and charged fragments. The characteristics, advantages and disadvantages of the different techniques involving these particles will be discussed in detail in Section 2.2.

2.1 Range uncertainties

To fully take advantage of the peculiar shape of the depth-dose distribution of heavy charged particles, their range in patients needs to be predicted as accurately as possible in the treatment planning, and carefully controlled during the delivery process. Uncertainties in the exact position of the distal dose gradient may arise from [41] [43]:

- range calculation approximations due to CT conversion and CT image resolution;
- limited knowledge of tissues composition of individual patients;
- dose-deposition and accelerating systems finite resolution;
- organ motion, set-up, anatomical variations and patient positioning;
- evaluation of the multiple scattering contribution and lateral spread of the beam inside the patient;
- nuclear interactions descriptive models;
- biological considerations.

The main sources of uncertainties, however, are those connected with CT image acquisitions and patient positioning. As in conventional radiotherapy, treatment planning for hadrontherapy is done on the basis of computer tomography data sets, and suffers from their inherent limitations. Among them, image noise, beam hardening and reconstruction artefacts are only some of the aspects that can directly affect range calculations. Furthermore, in particle therapy treatment planning systems, sophisticated algorithms have been developed to translate Hounsfield Units into relative stopping power, which do not consider the actual chemical composition of different materials. Since the density and the mean excitation energy I are the two main parameters of the Bethe-Bloch that determine the range, uncertainties in tissues based on their physical compositions play a major role. When based on good quality CT images, proton beam range uncertainties due to the conversion method have been reported to be up to $\pm 1.1\%$ for soft tissues and 1.8% for bone, corresponding to a range precision of about $1 - 3\,\mathrm{mm}$ in typical treatment situations [44].

Two other important sources of range uncertainty are the fluctuations in the delivered proton energy and variations in patient positioning with respect to the ion beam, which can be quite substantial in inducing errors in range calculations. Table 2.1 lists the main sources of uncertainties for non-moving targets, evaluated with a Monte Carlo approach. Indeed, a single analytical approach to the dose calculation cannot take into account all these factors. Therefore, the development of improved Monte Carlo techniques for hadrontherapy is necessary to fully understand range uncertainties, in order to reduce the range security margins currently applied to treatment volumes.

Table 2.1: Proton range uncertainties and their sources estimated with Monte Carlo simulations. As most uncertainties depend on the beam energy or range, they are given in % rather than in mm [43].

Source of range uncertainty in the patient	Range Uncertainty
Independent of dose calculation	
Measurement uncertainty in water for commissioning	±0.3 mm
Compensator design (passive beam delivery systems)	±0.2 mm
Beam reproducibility	±0.2 mm
Patient set-up	±0.7 mm
Dependent of dose calculation	
CT imaging and calibration	±0.5%
CT conversion to tissue (excluding I-value)	±0.2%
CT grid size	±0.3%
Mean excitation energy (I-value) in tissues	±1.5%
Complex inhomogeneities	±0.1%
Total	$2.4\% + 1.2\,\mathrm{mm}$

2.2 Secondary products

Nuclear interactions, as outlined in Section 1.1.4, have many direct consequences in hadrontherapy. Firstly, they cause a significant loss of beam fluence and modify the dose distribution both in the build up region of the Bragg curve and beyond the peak. Secondly, different secondary particles are produced.

These particles, which can be used for primary beam range verifications, are of three types [25] as shown in Figure 2.1:

- β^+ emitting isotopes: among the many fragments produced during irradiation there are the β^+ emitting nuclei. Depending on the value of their half-life, these radioactive isotopes emit a positron at a later time. After travelling a small distance, the positron annihilates with an electron of the medium producing two coincident gammas of 511 keV. These photons can be finally measured with a PET detector.
- Prompt gammas: accompanying the nuclear reactions along most of the primary beam path, prompt gammas are emitted isotropically with energies up to about 10 MeV.
- Charged fragments: these nucleons and nuclear fragments, with energies that may exceed a hundred MeV are produced and emitted mostly in the forward direction.

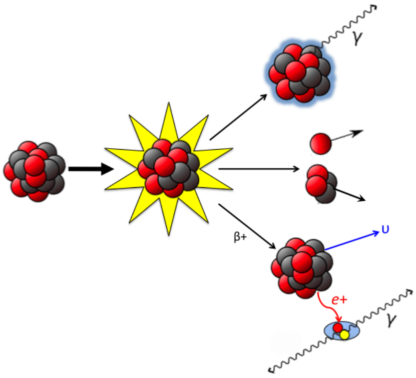

Figure 2.1: Schematic representation of a nuclear reaction and of the secondary particles subsequently produced: gamma prompt following nuclear deexcitation, charged particle following fragmentation and 511 keV photons following β^+ decay and electron-positron annihilation.

2.2.1 Gammas from e^+e^- annihilation

The Positron Emission Tomography, or PET, is an imaging technique employed in the functional diagnostic field. Its basic physical principle is the simultaneous detection of two 0.511 MeV back to back photons, produced in the annihilation between positrons and electrons of the medium. Positrons are emitted after a β^+ decay in the process described by Equation (2.1):

$$ {}^{\mathrm{A}}_{\mathrm{Z}}X \rightarrow {}^{\mathrm{A}}_{\mathrm{Z}-1}Y + e^+ + \nu_{\mathrm{e}}. \tag{2.1}$$

In **diagnostics**, PET imaging is used to obtain informations on tissues metabolism and to quantitatively measure various physiological parameters. This is done by injecting activities of the order of hundreds MBq of positron-emitter-labelled biological molecules, which target specific sites in patient's body. The most used radio-tracer in oncology is the Fluorine-18 (F-18) fluorodeoxyglucose (FDG) which, being a glucose analogue, is mostly taken up by glucose-using cells, as cancer cells are. Other commonly used radionuclides are listed in Table 2.2, with a brief description of their application. Some of those isotopes, as emerges from Table 2.2, have very short half-lives. Therefore, they need an on-site cyclotron for their production and can be used only to study processes that have a rapid uptake.
Imaging of regional tracer concentration is accomplished by using pairs of collinear detectors in coincidence, which are usually installed in a ring. Radioactivity can be then measured along lines through the organ of interest at a large number of angles, that can be used in the reconstruction of tomographic images of the regional radioactivity distribution.

In **hadrontherapy**, PET imaging is used as a dosimetric technique for *in vivo* range

Table 2.2: Common positron-emitting isotopes and radiopharmaceuticals available for PET [45].

Isotope	Half-Life (min)	Radiopharmaceuticals	Physiological Imaging Application
^{11}C	20.4	[^{11}C]-N-methylspiperone	Cerebral dopamine receptor binding
		[^{11}C]-methionine	Tumour localisation
		[^{11}C]-choline	Tumour localisation
		[^{11}C]-acetate	Myocardial metabolism
^{13}N	9.96	[^{13}N]H$_3$	Myocardial blood flow
^{15}O	2.04	[^{15}O]$_2$	Cerebral oxygen metabolism and extraction
		H$_2$[^{15}O]	Cerebral and myocardial blood flow
		C[^{15}O]	Cerebral and myocardial blood volume
^{18}F	110	[^{18}F]-fluorodeoxyglucose	Cerebral and myocardial glucose metabolism and tumour localisation
^{82}Rb	1.27	[^{82}Rb$^+$]	Myocardial blood flow

verifications. Nuclear reactions of incident protons and nuclei, as already stated, give rise to the production of β^+ emitting fragments, which can be spatially identified detecting the back-to-back 511 keV photons by means of a PET scanner. Usually, one dimensional profiles along the beam-axis are chosen to display the activity along the beam path. Such profiles are shown in Figure 2.2 for various incident beams impinging on a PMMA (polymethyl methacrylate) target. Two things can be noticed:

1. While for the p, ^{3}He and ^{7}Li ion beams, the induced activity is only due to positron-emitting target residuals, for the ^{12}C and ^{16}O beams, there is an additional contribution in the activity from positron-emitting projectile residuals.

2. The measured activity distribution, especially for lighter ions, cannot be compared directly to the applied dose distribution, thus a simulation of the expected β^+ activity has to be performed.

With respect to diagnostic PET, the involved β^+ activities are much smaller, limiting the achievable image quality. A comparison between the average activity densities, deriving from ion-beam irradiations, and those injected during normal nuclear medicine procedures is shown in Table 2.3. Reference activity distributions are generally made

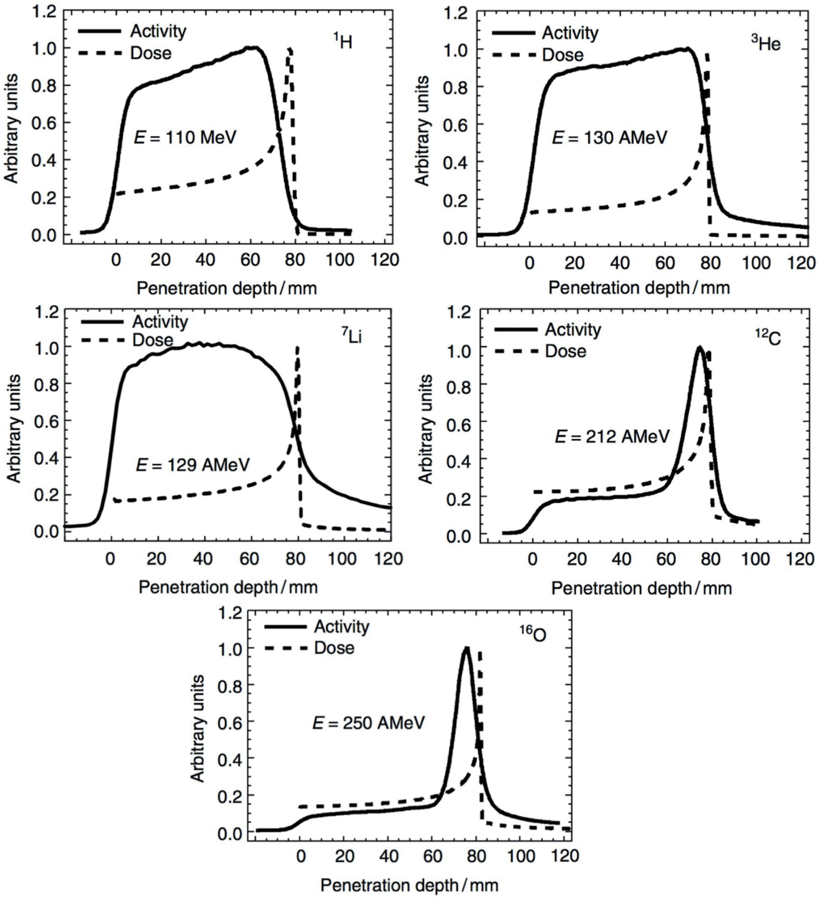

Figure 2.2: Measured positron emission activity (solid line) together with the dose distribution (dashed line) for the irradiation of a PMMA (polymethyl methacrylate) target with different projectiles [25]

Table 2.3: Comparison between induced activities following ion-beam irradiations and typical activities applied in nuclear medicine. Private report of V. Patera.

Average activity density ($\mathrm{Bq\,cm^{-3}\,Gy^{-1}}$)		
Therapeutic ion-beam	^{1}H	6600
	^{4}He	5300
	^{7}Li	3060
	^{12}C	1600
	^{16}O	1030
Nuclear medicine	$10^4 - 10^5$	

with Monte Carlo simulations, on the basis of the treatment plan, time-course of irradiation, the patient CT, detector geometry and imaging procedure. However, some important limitations are intrinsically linked to this method, usually leading to uncertainties in the β^+ yield and thus in the absolute particle range. Among them, the insufficient knowledge on cross section values, the inaccuracies in modelling biological washout and the lack of activity-to-dose maps are some of the main issues to be addressed.

For PET imaging in hadrontherapy, three acquisition strategies are usually investigated:

- **In-Beam data acquisition:** the PET system is integrated in the beam delivery system. On the one hand, the activity of some short-lived isotopes, such as ^{15}O, can be easily detected and no problems in image quality arise from biological washout. On the other hand, the costs of integrating these systems is very high and geometrical limitations affect the achievable statistics.
- **In-Room data acquisition:** the PET system is installed in the treatment room. Data are acquired quickly with a full angle coverage, reducing signal washout and problems related to patient transport and repositioning. On the other hand difficulties may arise in the co-registration of the PET image with the planning CT, and the impact of this procedure on the patient workflow may be remarkable.
- **Offline data acquisition:** the PET system is installed outside the treatment room. The costs of implementing these systems is very low; however, the delay between the treatment and the monitoring procedure rapidly causes signal degradation.

Even if the in-beam approach is the most attractive for its undeniable advantages, the low density of the implanted activity, if compared with diagnostic practice, and the huge background coming from random coincidences, limits its applicability in clinics. The first implementation of in-beam PET for the monitoring of hadrontherapy treatments, took place at the experimental carbon ion therapy facility of GSI (Darmstadt, Germany) [46]. During this clinical trial, which started in 1997 until 2008, a double head positron camera was integrated into the carbon ion therapy beam line, as shown in Figure 2.3, and more than 200 patients were monitored. This first practical experience was able to demonstrate the feasibility of the method, leading to a deeper comprehension of its physical model. A PET prototype for in beam monitoring has been also developed by the INFN and the Physics Department of the University of Pisa, within the RDH (Research and Development in Hadrontherapy) Project. This detector, called DoPET, is based on a dual head planar system, as visible in Figure 2.4 [47].

Another limiting factor of the in-beam monitoring approach is the restriction to limited angles, which reduces the achievable geometrical efficiency and thus the quality

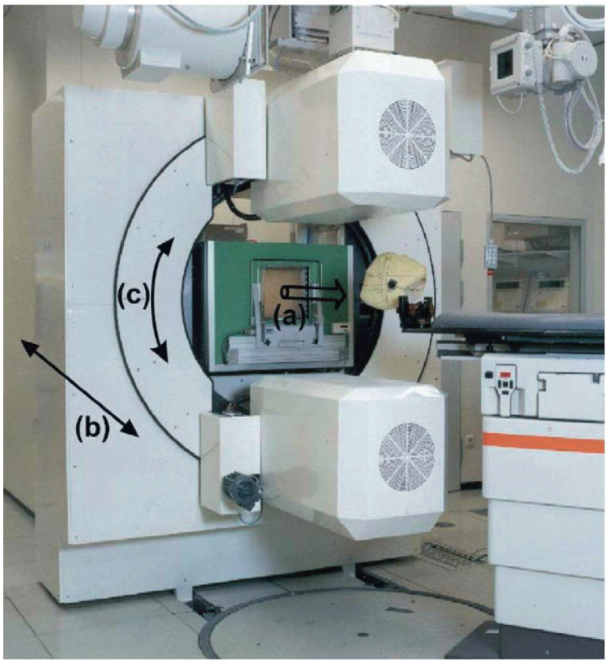

Figure 2.3: In-beam PET camera installed at GSI. The arrow (a) indicates the beam direction, while the arrows (b) and (c) show the horizontal and rotational movements respectively.

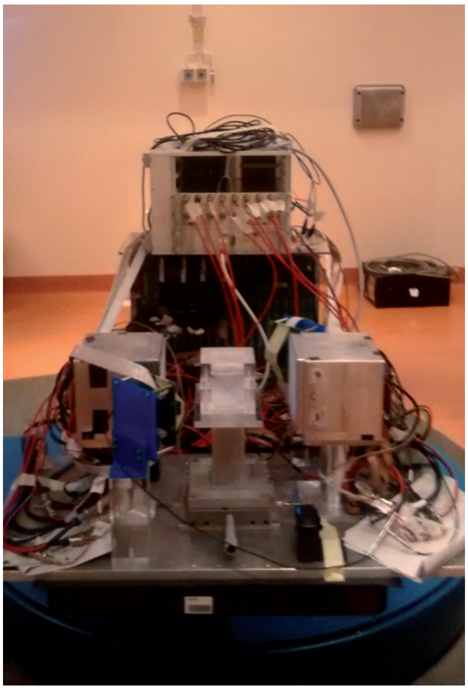

Figure 2.4: Dual head planar PET system developed by the collaboration of the INFN and the Physics Department of the University of Pisa. The detector is placed on the treatment couch at CNAO, and a PMMA target is visible in between the two PET heads [47].

of the PET images. Still, new ring-shaped PET systems are being investigated in Japan for in-beam data acquisition [25], and several groups are studying the possibility of using ultra-fast time of flight information for PET monitoring [7]. With these innovations, the problems of angular acceptance and background noise would be overcame, improving image quality and the feasibility of on-line PET monitoring.

2.2.2 Prompt gammas

The irradiation of tissues with hadron beams produces nuclear excitations, subsequently followed by de-excitations with the emission of photons. These photons, also called prompt gammas, arise in a time of the order of few nanoseconds, and are suitable particles for on-line monitoring in charged particle therapy. An exploited energy range for the detection of prompt gammas varies from ~ 1 to $10\,\mathrm{MeV}$, since photons produced after e^+e^- annihilation prevail for lower energies. Considering, for example, a proton beam impinging on a water phantom, the reaction between a proton and an oxygen nucleus giving a prompt photon emission, can be written as the follows:

$$\begin{gathered} p +^{16}\mathrm{O} \rightarrow \alpha +^{12}\mathrm{C}^* \\ ^{12}\mathrm{C}^* \rightarrow^{12}\mathrm{C} + \gamma_{4.44\,\mathrm{MeV}} \end{gathered} \tag{2.2}$$

The production reaction described in Equation (2.2) makes the prompt photons emission an independent mechanism from the patient's metabolism. Furthermore, with respect to the PET annihilation photons, prompt gammas are produced immediately when irradiating the patient, providing a real-time information very attractive for range verifications. To this end, recent studies have demonstrated that the prompt photon spatial distribution can be related with the depht-dose distribution in both proton [48] and carbon ion therapy [49], thus giving a direct indication of the position of the Bragg peak. This is shown in Figure 2.5, which refers to an experiment performed at the GANIL facility in France, with $73\,\mathrm{MeV\,u^{-1}}$ carbon ions [49]. The beam impinged on a PMMA cubic target, that can be seen in the lower part of Figure 2.5, and the ion range was determined by measuring the length of the darkened area after radiation damage. Prompt photons were detected by means of a scintillator coupled with a thick collimator, placed at 90° with respect to the beam direction and progressively translated to view different parts of the target. In this way a mono-dimensional gamma profile could be measured. Comparing the profiles in the two images of Figure 2.5, the correlation of the prompt gamma yield with the ion range emerges clearly.

However, besides prompt gamma rays from the excited nuclei, a substantial amount

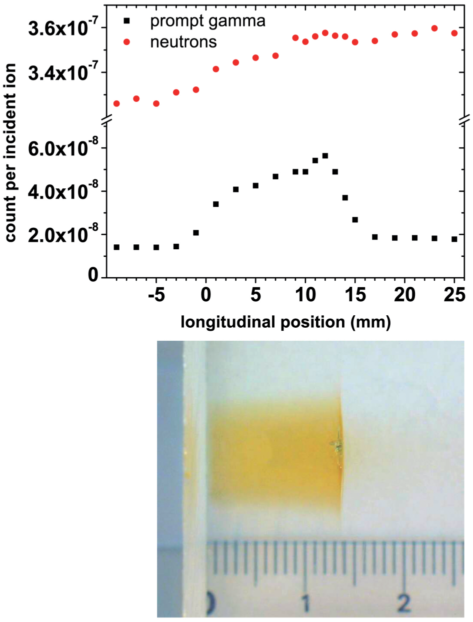

Figure 2.5: Top: measured prompt gamma (black squares) and neutron (red circles) activity as a function of the longitudinal position in a PMMA target irradiated with a 73 MeV u^{-1} carbon ion beam. Bottom: picture of the irradiated PMMA showing the radiation damaged area (in yellow) relative to the beam released dose distribution [49].

of background arises from neutrons. Thus, several imaging modalities are being investigated to shield the background and selectively acquire information from prompt gamma emission. At the energies of interest of photon emitted by nuclear de-excitation, the predominant mechanism of interaction with matter is the Compton scattering. In the Compton scattering process, a photon collides with a quasi-free electron, loses some of its energy and then is deflected from its original direction. Therefore, another gamma imaging system under investigation is the Compton camera, which uses two or more detectors to measure the initial energy and direction of photons undergoing Compton scattering inside the detectors. In this way, photon initial trajectories could be reconstructed without the use of collimators, which may produce background radiation. An additional improvement in prompt gamma detection and background rejection would be the introduction of a system based on prompt gamma timing spectroscopy (PGT). PGT spectra are distributions of the time difference between a reference time, denoting the passage of the particle bunch through a reference plane, and the prompt gamma arrival time at the detection system. These distributions encode informations about the primary particle range by means of the finite, measurable and range dependent transit time of the primary particle through the target [50]. Therefore, from the PGT statistical moments, such as the distribution mean and the standard deviation, informations on the particle transit time and consequently on its range can be extracted.

Anyway, even if prompt photons appear to be a promising tool for range monitoring, further research in detector development is still needed to bring this technique into clinical practice. So far, only one clinical trial has been done for verification of the proton range in-vivo, based on prompt gamma detection [51]: a knife-edge slit camera has been used (IBA prototype), consisting of a knife-edge shaped slit collimator optimised for the detection of $3-6\,\mathrm{MeV}$ gamma rays. The emission profile has been reconstructed by means of an array of 40 individual scintillators, resulting in a good spatially resolved gamma profile. In Figure 2.6 the camera and its position during the proton therapy treatment are shown. Inter-fractional global range variations of about $\pm 2\,\mathrm{mm}$ have been measured, showing the feasibility of a beam range monitoring technique based on prompt gamma detection in clinical practice.

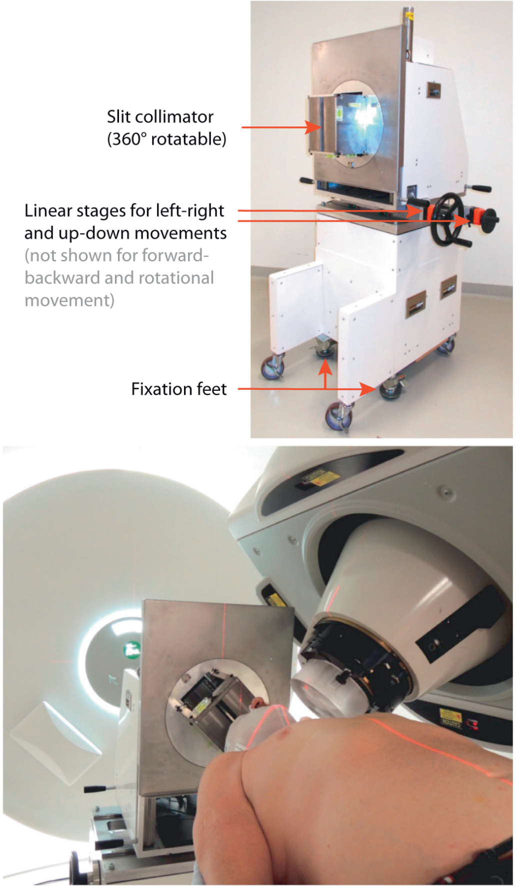

Figure 2.6: Knife-edge slit camera trolley (top) and its application during patient proton therapy treatment (bottom) [51].

2.2.3 Secondary charged particles

The approaches described so far are all based on photon detection, and need mechanical or electronic collimation to estimate the origin of the photon in order to reconstruct the gamma spatial distribution. An easier way to determine the primary beam range inside the patient appears to be the exploitation of charged particles produced after nuclear fragmentation, which can be easily tracked. This method is based on the Interaction Vertex Imaging (IVI) technique, firstly proposed by *Amaldi et al.* [52], i.e. on the reconstruction of the intersection point of two trajectories assumed to be straight lines: namely the primary beam ion trajectory and the secondary charged particle one [53].

Secondary charged particles can be detected in times of the order of few nanoseconds to $\sim 20\,\text{ns}$, and are mainly protons. With increasing ion mass, the production yield of secondary charged particles increases, with emission energies that can reach values up to 250 MeV, depending on the primary hadron beam type and energy. These particles, having velocities close to that of the primary ions, are likely to escape from the patient and can be detected with high efficiency by means of drift chambers, scintillating fibres and silicon detectors.

Recent studies [54] [55] [56] have demonstrated that the profile of the longitudinal emission distribution of secondary charged particles can be correlated to the Bragg peak position.

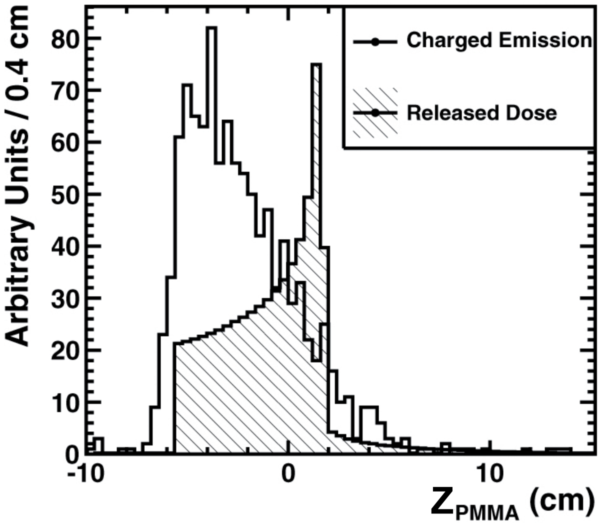

Figure 2.7: Measured longitudinal emission profile (Z_{PMMA}) of secondary charged particles (solid line) produced in the interaction of a $220\,\text{MeV}\,\text{u}^{-1}$ carbon ions impinging on a PMMA target, and the correspondent expected depth-dose distribution (hatched area) [56]. Beam coming from the left.

In Figure 2.7 the comparison between the longitudinal emission distribution of secondary products and the depth-dose profile for a $220\,\mathrm{MeV\,u^{-1}}$ ^{12}C ion beam is depicted. From this figure a relation between the two distributions can be deduced: as the ion beam enters inside the target, the number of emitted secondary charged particles increases sharply, due to the higher probability of having hard nuclear interactions, and reaches a maximum after a few centimetres. Then, while the primary beam slows down, the number of secondary products decreases, with a slope that depends on the Bragg peak position. Some parameters can be therefore extracted from the shape of the longitudinal emission distribution of secondary charged particles, to be correlated with the range of the primary beam. The properties of the longitudinal emission distribution of secondary charged particles, which are the main subject of this thesis, will be described in detail in the following chapters.

The principal issue in using charged particles as a Bragg peak position probe, is the production statistics, which lowers with increasing angles, with respect to the beam incoming direction, and with the traversed material, due to the medium absorption of charged secondaries. Indeed, fragmentation products are peaked in the forward region, and mostly contained within few degrees with respect to the beam axis. However, especially in the case of secondary protons, tails can be seen at large emission angles and energies. A large acceptance detector can be thus used to reconstruct the secondary charged particles direction, as the quality of the trajectory reconstruction compensates for the reduction in statistics. Large angles with respect to the beam axis are of great interest for the purposes of monitoring in hadrontherapy. For geometrical reasons, considering also the multiple scattering suffered by charged particles inside the material before exiting the patient, the achievable sensitivity in the reconstruction of the emission origin is optimal in the $60° - 90°$ angular range. Furthermore, thinking about future applications of charged particle detectors in clinics, the positioning at large angles would be easier to manage in a treatment room.

Nowadays, among the techniques so far described, only the off-line PET is adopted in clinical practice, while in-beam PET and prompt gamma detection are the only real-time monitoring approaches already tested on patients. Even if the techniques associated with PET and prompt photons detection are expected to have the highest sensitivity, charged particles can still provide a useful additional information when combined with them as part of a "hybrid" system. The experiment of which this thesis is part, provides a preliminary study of feasibility for the construction of an integrated system, the *Dose Profiler*, developed in the framework of the INSIDE (Innovative Solutions for In-beam Dosimetry in hadrotherapy) project [57]. The Dose Profiler design aims to detect both prompt photons and secondary charged particles, working simultaneously as a Compton camera and a tracker, as schematically shown in Figure 2.8. The operation of the Dose Profiler would exploit the information given by 6 planes of scintillating fibres, followed by an electron absorber and a LYSO calorimeter.

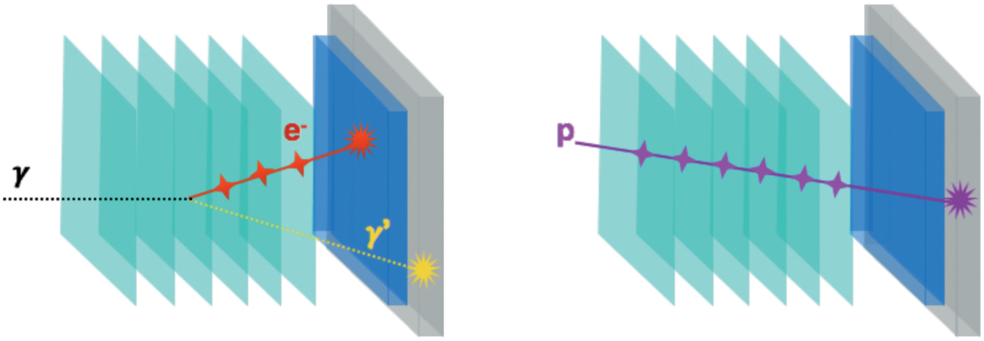

Figure 2.8: Detection principle of a prompt photon undergoing Compton scattering (left) and of a secondary proton (right), in the dose profiler. The tracking planes (green), the absorber (blue) and the calorimeter (grey) are shown.

The work presented in this thesis is part of an experiment that took place at the Heidelberg Ion Therapy Centre (Germany), with the purpose of studying the different monitoring techniques in hadrontherapy. As will be described in Chapter 3, data were acquired irradiating a polymethyl methacrylate (PMMA) target with different ion beams at different energies, and detecting all the different secondary products presented in this Section. This thesis project, in particular, aimed at studying secondary charged particles emitted by oxygen beams impinging on the PMMA, in order to define the feasibility of a monitoring approach based on their detection at large angles. A detailed description of the analysis performed in this study will be presented in Chapter 3.

Chapter 3

Experimental Apparatus

In this Chapter, the experimental apparatus used to acquire the data presented in this thesis will be described. The aim of the experiment, as mentioned at the end of Chapter 2, is that of characterising the secondary radiation production during the irradiations of a PMMA block with different ion beams. The obtained measurements are of fundamental importance for the development and construction of a dose monitoring device for particle therapy. The irradiations were all accomplished at the Heidelberg Ion Beam Therapy Centre (HIT), described in Section 3.1, with a rather complex set of detectors aiming at measuring all the different secondary products previously described (see Section 2.2). The next Sections will focus especially on the experimental set up regarding the detection of secondary charged particles, which are the main subject of the analysis performed in this work.

3.1 HIT: Heidelberg Ion Beam Therapy Centre

The experiment of which this thesis is part, took place in February 2014 at HIT, the Heidelberg Ion Beam Therapy Centre in Germany. HIT is the first Europe hospital-based treatment facility for heavy ion radiotherapy with protons and various heavy ions. After a dedicated planning, construction and commissioning phase, patient treatments started in 2009. Since then, more than 2500 patients have been irradiated with both protons (~ 1700) and carbon ions (~ 800) [37]. The operation principle of the facility is shown in Figure 3.1.
The main steps of the acceleration chain are the following [59]:

1. **Ion source**: This is where proton and ion beams are generated. To create protons, hydrogen gas is used, while carbon dioxide is used for carbon ions. Other available ions are: helium and oxygen ions.

2. **Linear accelerator**: Before being injected in a synchrotron, ions are pre-

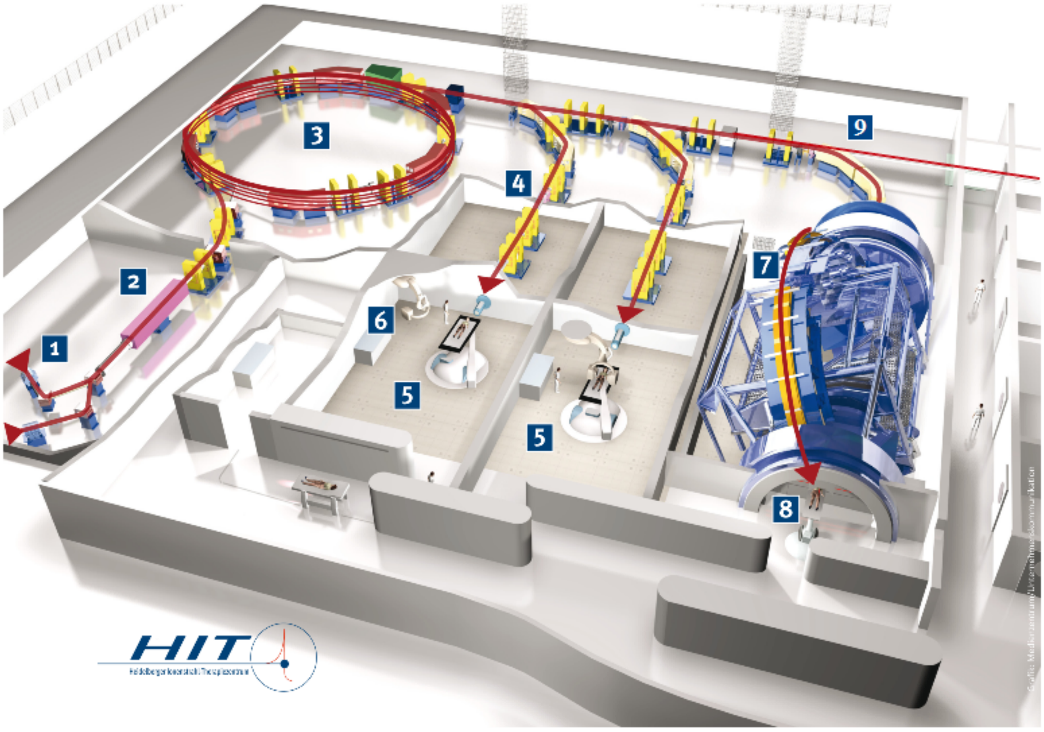

Figure 3.1: Schematic illustration of the technical components of the Heidelberg Ion Beam Therapy Center (HIT). Ions are created from the ion sources (1) and accelerated firstly in the linear accelerator (2) and secondly in the synchrotron (3). Vacuum tubes and bending magnets (4) guide the beam to the horizontal treatment rooms (5) which are equipped with position control systems (6). Alternatively the beam can be guided to the gantry (7) which allows irradiations for several angles (8). A fourth room (9) with a fixed beam line is available for experiments and quality assurance. Adapted from [58].

accelerated in a linear accelerator, up to about 10% of the speed of light.

3. **Synchrotron**: From the linear accelerator, ion beams are injected into a synchrotron with a diameter of 20 m. Here, six 60° magnets bend the ions trajectory into a circular path, until they reach the designated energy.
4. **High Energy Beam Transport (HEBT) line**: When the desired energy is reached, the ion beams are focussed by means of quadrupole magnets and guided in vacuum tubes towards the treatment rooms.

An intrinsic property of a synchrotron is that the irradiation is not continuous. At HIT, the acceleration phase takes up to five seconds and is followed by an extraction phase with a similar duration. This leads to the characteristic spill structure shown in Figure 3.2.

The desired beam parameters can be chosen from a predefined library of 255 energies, 6 widths of the beam spot and 15 intensity steps for each ion species [60]. Depending on the ion type, the energy interval can cover ranges in water between 2 cm and

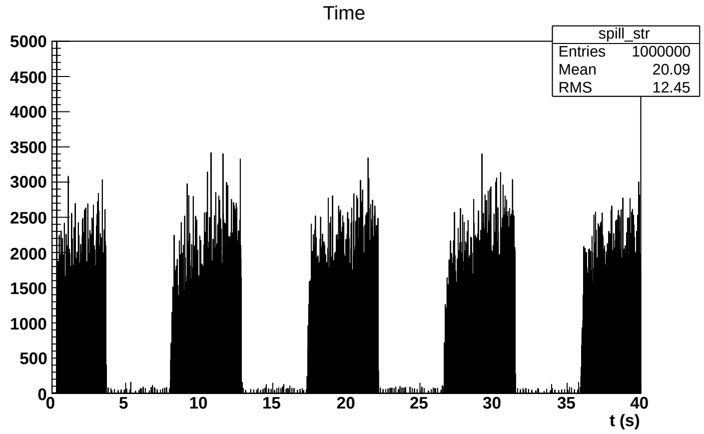

Figure 3.2: Example of spill structure for an oxygen beam of 300 MeV u^{-1} at HIT.

30 cm. This results in a spacing of the Bragg peak position equivalent to 1 mm for the first 195 energy steps, and to 1.5 mm afterwards. As emerges from Equation (1.11), lower beam energies and lighter ion species experience enhanced multiple Coulomb scattering in the beam line. In order to reach a compromise between accuracy and speed during the treatment, six different values for the Full Width at Half Maximum (FWHM) of the beam spots are available. Finally, logarithmically-spaced beam intensities can be selected for carbon ions in the range from 2×10^6 particles/s to 5×10^8 particles/s. For the other ion types, the intensities are adapted to reach the same dose rates.

Within the HIT center, as shown in Figure 3.1, radiation therapy is offered in three treatment rooms, two equipped with a horizontal beamline and one with the world's first gantry, allowing irradiations from 360° [61]. Additionally, a fourth room with a fixed beam line is available, dedicated to quality assurance and preclinical research. In this last room the experiment to which this thesis is related took place.

In the treatment rooms, patient positioning is performed by means of robotic treatment tables offering maximal variability and flexibility. Indeed, the robotic table can be moved in six ways, allowing many different beam entrance angles. Furthermore, combining these movements with the rotating beam delivery system, an infinite number of beam entrance angles can be realised, achieving a superior dose distribution for certain tumours. Finally the HIT facility is the first ion therapy facility with intensity-controlled raster scanning. With this technique, the radiation volume is virtually divided into tiny regions, each of them receiving an optimised radiation intensity during the scanning process. The relevant accelerator and facility parameters of the Heidelber Ion Beam Therapy center are summarised in Table 3.1, while in Figure 3.3 some details of the treatment rooms are shown.

(a) (b)

Figure 3.3: Pictures of the treatment rooms at HIT. (a) One of the two horizontal treatment rooms, in which the positioning systems are clearly visible. (b) The gantry room. Pictures from `www.klinikum.uni-heidelberg.de`

Table 3.1: HIT relevant accelerator and facility parameters [62] [61].

Particle species	p, He, C, O
Accelerator type	Synchrotron
Beam intensity (particles per synchrotron cycle)	p: 4×10^{10} He: 1×10^{10} C: 1×10^{9} O: 5×10^{8}
Beam energy	p: $48 - 221\,\mathrm{MeV\,u^{-1}}$ He: $50 - 220\,\mathrm{MeV\,u^{-1}}$ C: $88 - 430\,\mathrm{MeV\,u^{-1}}$ O: $104 - 515\,\mathrm{MeV\,u^{-1}}$
Beam spot size	$4 - 10\,\mathrm{mm}$ FWHM (2D-gaussian)
Range resolution	$\approx 1\,\mathrm{mm}$
Treatment rooms	2 fixed horizontal-beam treatment room 1 gantry room
Beam delivery technique	Intensity controlled raster scanning
Treatment field	$20 \times 20\,\mathrm{cm}^2$
PET monitoring type	In-situ verification of the irradiation procedure
Number of patients per year	$\gtrsim 1000$
Building area	$5000\,\mathrm{m}^2$

3.2 Description of the experimental apparatus

In 2011, an experimental campaign started, with the aim of giving some answers regarding the yield of secondary products emerging from a tissue-equivalent target irradiated with different ion beams. The first experiment was performed in March at the Laboratori Nazionali del Sud (LNS) [54] [63] with a 80 MeV u^{-1} ^{12}C ion beam impinging on a poly-methil methacrylate (PMMA) target. From this experiments, the differential production rates of protons and photons were obtained, for a deposited energy greater than 2 MeV and detected at an angle of 90° with respect to the beam axis. In May 2012 a similar experiment was performed at the GSI (Gesellschaft für Schwerionenforschung, Darmastadt, Germany) facility with 220 MeV u^{-1} ^{12}C ion beams [56]. In this occasion, yields were obtained for protons, deuterons, tritons and photons measured with two detector configurations: at 90° and 60° with respect to the beam axis. Finally, in February 2014, following the experiences at the LNS and GSI laboratories, a new experiment was conducted at HIT, thanks to the collaboration of the INFN RDH commission V, the Centro Fermi and the University of Roma La Sapienza. The actual innovative aspect of this experiment was the use of different ion beams at different energies, for which few or no data are available. Indeed, the study of helium and oxygen beams appears to have a key role in the future development and widespread of new hadrontherapy applications, as underlined in Section 1.4.

The experiment performed at HIT had different purposes, summarised in the following macro-areas: (1) analysis of secondary charged particles for monitoring purposes; (2) analysis of neutral particles for monitoring purposes; (3) analysis of PET photons for the development of in-beam techniques and (4) the study of forward-emitted fragments for dosimetric purposes. Necessarily, each one of these goals asked for dedicated detectors and different set-up, in order to measure and analyse the different particle characteristics. A scheme of the global experimental apparatus is shown in Figure 3.4, in which different colours highlight the different parts of the experiment.

Starting from the left of Figure 3.4, the incoming direction of the various ion beams is depicted. When the beam exited from the vacuum tubes through the Beam Exit Window (BEW) helium ions had energies which varied from 100 MeV u^{-1} to 150 MeV u^{-1} while energies varied from 160 MeV u^{-1} to 400 MeV u^{-1} for carbon and oxygen ions. The beam then encountered a small scintillator, named Start Counter (SC), and the PMMA target, both highlighted in red, meaning that they were common elements of the experimental set-up. The choice of a PMMA target is very common in medical applications thanks to its chemical composition ($C_5O_2H_8$), which gives it physical-chemical properties similar to those of human tissues. Foreseeing the introduction of monitoring detectors into normal clinical practice, target positioning is a crucial issue for the subsequent analysis and reconstruction of secondary particles emission profiles. Thanks to a preliminary Monte Carlo simulation, the Bragg peak position inside the PMMA was estimated for helium, carbon and oxygen ion beams at different energies. The length of the target was then chosen in order to contain all the primary beam energy and to find the Bragg peak at least 1 cm before the end of the PMMA block. Depending on the primary beam energy, three PMMA lengths

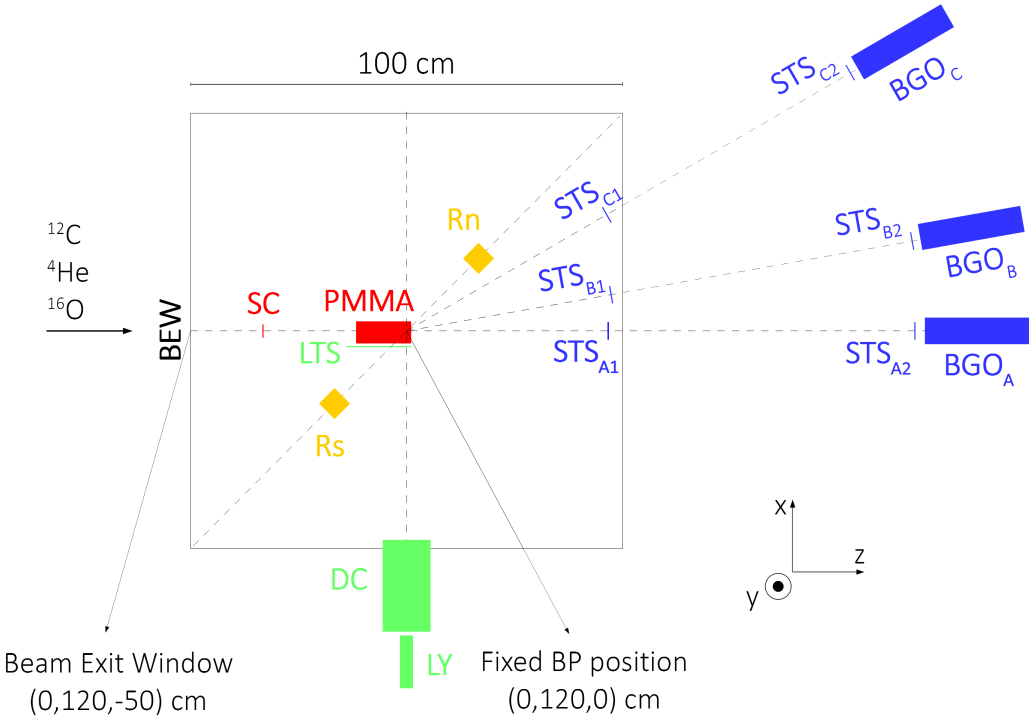

Figure 3.4: Schematic drawing of the experiment performed at HIT: (red) common elements, (green) measurement of secondary charged particles and prompt photons, (yellow) measurement of PET gammas, (blue) measurement of forward emitted fragments. The PMMA and the SC,LTS, Rn, Rs and STS$_1$ detectors were placed over a table of $100 \times 100\,\text{cm}^2$, while the BGOs and STS$_2$ were mounted on rotating supports. The LYSO and DC position was aligned with the Bragg peak on the horizontal plane, and could be rotated with respect to the beam axis at 90° or 60°

were available: 7.65 cm, 10 cm and 12.65 cm. Furthermore, the Bragg peak position determined the isocentre of the apparatus, with respect to which all the detectors were aligned. In the experiment, the following detectors were used:

- Start Counter (SC) scintillator: this thin plastic (EJ-200) scintillator of 2 mm thickness and $30 \times 30\,\text{mm}^2$ surface, was connected to two photomultipliers (PMTs) for the counting of the primary ions. The logic AND between the two PMTs determined the "start" of the acquisition.
- Large Thin Scintillator (LTS): this thin plastic (EJ-200) scintillator, of the same thickness of the SC, is 15 cm long, and was located on the PMMA lateral face. It was used to differentiate charged particles from the neutral ones, by means of Time of Flight (ToF) measurements.
- Drift Chamber (DC): is a multi-wire drift chamber used to reconstruct charged particle tracks. It is 21 cm long and, together with the LYSO, could be placed at 90 or 60 degrees with respect to the beam axis.

- LYSO (LY) scintillator: this 2 × 2 matrix of plastic scintillator crystals ($Lu_{1.8}Y_{0.2}SiO_5(Ce)$) was placed at $\sim 75\,\mathrm{cm}$ from the target in order to measure both the energy and the time of flight of prompt photons and secondary charged particles. Each crystal is 120 mm long and has a surface of $30 \times 30\,\mathrm{mm}^2$.
- Short Thin Scintillator (STS): these thin plastic (EJ-200) scintillators have a 2 mm thickness and a surface of $40 \times 40\,\mathrm{mm}^2$. They were coupled in order to measure the ToF for fragmentation analysis, and were placed at 0° (A), 10° (B) and 30° (C).
- BGO scintillator: these 2×2 matrices of inorganic scintillator crystals ($Bi_4Ge_3O_{12}$) were placed at a distance of 1.2 m from the target at different angles (0°, 10° and 30°), and were used for the angular analysis of forward emitted fragments. They have a trapezoidal shape, with a height of 240 mm, larger base of $60 \times 60\,\mathrm{mm}^2$ and smaller base of $47 \times 47\,\mathrm{mm}^2$.
- Rn and Rs: these detectors are made of 23 × 23 pixel matrices of two LYSO crystals of $50 \times 50 \times 16\,\mathrm{mm}^3$ each. They were placed one in front of the other on each side of the PMMA, in order to detect back to back photons coming from e^+e^- annihilations.

In Figure 3.5 a collection of pictures taken during the data acquisition is shown, in which the different detectors described until now can be identified. In the next Sections, the different purposes of the experiment will be examined in detail, paying particular attention to the detection and measurement of secondary charged particles.

3.2.1 Detection of charged particles

Secondary charged particles produced after nuclear interactions of ion beams with tissues, present many interesting aspects for dose monitoring purposes. As previously shown in Figure 2.7, the longitudinal emission profile of secondary charged particles can be used to determine the primary ion beam range, at least for an homogeneous target. In order to reconstruct this profile, a tracking device is needed to determine the longitudinal emission coordinate (vertex) of these particles. To achieve this purpose, as already done in the experiments performed at LNS and GSI, a multi-wire drift chamber was used, that will be described in detail in the next paragraph. Furthermore, since secondary charged particles are of different nature, a system to establish their mass and energy is also necessary. This could be done by means of the LTS and the LYSO, which together were able to give informations about the time of flight and deposited energy of the different particles.

In Figure 3.4 the DC and LYSO are placed at 90° with respect to the beam direction. During the data acquisition, measurements were performed also at 60°. Indeed,

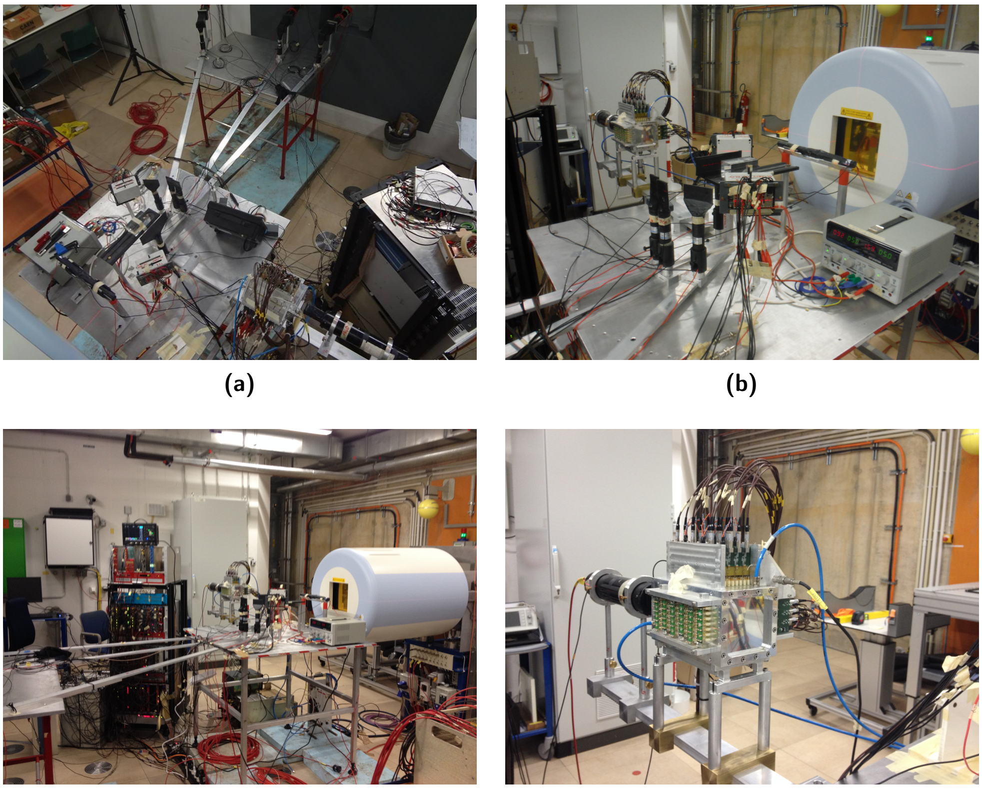

(a) (b) (c) (d)

Figure 3.5: Experimental set-up at HIT: (a) panoramic view of the experiment, (b) detail of the Beam Exit Window, (c) view of the electronic modules, (d) detail of the drift chamber.

the choice of the detection angle appears to be a crucial issue in any monitoring application. While prompt gammas are emitted isotropically, secondary charged fragments present a completely different situation, being their emission rate enhanced at small detection angles. Therefore, a low angle position should be chosen, in order to maximise the collected statistics. However, other geometrical and practical aspects must be taken into account when foreseeing the introduction of a monitor device in ordinary clinical practice. The emission distribution profile of secondary charged particles suffers from multiple Coulomb scattering, determining an intrinsic uncertainty in the back tracking of these particles to the beam line. The multiple scattering angle resolution is proportional to the square root of the particle path length inside the target, thus being minimised at a 90° detection angle. On the other hand, this resolution is inversely proportional to the particle energy, that decreases with larger detection angles. As a consequence of this opposite effect, from the point of view of multiple Coulomb scattering, no clear advantages arise for larger or smaller emission angles. The situation is very different, however, when considering the reconstruction accuracy. In fact, the uncertainty of the emission point has a dependency on the emission angle, due to the non zero transverse dimension of the ion beam. As shown in Figure 3.6, this uncertainty is given by $\sigma = \sigma_{\text{beam}}/\tan(\theta)$, and it is minimum when an angle $\theta = 90$ degree is considered. Furthermore, positions at low θ are not very often available for a monitor device during hadrontherapy treatments, especially when the patient body is aligned with the beam axis. All these considerations together, make it preferable to choose detection angles in the range of $60° - 90°$.

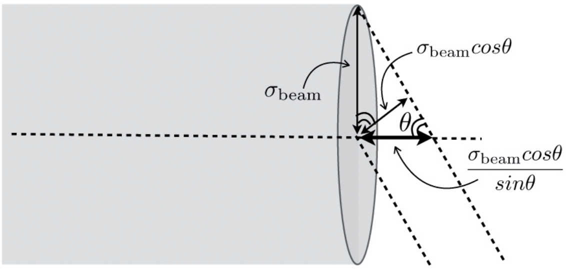

Figure 3.6: Scheme of the beam spot size (grey cylinder) and of its contribution to the reconstruction of the secondary charged particle emission vertex. Experimental set-up placed at an angle θ with respect to the primary beam direction [64].

In the following paragraphs, a detailed description of the set-up elements of interest for the detection of secondary charged particles, and some general aspects of the analysis will be given.

Drift Chamber

A drift chamber is a proportional counter in which the spatial information is obtained by measuring the drift time of the electrons coming from an ionising event. When a charged particle passes through a gas, it interacts electromagnetically with nearby electrons, generating electron/ion pairs along its path. The number of such ionisations depends on the energy of the particle and on the type of the gas. If an electric field is applied to the gas, electrons will start to drift towards the positive sense wire, undergoing repeated collisions with the gas molecules and inducing further ionisations. In this way an avalanche is formed, in which the number of electrons increases exponentially. When such electron cascade reaches the positive anode, an electric current, proportional to the original number of created ions, arises. Since electrons drift with a predictable speed, a measurement of the drift time can be turned into a measurement of the distance of the original source particle from the anode. If a trigger is available to signal the arrival of a particle, then the distance from the sensing wire to the origin of the electron is [65]:

$$x = \int_{t_0}^{t_1} v \, \mathrm{d}t \tag{3.1}$$

where t_0 is the arrival time of the particle, t_1 is the time at which the pulse appears at the anode and v is the drift velocity. In order to have a linear relationship between distance and time, the electric field should be made as constant as possible over a large volume.

The drift chamber used in the experiment performed at HIT, shown in Figure 3.5d, is made of alternated horizontal (U-view) and vertical (V-view) wire layers, for a total number of 12 planes. Each layer has three rectangular cells of $16 \times 10\,\mathrm{mm}^2$ along the beam direction, as depicted in Figure 3.7

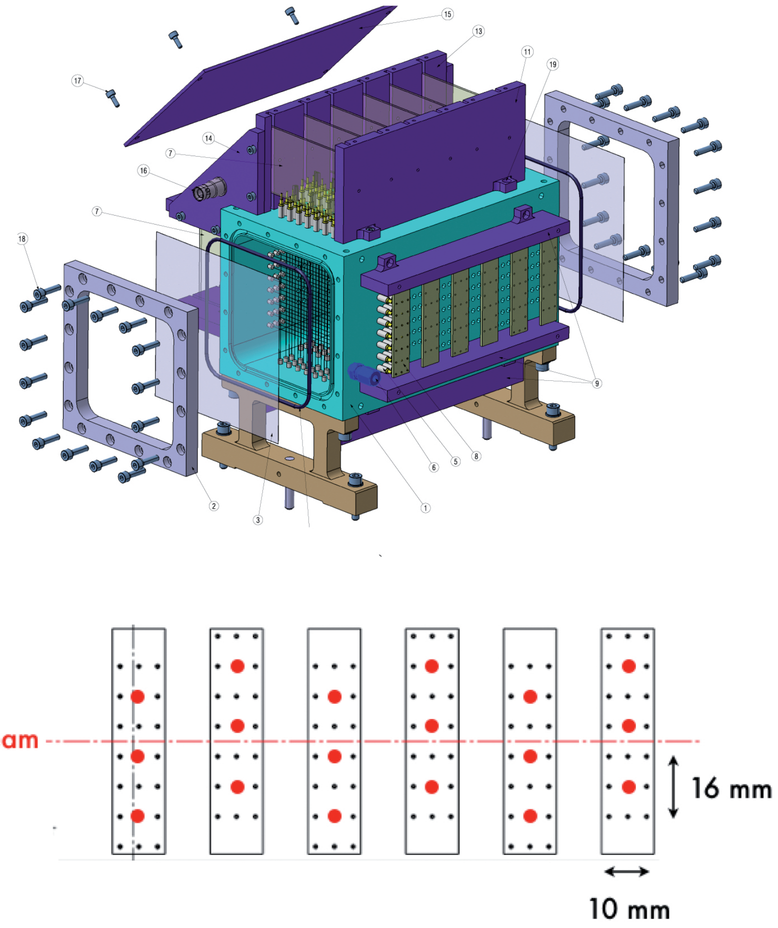

Figure 3.7: On top: scheme of the drift chamber mechanism. Below: DC lateral layout, the red dots show the sense wires [64].

The geometrical layout, custom front-end, electronic boards and track-reconstruction algorithm were designed and optimised by the Laboratori Nazionali di Frascati (LNF).

The twelve planes provide tracking redundancy while minimising ion interactions with the wires. Furthermore consecutive layers of each view are shifted by half a cell, in order to minimise tracking ambiguities. The performances of the drift chamber were evaluated in terms of efficiency and spatial resolution by *Abou-Heider et al.* [66]. With the chamber operated applying a high voltage of 1.8 kV to the sense wires and filling it with a Ar/CO_2 (80%/20%) gas mixture, the single cell spatial resolution is $\sigma_{DC} \leq 200\,\mu m$ and the single cell efficiency is $\epsilon_{DC} = (93 \pm 3)\%$, at a distance of ~ 75 cm. This was the applied configuration for the experiment performed at HIT. The hits recorded by the drift chamber can be used to reconstruct the trajectories of charged particles in the detector active volume. To this end, suitable electronic signal processing has to be use in order to determine the position and direction of the crossing particle. The temporal information of each hit is measured by means of a Multi-hit TDC (CAEN V1190B) module, capable of temporarily store informations about the time spread of hits related to the same event, within a programmable-size time-window. Then, this temporal information can be converted into a measurement of the ionisation event distance from the fired sense wire, by means of space-time curves as the one shown in Figure 3.8.

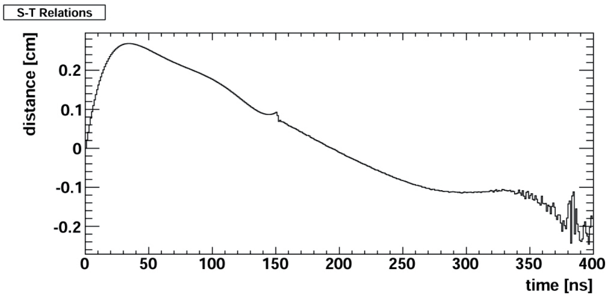

Figure 3.8: Space-time curves obtained operating the DC at 1.8 kV with an Ar/CO_2 (80%/20%) gas mixture. [66].

The spatial information extracted form the s-t relation is employed also to select track candidates to be fitted, considering only those events in which only one cell per plane is fired. Finally, a tracking algorithm, based on a least square iterative fitting method, is used to determine the trajectories of charged particles crossing the detector. An example of a reconstructed track is shown if Figure 3.9.

Even if the position of a particle in the DC can be determined with an accuracy of a hundred microns, the vertex reconstruction along the beam axis has an intrinsic uncertainty of the order of some millimetres, mainly due to multiple scattering inside the target. The very efficient and fast response drift chamber is hence a perfect low cost charged particle detector for the aim of the measurement described in this work.

The DC can be used also to discriminate among different secondary particle types

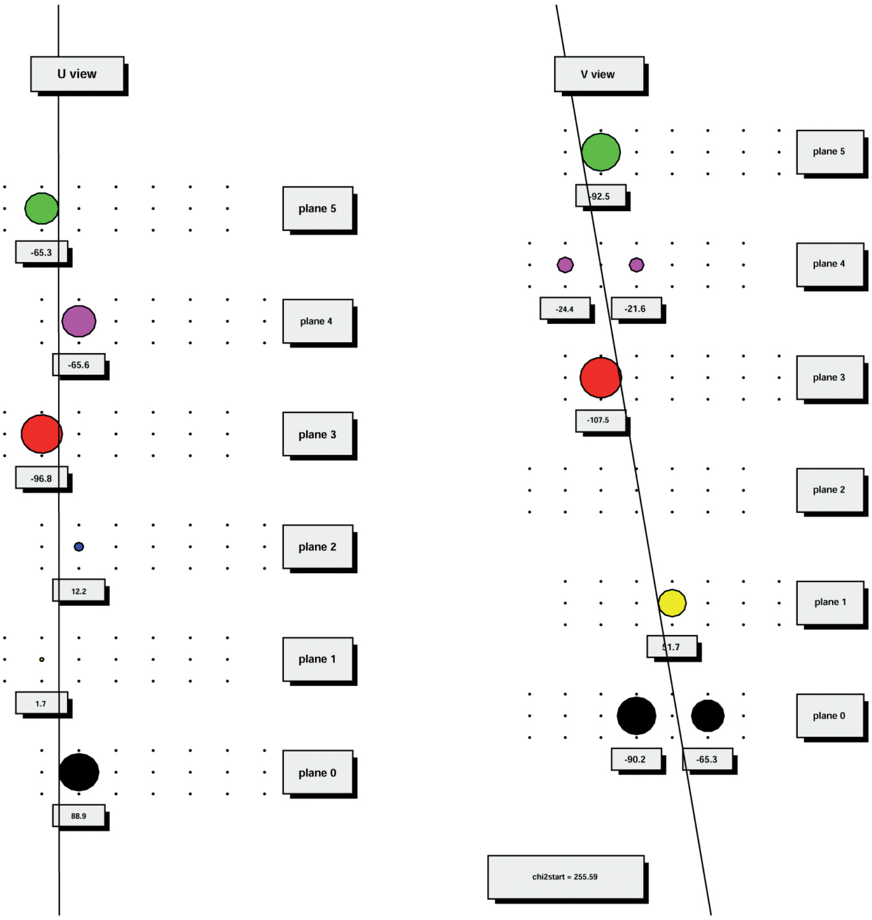

Figure 3.9: Example of particle track reconstruction by means of the least square iterative fitting method. Hit wires are depicted as coloured circles with a diameter proportional to the drift time measured with the TDC.

emerging from the PMMA, thanks to the analysis of the number of hits distribution. As an example, the distribution of the number of hits in the 90° configuration for the experiment performed at GSI is shown if Figure 3.10. In this Figure, FLUKA Monte Carlo predictions are compared to the experimental data, and normalised to the $N_{\text{hits}} = 12$ bin. The peak at $N_{\text{hits}} = 12$ appears to be the signature of secondary charged particles that crossed all the DC planes firing one cell per plane. Therefore, events in which the reconstructed tracks satisfy, for example, the requirement $N_{\text{hits}} \geq 8$, can be selected for secondary charged particles analysis. This procedure will be described in greater detail in Section 4.3, considering the specific N_{hits} distribution for the experiment performed at HIT.

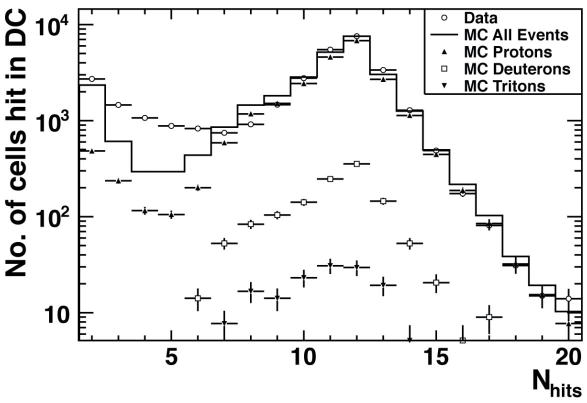

Figure 3.10: Data (circles) and MC (solid line) distributions of the number of hit cells in the DC (N_{hits}) for the experiment performed at the GSI. Individual contributions from protons (up triangles) deuterons (squares) and tritons (down triangles) obtained from the simulation, are shown. The MC data have been normalised to the experimental data using the $N_{\text{hits}} = 12$ bin [56].

Scintillators

Scintillation detectors are undoubtedly the most often and widely used particle detection devices in nuclear and particle physics. Scintillation materials exhibit the property of emitting small flashes of light when struck by ionising radiation. When coupled to an amplifying device, such as a photomultiplier, this light can be converted into electrical pulses, which can give information concerning the incident radiation. An ideal scintillation material should posses many properties: the ability to convert linearly the kinetic energy released by radiation into detectable light; transparency to the wavelengths corresponding to its own emission; short decay times; refraction index similar to that of glass (~ 1.5), which permits efficient coupling to any light sensor. Obviously, a material meeting all these criteria together does not exist. A first distinction can be done between organic and inorganic scintillators. The first are generally faster, but yield less light, while the seconds tend to have the best light output and linearity, but are relatively slow in their response time. Two are the main processes which lead to the production of light following excitation from ionising radiation: fluorescence and phosphorescence, which are distinguished by the different wavelength of the scintillation outcome. The process of fluorescence indicates the prompt emission of radiation following some kind of excitation, while phosphorescence corresponds to the emission of longer wavelength light with greater decay times. Thus, the time evolution of the number of emitted scintillation photons in a single scintillation event can be often described by the linear combination of two exponential decays, with a fast (τ_{f}) and a slow (τ_{s}) decay constant.

Organic and inorganic scintillators may be differentiated by their different mechanism of fluorescence. In the first, fluorescence arises from transitions in the energy level structure of a single molecular species, independently of it physical state. In the second, the scintillation process is due to the electronic band structure found in crystals, and arises from electron transitions from the valence band to the conduction band.

The light output of a scintillator is defined by its efficiency in converting ionisation energy into photons. In general, this value depends on the incident particle type, and does not always vary linearly with the energy. For example, very high ionising particles might induce quenching effects, i.e. interactions in which the energy is transferred by means of non-radiative mechanisms, with a consequent reduction in the light output. This effect is more pronounced for organics than for inorganic crystals, making the latest to be preferable for the detection of these particles. Furthermore, inorganic crystals have a high stopping power, providing better energy resolution.

It must be kept in mind that, as scintillation detectors are inseparably coupled to a photomultiplier, the efficiency of the latter has to be taken into account. Typical values for this efficiency are of the order of 30%, meaning that only 30% of all the emitted photons will be actually detected. A typical photomultiplier is made by two major components: a photosensitive layer, followed by an electron multiplier structure. The first serves to convert the photons emitted by the scintillating material into electrons; while the second provides an efficient collection geometry for the photoelectrons, amplifying their number with a cascade effect.

In the experiment performed at HIT, different scintillation detectors of both the organic and inorganic type were used. Regarding the detection of secondary charged particles, the scintillators of interest were the SC, the LTS and the LYSO. The first two are plastic (organic) scintillators (EJ-200) of 2 mm thickness, while the second is an inorganic crystal of Lutetium and Yttrium Ortho-Silicate doped with Cerium. The LYSO is made by a 2×2 matrix of $1.5 \times 1.5 \times 12\,\mathrm{cm}^3$ crystals, each of them covered with 100 µm of tyvec. The choice of the LYSO crystals was driven by their relatively fast time response ($\tau \sim 42\,\mathrm{ns}$) and high density, which allowed for a compact detector with high detection efficiency and high spatial resolution. On the other hand, the thin LTS and the SC detectors provided an ultra-fast response for the passage of charged particles, without perturbing their energy and trajectory.

The SC, placed between the beam exit window and the PMMA, was directly connected to a scaler module (CAEN V560N), which counted the number of incident primary ions. Furthermore, its time coincidence with the LYSO provided the trigger for the measurement of secondary charged particles and prompt photons. For a given trigger, the LTS together with the LYSO, gave the time of flight measurement of particles impinging in both detectors. This last information is of fundamental importance for the determination of charged particles kinetic energy. Indeed, LYSO crystals can be safely used as calorimeters only for the detection of prompt and PET photons, while for high energy secondary charged particles quenching effects arise, reducing the linearity of the response. Since the energy of secondary particles covered a wide range, the signal coming from the PMT coupled with the LYSO was split and attenuated with three different attenuation factors, before being given to a 12-bit QDC module (CAEN V792N) and avoid its saturation. Finally, in order to discriminate the LYSO signal from its intrinsic background, a threshold on the deposited energy of $\sim 1\,\mathrm{MeV}$ was set. Indeed, the naturally occurring Lutetium consists of a fraction of ^{176}Lu (abundance 2.6%), a long-lived radioactive element including a beta decay and three major simultaneous gamma decays. The main decay process is $^{176}\mathrm{Lu} \rightarrow ^{176}\mathrm{Hf}^{*} + e^{-} + \overline{\nu}_{\mathrm{e}}$, with a maximum energy of the β^{-} particle equal to 596 keV, followed by three simultaneous de-excitation gamma ray emissions, with energies lower that 1 MeV.

3.2.2 Detection of neutral particles

Nuclear interactions of the primary ion beam with the PMMA target lead to the production of neutral particles, such as neutrons and prompt photons. As already discussed in Section 2.2.2, those photons have a leading role in the development of another innovative range monitoring technique, due to their large abundance and the high precision achievable on their emission point reconstruction. Nevertheless, with the detectors already available, the back-pointing reconstruction is still a low efficiency process. A precise experimental knowledge of prompt gamma yields is thus fundamental for the development of new and more efficient monitor devices. While many experiments have already been performed to determine the prompt photon abundance for proton and carbon ion beams, few experimental data are available regarding ^{4}He and ^{16}O beams.

In the HIT experiment, the same devices employed for the detection of charged particles were used for the measurement of prompt photon energy spectra and angular yields at 90° and 60°.

As already explained in Section 3.2.1, the drift chamber can be used to discriminate charged particles from the other secondary products coming from the PMMA. Neutral particles interact rarely with the gas filling the chamber, producing few or no ionisations at all. Thus, an opposite filter can be imposed on data, selecting only those events in which a small number of hits is recorded. Nevertheless, this is still not enough to distinguish and separate the prompt photon signal from the neutrons background. To this end, a two-dimensional histogram of the energy deposited in the LYSO as a function of the measured ToF can be employed, were the ToF is defined as the time difference between signals detected in the LYSO and in the SC. The time

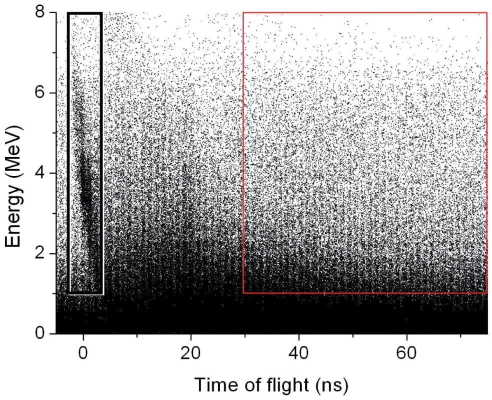

Figure 3.11: Two dimensional spectrum of the energy deposited in a collimated scintillator as a function of the ToF, for secondary particles emitted by a 73 MeV u^{-1} $^{13}C^{6+}$ beam impinging on a PMMA. Detection angle $\theta = 90°$ with respect to the beam axis. Experiment performed at GANIL (Caen, France) [68]. The black selection highlights prompt photons, while the red one highlights neutrons.

of flight of photons is dominated by the speed of light c, meaning that, in such a histogram, photons should all concentrate in a small temporal window preceding the other detected particles. On the contrary, neutrons would be expected to have a broader temporal distribution, less uniform and extended to high values of ToF. This behaviour was observed by *Testa et al.* [68] during an experiment performed at GANIL (Caen, France), as emerges from Figure 3.11: while photons were all concentrated in a small region delimited by the black box, neutrons were distributed in a broader region delimited by the red box.

3.2.3 Detection of fragments

Among the other effects of nuclear interactions of the primary ion beam in the PMMA, hard collisions of the projectile with the target nuclei might lead to the production of fragments from both particles. Those fragments travel at a velocity near to that of the primary ion and for a longer distance, determining a dose-tail behind the Bragg peak, possibly invalidating the positive potential of hadrontherapy in sparing organs at risk. A detailed study of the angular distribution of fragments is then of fundamental importance, in order to determine the amount of extra-dose released in tissues and preserve the organs at risk close to the tumour volume. Nowadays, ^{16}O and ^{4}He ions are being investigated as candidates for particle therapy, due to their high LET and RBE characteristics. The limited data available in literature about these ions, makes it necessary to study fragments abundance and angular yields in order to improve dose conformity in new hadrontherapy techniques. A crucial point in this kind of measurement is the identification of fragments, that can be achieved by means of a $\Delta E - E$ telescope, as suggested by *Gunzert-Marx et al.* [29]. A telescope consists of two different scintillation detectors in sequence: one measuring the energy loss ΔE, and the other measuring the residual energy E, by stopping the particles in it. In the experiment performed at HIT, this was done by means of the STS_2 (EJ-200) and BGO detectors, placed at a distance of 1.2 m from the target at three angular positions (0°, 10° and 30°). The choice of the BGO crystals for this purpose has been driven by their high density and high Z value, which ensured an optimal capability of stopping high energy fragments in a small volume. Furthermore, BGO crystals have a good energy resolution and uniform response to radiation, being the ideal candidates for the detection of charged particles emitted at a small angle with respect to the primary beam direction. Table 3.2 collects some of the main technical characteristics of the scintillation detectors employed in this experiment and described until now. As for the detection of secondary charged particles, a deviation from the linearity of the scintillators response is observed for very high energy fragments. To obtain the kinetic energy of these fragments, then, the information about the time of flight is needed. This was achieved measuring the time difference between signals coming from the STS_1 and STS_2, given a trigger from a SC-BGO coincidence. An example of the expected results for this kind of measurements is shown in Figure 3.12, in which secondary beam fragments produced by $200\,\mathrm{MeV\,u^{-1}}$ $^{12}\mathrm{C}$ ions in water were studied.

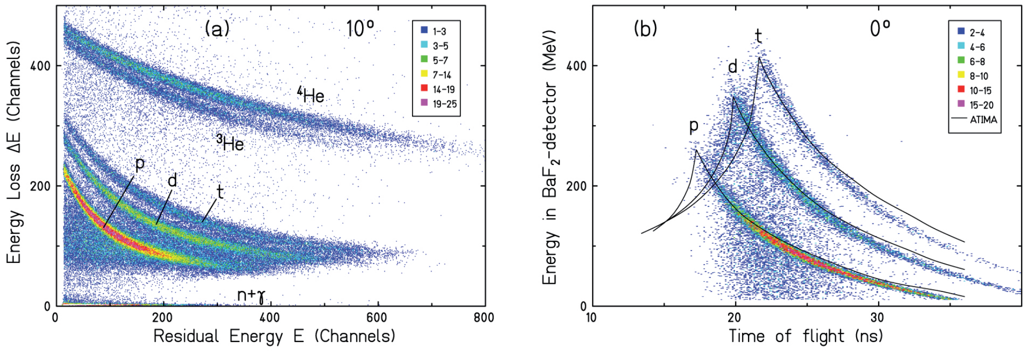

Figure 3.12: Example from the data analysis performed by *Gunzert-Marx et al.* [29]. (a) Correlation of energy loss and residual energy measured with a $\Delta E - E$ telescope: hydrogen and helium isotopes can be well separated. (b) Correlation of particle energy deposited in a BaF_2 scintillation detector and the time of flight, showing escape events at high energies.

3.2.4 Detection of in-beam PET gammas

Besides the direct generation of secondary charged and neutral particles, nuclear interactions of the primary beam with the target can lead to the production of excited nuclei, which decay emitting a positron. The main β^+ emitters studied in the

Table 3.2: Principal characteristics of scintillation detectors employed in the experimental set-up [67].

	Inorganic Scintillators		Organic Scintillator
Material	**BGO**	**LYSO**	**EJ-200**
Composition	$Bi_4Ge_3O_12$	$Lu_{1.8}Y_{0.2}SiO_5$	Polyvinyltoluene
Density $g\,cm^{-3}$	7.13	7.3	1.032
Light Yield	$\sim$ 15 % NaI(Tl)	$\sim$ 75 % NaI(Tl)	64 % Anthracene
Radiation Length cm	1.10	1.16	380
Decay Time ns	300	50	2.1
Peak Wavelength nm	480	420	425
Num. γ/MeV	8200	25 000	10 000
Radioactive	no	yes	no

experiment are ^{11}C, ^{15}O and ^{10}C, having half-lives of 20 minutes, 2 minutes and 20 seconds respectively. At present, PET monitoring techniques already implemented in clinical practice are based on the off-line approach, displacing the patient from the treatment room to another room, or using an in-room PET system just after the treatment. Considering the very small decay times of the radioactive isotopes involved, a lot of information is lost after the beam irradiation and during patient repositioning. One of the purposes of the experiment performed at HIT, thus, was that of developing a new in-beam monitoring technique to be implemented during the treatment. Two small matrices of 23 × 23 pixels of LYSO crystals (Rn and Rs), placed on each side of the PMMA, were used to this end, for the detection of back to back 511 keV gammas. Finally, signals coming from the multi-anode PMTs associated to the detectors could be used to reconstruct the position of the fired pixel, which is necessary in order to evaluate the three-dimensional distribution of the released dose.

3.2.5 Data acquisition

As briefly cited in the previous Sections, many electronic modules of both the VME and NIM standards were used for the experimental Data AcQuisition (DAQ). All the electronic signals were read-out by a VME system (CAEN V271 VME-PCI bridge) interfaced with a computer, while the time and charge informations were acquired using a 19-bit TDC Multi-hit (CAEN V1190B time to digital converter, time resolution of $\sim$ 100 ps), and a 12-bit QDC (CAEN V792N charge to digital converter, resolution of $\sim$ 0.1 pC). The number of impinging ions was counted by means of a VME scaler (CAEN V560 N), using the logic AND of the signals coming from the two PMTs associated to the SC. The VME scaler is capable of sustaining an incoming beam rate up to 100 MHz. Thanks to the primary ion rate provided by the scaler, the acquired data files contained informations about the acquisition Dead Time (DT) efficiency, given by the following formula:

$$\epsilon_{\text{DAQ}} = \frac{N_{\text{acq. ion}}}{N_{\text{ion}}} \tag{3.2}$$

where $N_{\text{acq. ion}}$ is the number of trigger signals acquired by the data acquisition system and N_{ion} is the number of all the generated trigger signals. As shown in Figure 3.13, the DT efficiency varied from 60% to 90%, depending on the beam rate. Average values of ϵ_{DT} for the different data taking conditions (ion species, beam energies and angular configurations) have been used to compute the integrated secondary protons yield, which will be presented in Section 4.6.

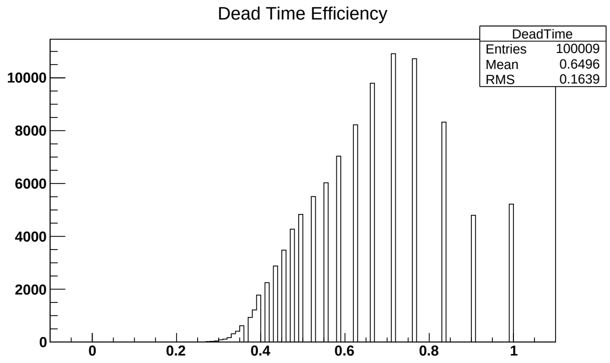

Figure 3.13: Dead time efficiency (ϵ_{DAQ}) for an acquisition with an oxygen beam of $300\,\text{MeV}\,\text{u}^{-1}$.

Finally, the charges associated to the BGO and LYSO scintillators were splitted in three and attenuated by a factor 1/3, 1/12 and 1/72, in order to ensure a large detection energy range with high resolution.

Chapter 4

Data Analysis and Results

In this Chapter, the analysis performed on secondary charged particles emitted by oxygen beams impinging on a PMMA target will be described. Firstly, a brief overview about the preprocessing of collected data will be given in Section 4.1. An introduction to the FLUKA Monte Carlo simulation package will follow in Section 4.2, underlining some aspects of the experimental apparatus simulation. Finally, the actual data analysis carried out during this thesis work will be presented, and the obtained results will be compared to the Monte Carlo predictions. In order to analyse secondary charged particles, a data selection has been performed, and the different isotope species have been identified (refer to Section 4.3). Following particle identification, kinetic energy spectra at detection can be computed exploiting the Time of Flight (ToF) information, as will be presented in Section 4.4. Then, using a reconstruction algorithm of the tracks detected by the drift chamber, the emission vertex coordinates, in both the longitudinal and transverse planes with respect to the primary ion beam direction, can be determined (see Section 4.5). The informations about kinetic energy spectra and reconstructed longitudinal coordinates are of fundamental importance for the calculation of the particle yields at generation, as will be described in Section 4.6. Finally, a possible correlation of the longitudinal emission distribution of secondary charged particles with the beam range inside the PMMA will be proposed in Section 4.7.

4.1 Preliminary analysis

The measurement configurations relative to the collected data sample are summarised in Table 4.1.

Oxygen ion beams of three different energies have been directed to the PMMA target, and the corresponding secondary charged particles have been detected with the DC-LYSO arm in two angular configurations. The length of the PMMA was

Table 4.1: The beam energy, beam spot size (FWHM), beam range (Bragg peak position depth) and PMMA thickness used during the data acquisition with oxygen ions are listed. Two angular configurations were used: θ is the angle at which the DC and LYSO detector were placed with respect to the beam direction.

Ion	Energy (MeV u^{-1})	B_{FWHM} (mm)	Range (cm)	t_{PMMA} (cm)	θ
^{16}O	210	4.6	6.0	7.65	90° − 60°
	260	3.9	8.5	10.00	
	300	3.6	11.0	12.65	

chosen in order to find the Bragg peak position approximately 1 cm before the end of the target, in correspondence to the zero of the reference frame. The ranges of the oxygen beams in PMMA, defined as the Bragg peak depth, were computed using a FLUKA Monte Carlo simulation [69] [70], while the beam spot sizes were known from the HIT beam libraries.

As will be described in the next Sections, a preliminary analysis on the collected data has been done: the subtraction of QDC pedestals and the summation of the three attenuated charge ranges (Section 4.1.1), the LYSO energy calibration (Section 4.1.2), and the time slewing correction of the measured ToF (Section 4.1.3).

4.1.1 Raw data preprocessing

Signals coming from the QDC have a definite pedestal, corresponding to the response of the electronic module to an input of charge zero. The pedestal, therefore, determines the zero of the charge scale, and has to be subtracted from the QDC signal distribution. This is automatically done by the software developed for the data analysis, which models the pedestal with a Gaussian curve and subtracts the obtained mean value from the true signal charge values (see Figure 4.1).

Another key aspect of the raw data preprocessing procedure is the correction for the different attenuations. As presented in Section 3.2.5, the signals coming from the PMT associated to the LYSO have been attenuated by three different factors in order to guarantee a large energy range with a good resolution. In the following, the expressions QDC0, QDC1 and QDC2 will refer to the charges attenuated by a factor 1/3, 1/12, 1/72 respectively. The three attenuated signals have been merged in one via software, scaling the higher attenuated signals to the less ones. To this end, a preliminary cross check on the linearity of the different attenuation factors has been performed, plotting the readout charges as a function of the others (see Figure 4.2), in order to use the correct attenuation coefficient to merge the three charge ranges. The result of the merging of the three attenuated charge distributions is shown in Figure 4.3.

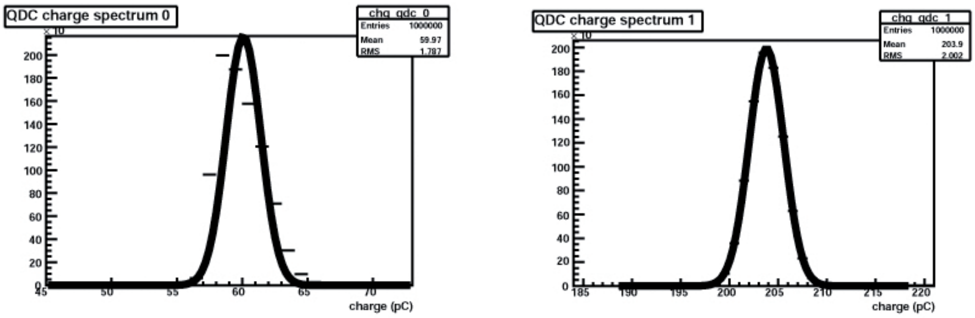

(a) Pedestal charge att. 1/3

(b) Pedestal charge att. 1/12

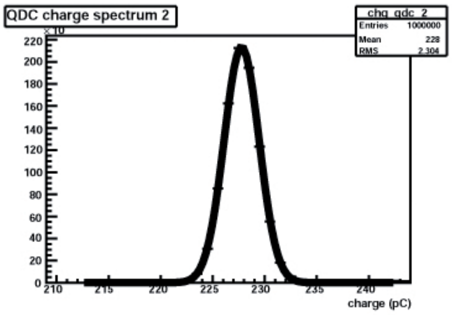

(c) Pedestal charge att. 1/72

Figure 4.1: Gaussian fit of the pedestals of the QDC associated to the LYSO. Channels 0 (a), 1 (b) and 2 (c) correspond to the different attenuations. Acquisition with an oxygen beam of 300 MeV u^{-1}.

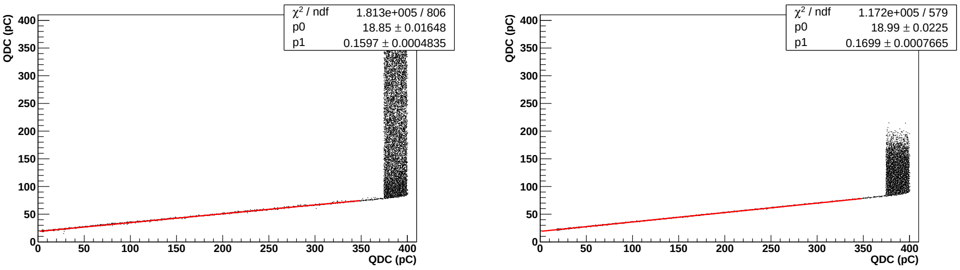

(a) QDC0 vs QDC1

(b) QDC1 vs QDC2

Figure 4.2: Cross-check on the linearity of the three attenuation factors. Each attenuated charge is plotted as a function of the others and a linear relation emerges, as expected. At the end of the linear region, a saturation region can be distinguished. The attenuation factors have been extracted from the linear fit. Acquisition with an oxygen beam of 300 MeV u^{-1}.

4.1.2 LYSO calibration

The LYSO detector has been calibrated exploiting sources above 1 MeV. Apart from the ^{22}Na and ^{60}Co sources, which emit photons of 0.511 MeV and photons of 1.17 MeV and 1.33 MeV respectively, the lifetimes of the other isotopes with high

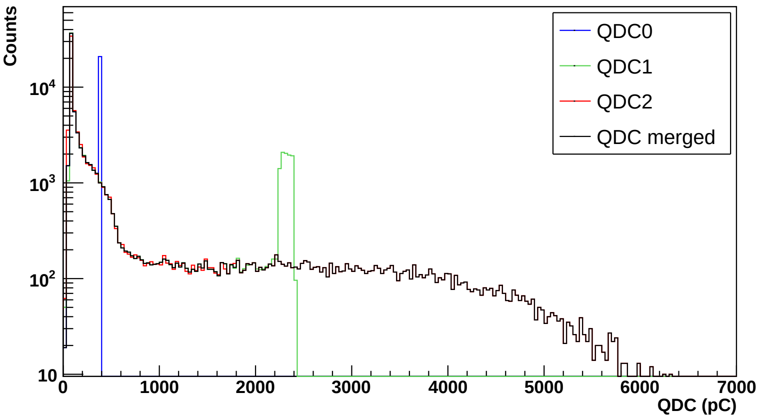

Figure 4.3: Merging of the three charge ranges. The different contributions are shown with different colours, as listed in the legend. Acquisition with an oxygen beam of 300 MeV u^{-1}.

energy emission lines are too low to be useful for a calibration procedure. To overcome this problem, an indirect production mechanism was introduced by *Bellini et al.* [71], using the neutron induced gamma lines from an AmBe source hosted inside a 5 cm thick paraffin ($C_{31}H_{62}$) container. The interaction of the neutrons emitted by the AmBe with the hydrogen of the paraffin produces a 2.22 MeV line from deuteron formation (H(n,γ)d), while the interaction with the carbon produces a 4.44 MeV $^{12}C^{*}$ de-excitation line. Figure 4.4 shows the gamma charge spectrum measured by the LYSO, obtained from the ENEA (Frascati, Italy) AmBe source in the operational conditions used at HIT.

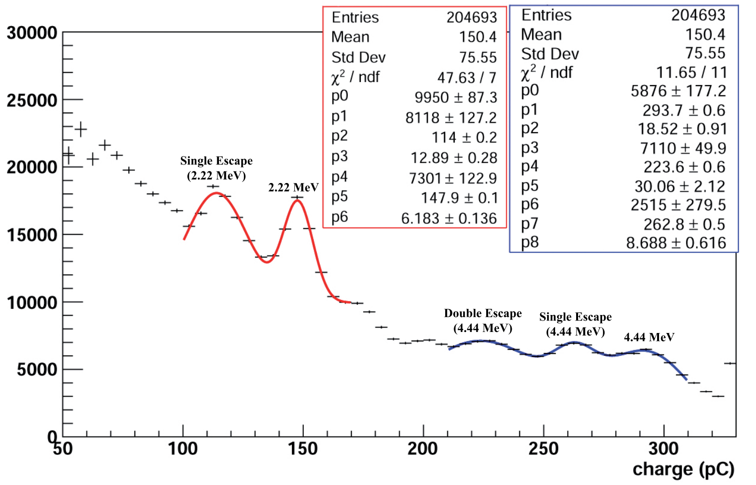

Figure 4.4: Charge spectrum of the LYSO detector obtained with an AmBe source moderated with paraffin. The interpretation of the charge peaks has been done following the analysis in *Bellini et al.*. [71]

In this Figure, the 2.22 and 4.44 MeV lines are clearly visible together with their single escape lines, that occur when a 511 keV photon produced by the annihilation of a positron escapes the detector. In the case of the $^{12}C^{*}$, a double escape peak is also fairly noticeable. The LYSO calibration curve (Figure 4.5) shows a linear dependence of the deposited energy on the QDC counts, in the calibration range $1 \div 5$ MeV.

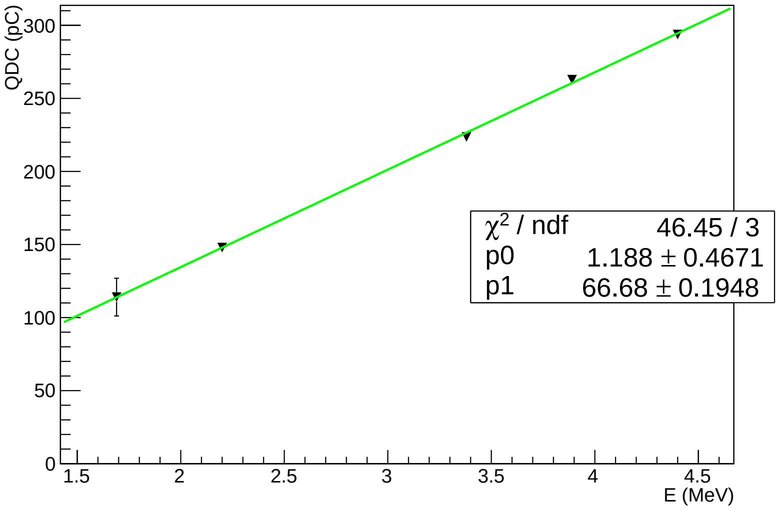

Figure 4.5: LYSO calibration curve used for the conversion of the QDC (charge) values into deposited energy values, in the experiment performed at HIT.

Following the results obtained in the extended calibration energy range study presented in *Bellini et al.* [71], the linearity of the LYSO calibration curve at HIT has been assumed to be valid in the $1 \div 10$ MeV interval (prompt photons detection range).

Since secondary charged particles emitted in the interaction of the ion beam with the target can reach energies much higher than 10 MeV, at HIT an energy calibration for protons was also performed, directly directing primary proton beams of different energies towards the LYSO. However, data collected from these acquisitions could not be used to linearly convert the registered charges into actual energies, due to both quenching effects in the LYSO and saturation of the PMT. On the other hand, those calibration runs have been used to better understand the LYSO detector response to high energy protons, aspect that is fundamental to correctly interpret the secondary charged particle data, which are the subject of this study. As described in Section 3.2.1, the LYSO detector is a matrix of four LYSO crystals. Figure 4.6 shows how the four LYSO crystals respond differently to protons of the same energy, information that has been taken into account in the analysis and in the development of the simulation (see Section 4.2.2). Only, three peaks are clearly visible, since the response of two of the four LYSOs is combined in the last third peak due to crystals resolutions.

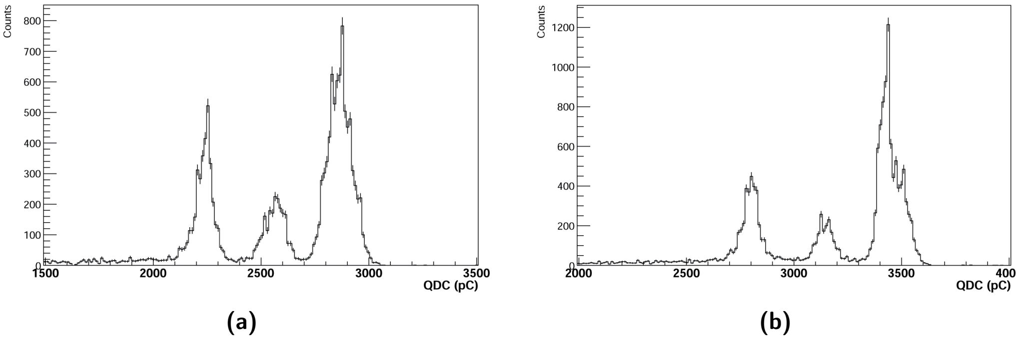

Figure 4.6: Examples of the LYSO response to direct proton irradiations at different energies ((a) 70.03 MeV, (b) 90 MeV). Three different peaks are clearly visible.

Table 4.2: Relative shift in the response of each LYSO crystal, calculated with respect to the one with the lower response (**LY2**). Refer also to Figure 4.7.

LY1	**LY2**	LY3	LY4
1.22	1	1.12	1.17

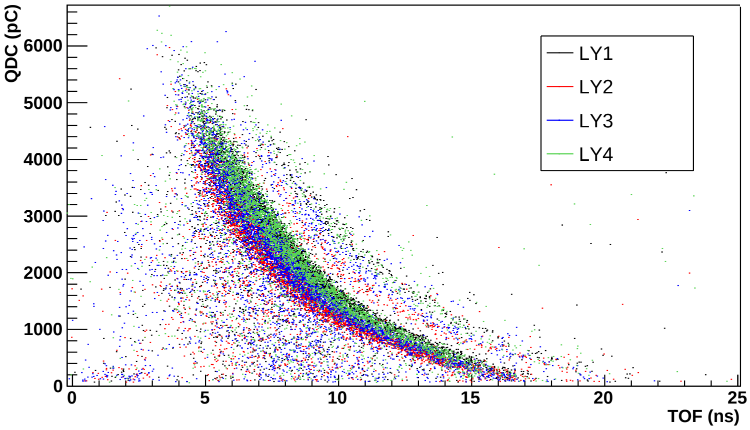

Figure 4.7: Two-dimensional histogram of the charge (QDC) deposited in the LYSO as a function of the time of flight for an oxygen beam of 300 MeV in the 90° configuration. The responses of the different LYSO crystals are shown in different colours, as listed in the legend. The three peak structure can be explained observing that the responses of two of the four LYSOs (LY1 and LY4) are combined due to crystals resolutions.

In the first approximation, a value equal to 2.5% has been obtained for the resolution of all the LYSO crystals, modelling with a Gaussian function the peaks visible in

Figure 4.6. For what concerns the relative shifts in the response of the four LYSOs, a detailed study has been performed, separately on each one of them, with a ^{22}Na calibration source. The results of the relative shifts are presented in Table 4.2, in which the lower LYSO response has been taken as the reference value.
The behaviour of the four LYSO crystals can be observed also from Figure 4.7, where the charge deposited in each LYSO crystal is reported as a function of the ToF of secondary charged particles, selected exploiting the drift chamber information (details in Section 4.3).

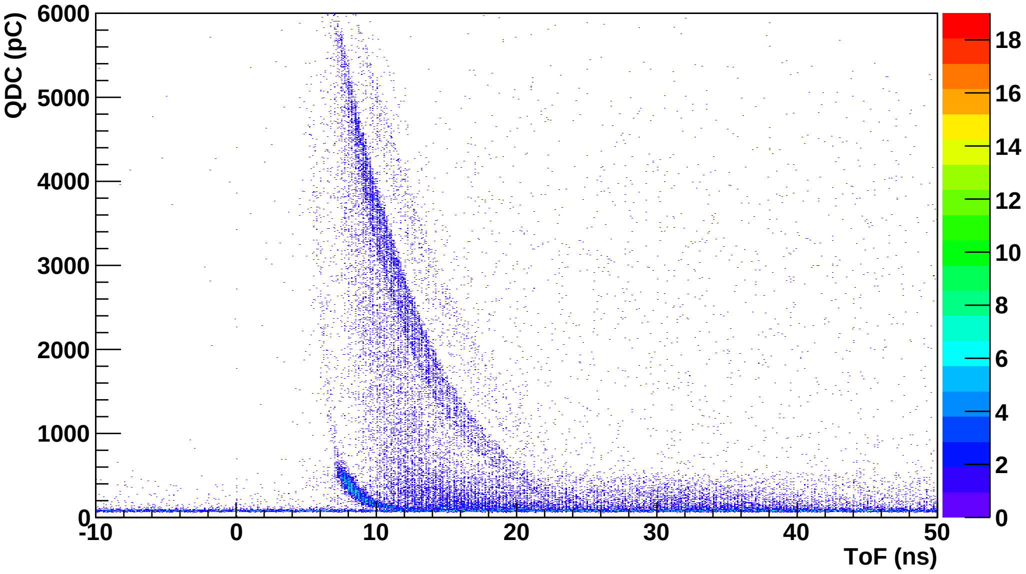

Figure 4.8: Two-dimensional histogram of the charge (QDC) deposited in the LYSO as a function of the ToF (LYSO-SC). Photons can be distinguished for their distribution centred on $\approx 10\,\mathrm{ns}$, while charged particles and neutrons are distributed around higher time values. Acquisition with an oxygen beam of $300\,\mathrm{MeV\,u^{-1}}$.

4.1.3 Time slewing correction

Observing the two-dimensional histogram depicted in Figure 4.8, of the charge collected in the LYSO as a function of the time difference (ToF) between signals in the LYSO and in the SC, a systematic deviation from the expected behaviour emerges clearly.
In Figure 4.8, photons can be easily distinguished from the other particles for their lower and narrower ToF distributions. Since photons have always $\beta = 1$, they should ideally arrange in a vertical band centred on a single ToF value. This is not apparently true when observing the two-dimensional photon distribution in Figure 4.8, which bends toward higher ToF values with the decreasing of the detected charge. The

shape of this distribution is due to an effect induced by the front-end electronics fixed voltage threshold, and it is known as time slewing effect. As represented in Figure 4.9, two signals produced at the same time with different amplitudes cross the voltage threshold at different times, introducing an energy-dependent shift on ToF.

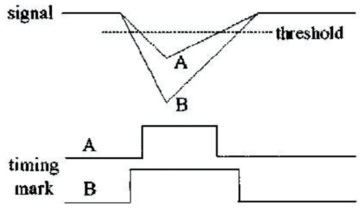

Figure 4.9: Time slewing effect: two signals produced at the same time with different amplitudes cross the voltage threshold at different times.

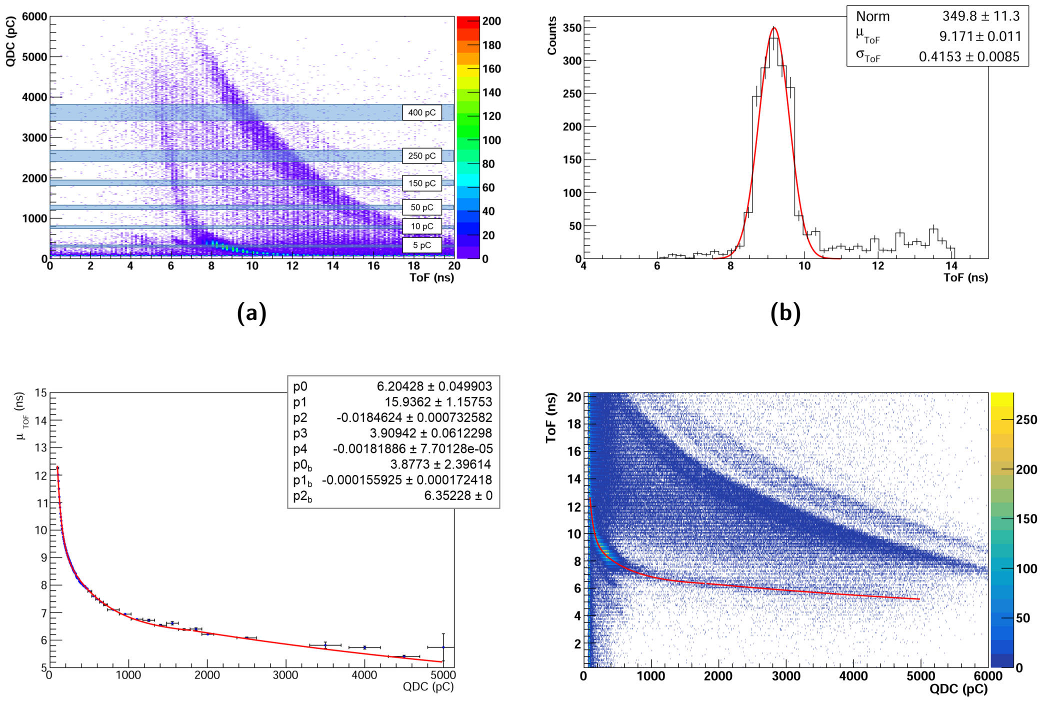

(a) (b)

(c) (d)

Figure 4.10: (a) Two-dimensional histogram of the charge deposited in the LYSO as a function of the ToF (LYSO-SC). QDC windows for the time slewing correction are superimposed. (b) Example of the fit of the ToF distribution in a QDC window (200−205 pC). (c) Mean values of ToF obtained from the different QDC windows as a function of the mean QDC values. The fit function $C(\mathrm{QDC})$ is the sum of two exponential curves (Equation (4.1)). (d) The fit function $C(\mathrm{QDC})$ is drawn on the inverted two-dimensional histogram of the charge versus the time of flight, to check the exact behaviour of the correction. Data acquired with different energies and angular configurations are summed together.

The time slewing effect can be corrected by fitting the ToF distributions in bins of QDC, as shown in Figures 4.10a and 4.10b, thus obtaining the correction curve $C(\mathrm{QDC})$ shown in Figure 4.10c, to be subtracted from a measured ToF distribution. The correction curve $C(\mathrm{QDC})$ has been computed separately in two QDC ranges, and it is given by the following Equation:

$$C(\mathrm{QDC}) = \begin{cases} \mathrm{p0} + \mathrm{p1} \cdot \mathrm{e}^{(\mathrm{p2} \cdot \mathrm{QDC})} + \mathrm{p3} \cdot \mathrm{e}^{(\mathrm{p4} \cdot \mathrm{QDC})} & \mathrm{QDC} \leq 1800 \\ \mathrm{p2_b} - \mathrm{p0_b} \cdot \mathrm{e}^{(\mathrm{p1_b} \cdot 1800)} + \mathrm{p0_b} \cdot \mathrm{e}^{(\mathrm{p1_b} \cdot \mathrm{QDC})} & \mathrm{QDC} > 1800 \end{cases} \tag{4.1}$$

whose parameters are listed in Figure 4.10c.

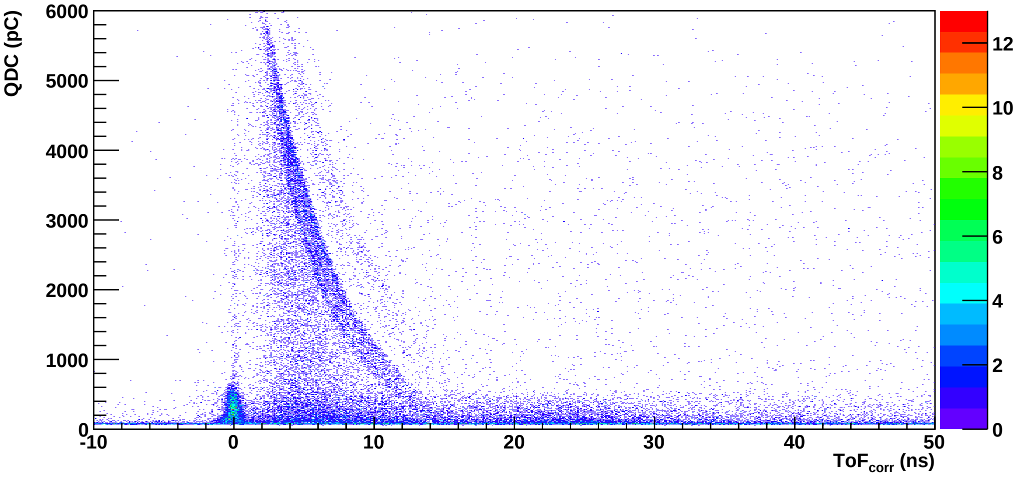

Figure 4.11: Two-dimensional histogram of the charge deposited in the LYSO as a function of the ToF between the Start Counter and the LYSO, corrected for the time slewing effect computed with respect to the photons ToF. Acquisition with an oxygen beam of 300 MeV u^{-1}.

An example of a two-dimensional histogram of the collected charge as a function of the corrected ToF, computed with respect to the photon ToF ($\mathrm{ToF_{corr}} = \mathrm{ToF} - C(\mathrm{QDC})$), is shown in Figure 4.11.

For the secondary charged particles analysis, the ToF has been computed as the time difference between the signals in the LYSO and in the LTS, and the same time slewing correction procedure just described has been applied. In this case, however, few photon signals are detected, and the main contribution at low ToF values is given by secondary electrons emitted in the PMMA, as appears from Figure 4.12. These electrons are mainly due to the Compton scattering of de-excitation photons, produced in the interaction of the beam with the PMMA target.

Since electrons are much faster than heavier secondary charged particles, and have $\beta \simeq 1$, the same considerations made for photons are valid in this case: time slewing correction has been applied taking the electron signal as a reference. While doing

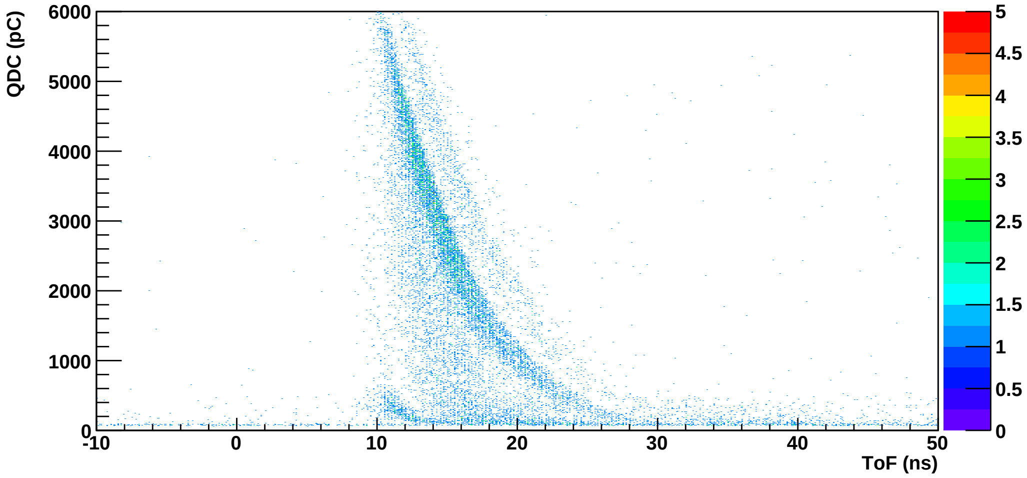

Figure 4.12: Two-dimensional histogram of the charge deposited in the LYSO as a function of the time of flight between the Large Thin Scintillator and the LYSO. Electrons can be distinguished for their low ToF values distribution, while heavier secondary charged particles are distributed around higher time values. Acquisition with an oxygen beam of 300 MeV u^{-1}.

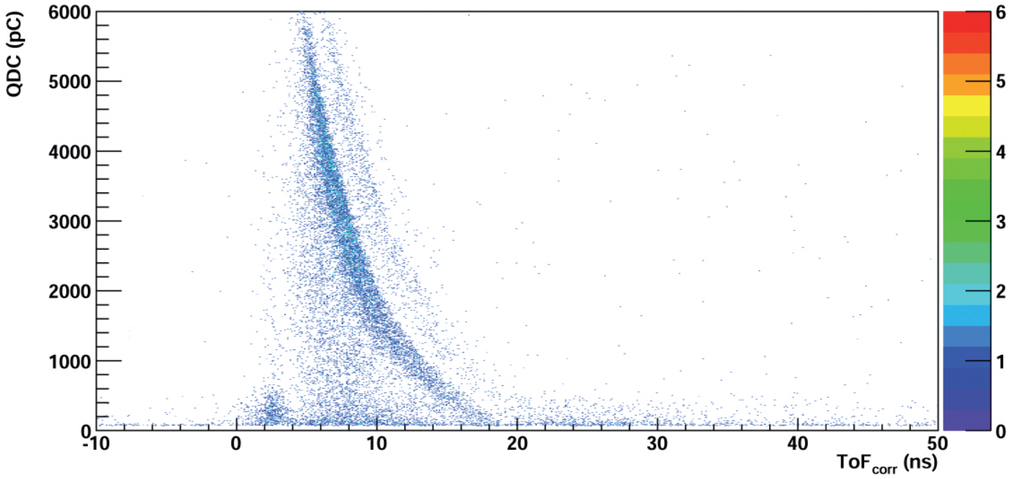

Figure 4.13: Two-dimensional histogram of the charge deposited in the LYSO as a function of the time of flight between the Large Thin Scintillator and the LYSO, corrected for the time slewing effect and electron ToF shift. Acquisition with an oxygen beam of 300 MeV u^{-1}.

so, the true time necessary for the electrons to travel from the LTS to the LYSO has been taken into account. Considering an electron energy $E_\mathrm{e} = 2\,\mathrm{MeV}$ and a LTS-LYSO distance d of $\approx 75\,\mathrm{cm}$, the ToF of the electrons can be evaluated as:

$$\Delta T^{\mathrm{e}}_{\text{Ly-Lts}} = \frac{d}{c}\left[1 - \left(\frac{m_\mathrm{e}c^2}{E_\mathrm{e} + m_\mathrm{e}c^2}\right)^2\right]^{-\frac{1}{2}} \approx 2.5\,\mathrm{ns}. \tag{4.2}$$

Following Equation (4.2), an example of a two-dimensional histogram of the collected charge as a function of the corrected ToF is shown in Figure 4.13.

4.2 FLUKA Monte Carlo simulation code

The experiment performed in this thesis has been complemented with Monte Carlo simulations, in order to asses what to expect from the interactions of an ion beam with a PMMA target. The FLUKA Monte Carlo (MC) code has been chosen, as it is well benchmarked for heavy ion therapy applications. FLUKA is an advanced Monte Carlo simulation package for the calculation of particle transport and interaction with matter, developed from the collaboration of INFN and CERN. FLUKA has a wide range of applications, from high energy experimental physics to cosmic rays studies and medical physics, since it can simulate a large number of different particles covering an energy range from keV to TeV. This multipurpose code rests on sound and updated physical models, based as far as possible on original and well tested microscopic models. The consistency among all the reaction steps is always ensured, and basic conservation laws are fulfilled a priori. As a result, final predictions can be obtained with minimal free parameters, fixed for all energies, targets and projectiles. FLUKA physical models are fully integrated in the code and not modifiable. However, a set of user interface routines, written in Fortran 77, can be used to customise the software and control each step of the simulation. Finally, FLUKA is able to build very complex geometries, using a combinatorial geometry package, and to manage voxel geometries such as patient CTs, which are of particular interest for hadrontherapy applications.

The starting point for the development of a simulation is the definition and programming of all the informations necessary to the software for the processing of data, in other words the *input*. FLUKA inputs are made of a series of command lines, which are called *cards*. The main cards that compose a basic input are the following:

- `DEFAULTS`: Selects predefined physics settings, for example transport thresholds.
- `BEAM` and `BEAMPOS`: Define beam characteristics and beam position and direction.
- `GEOMETRY`: Defines the geometry, which is made of bodies and regions. Bodies are basic geometrical objects, while regions are more complex uniform objects formed from the boolean combination of many bodies.
- `MATERIAL` and `ASSIGNMA`: Define the materials and their assignment to the different regions. FLUKA handles different materials and compounds, that can be also user-defined.

- `RANDOMIZ`, `START` and `STOP`: Initialise the *seed* for the generation of random numbers and the number of primaries, and declares the end of the program.

Apart from these compulsory cards, others can be added for the precise definition of some physical processes, as well as for the scoring of the interesting physical quantities.

For a better management of the different cards, the FLuka Advanced InteRface (FLAIR) can be used, which is an all-in-one user friendly graphical interface. FLAIR is endowed with a fully featured input file editor, and it allows interactive visualisation of the geometry as well as the compilation, running and plotting of the results.

4.2.1 FLUKA nuclear models

As discussed in Section 1.1.4, no rigorous models exist to describe nuclear interactions. FLUKA handles hadron-nucleus interactions with the PEANUT (Pre-Equilibrium Approach to NUclear Thermalisation) model, which simulates the first two stages of nuclear reactions described for protons in 1.1.4. On the other hand, nucleus-nucleus reactions are modelled through interfaces to event generators, which simulate the dynamic stage of hadron-nucleus collisions in two main ways, depending on the energy range [25]. For initial ion energies up to $100\,\mathrm{MeV\,u^{-1}}$ the Boltzmann Master Equation (BME) approach is taken, while higher energies fragmentation processes are described by the relativistic Quantum Molecular Dynamics (rQDM) theory [69].

The **BME** model describes the evolution of the de-excitation of the system of the two interacting nuclei during the pre-equilibrium phase. By solving a set of time-dependent transport equations, the model describes the evolution towards an equilibrium state through a sequence of two body reactions and ejection of unbound particles, whose multiplicity can be calculated [72] [73].

The **rQDM** model describes the interaction of two nuclei starting from their initial state described as a Fermi gas, following the propagation of each nucleon in the potential generated by all others nucleons and described according to a quantum mechanical formalism. The dynamical evolution of particles, the formation of heavy and light fragments and secondary nucleons is then predicted [74] [75].

All the models described until now, are coupled to the internal FLUKA models for the final relaxation step, which include nuclear evaporation, fission, Fermi-breakup and gamma emission.

4.2.2 FLUKA simulation of the experimental apparatus

Besides the correct application of the physical models, an exact implementation of the experimental geometry is crucial to achieve representative simulation results. Therefore, in order to better comprehend the experimental data collected at HIT, a FLUKA MC simulation has been developed, in which the full experimental set-up geometry shown in Figure 3.4 has been reproduced, as depicted in Figure 4.14.

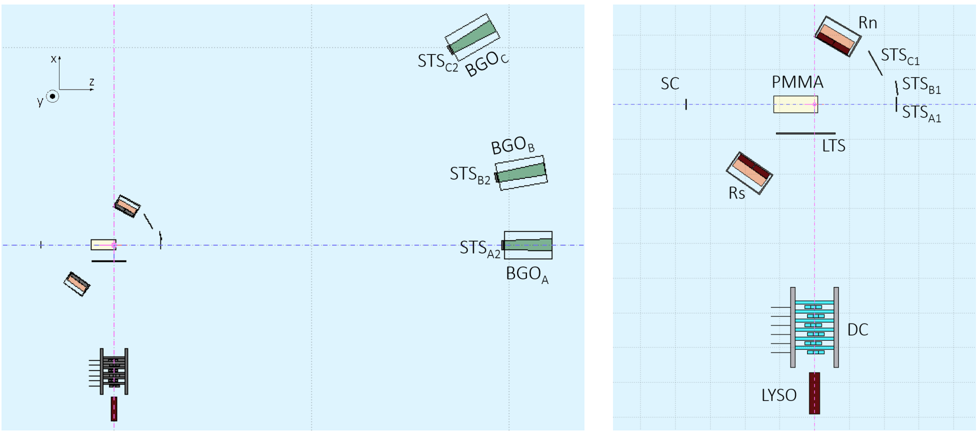

(a) **(b)**

Figure 4.14: Experimental set-up geometry implemented in FLUKA. (a) View of the whole set-up for the experiment performed at HIT, which aimed to measure prompt gammas, gammas from e^+e^- annihilation, forward emitted fragments and secondary charged particles (see Section 3.2). (b) Detail of the experimental set-up section relative to the detection of prompt photons and secondary charged particles at 90° with respect to the beam direction.

Table 4.3 collects the primary oxygen ions statistics generated for the different energies and angular configurations.

Table 4.3: Monte Carlo statistics: generated primary oxygen ions for the different energies and angular configurations.

90°			
Energy (MeV/u)	210	260	300
Primary ions ($\times 10^8$)	11.1	7.55	5.75
60°			
Energy (MeV/u)	210	260	300
Primary ions ($\times 10^8$)	14.05	8.0	2.85

In Figure 4.14b, the drift chamber and LYSO detector can be clearly distinguished. Even if all the components and materials of the DC have been modelled, no true drift process has been implemented in the simulation. Therefore, the response of the simulated DC has been parametrised in order to have the same performances as the experimental one. This parametrisation has been checked to be valid for all different ion beams and energies. For what concerns the LYSO crystals, the different responses seen in Section 4.1.2 have been introduced in the simulation in order to have a faithful energy output to be compared with experimental data. Figure 4.15 shows the four LYSO crystals energy responses as a function of the ToF of secondary protons, to be compared with Figure 4.7).

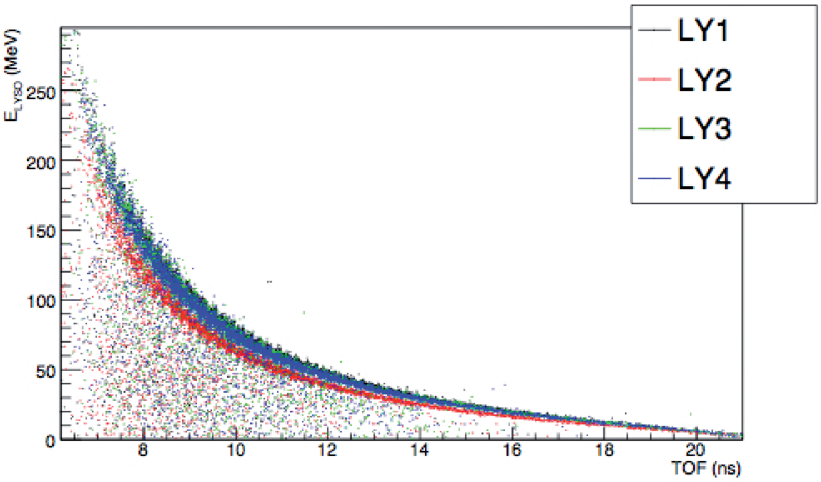

Figure 4.15: Two-dimensional Monte Carlo histogram of the energy measured in the LYSO as a function of the time of flight of secondary protons, for an oxygen beam of 300 MeV u^{-1} in the 90° configuration. The simulated responses of the different LYSO crystals are shown in different colours, as listed in the legend.

The simulated results presented in this work have all been obtained with the `PRECISIO` default, whose main features are the following [76]:

- Rayleigh scattering and inelastic form factor corrections to Compton scattering and Compton profiles activated;
- detailed photoelectric edge treatment and fluorescence photons activated;
- low energy neutron transport on, down to thermal energies included (high energy neutron threshold at 20 MeV);
- fully analogue absorption for low-energy neutrons;
- particle transport threshold set at 100 keV, except neutrons (1×10^{-5} eV);
- multiple scattering threshold at minimum allowed energy, for both primary and secondary charged particles;
- delta ray production on, with threshold 100 keV;

- restricted ionisation fluctuations on, for both hadrons/muons and electromagnetic particles;
- tabulation ratio for hadron/muon dE/dx set at 1.04 with 80 tabulation points, fraction of the kinetic energy to be lost in a step set at 0.05, number of dE/dx;
- heavy particle e^+e^- pair production activated with full explicit production (with the minimum threshold equal to $2m_\mathrm{e}$;
- heavy particle bremsstrahlung activated with explicit photon production above 300 keV;
- heavy fragment transport activated.

In the following Sections, the experimental data will be compared with the Monte Carlo results, reproduced with the simulation just described. Furthermore, a dedicated MC simulation has been also used for the evaluation of the total detector efficiency, necessary to calculate the experimental yields as will be presented in Section 4.6.1.

4.3 Particle identification

For the purpose of the analysis presented in this work, secondary charged particles emitted by oxygen beams impinging on a PMMA need necessarily to be identified and distinguished among the other secondary products detected by the LYSO, in order to be able to determine their yield and reconstruct their spatial emission distributions. To this end, the informations collected by the drift chamber have been used, at least to separate neutral particle driven events from charged ones. Considering the geometrical set-up, a charged particle travelling from the PMMA to the LYSO is likely to hit all the twelve planes of the drift chamber. Therefore, it is possible to perform a first event selection based on the number of hit cells (N_hits) in the drift chamber. Figure 4.16a shows an example of the distribution of N_hits for events detected by the LYSO crystals (red solid line) compared to the corresponding MC distribution (blue dashed line). The Monte Carlo distribution has been normalised to the peak of the experimental N_hits distribution, and the same selection conditions as in the experimental data have been applied ($E_\mathrm{lyso} > 1\,\mathrm{MeV}$ and trigger given by the LYSO and SC time coincidence). In Figure 4.16a a clear peak in correspondence to $N_\mathrm{hits} = 12$ can be easily distinguished, indicating the signature of a secondary charged particle having crossed all the DC planes, firing one cell per plane. The contribution to the data-MC disagreement observed in the $N_\mathrm{hits} \leq 5$ range is mainly

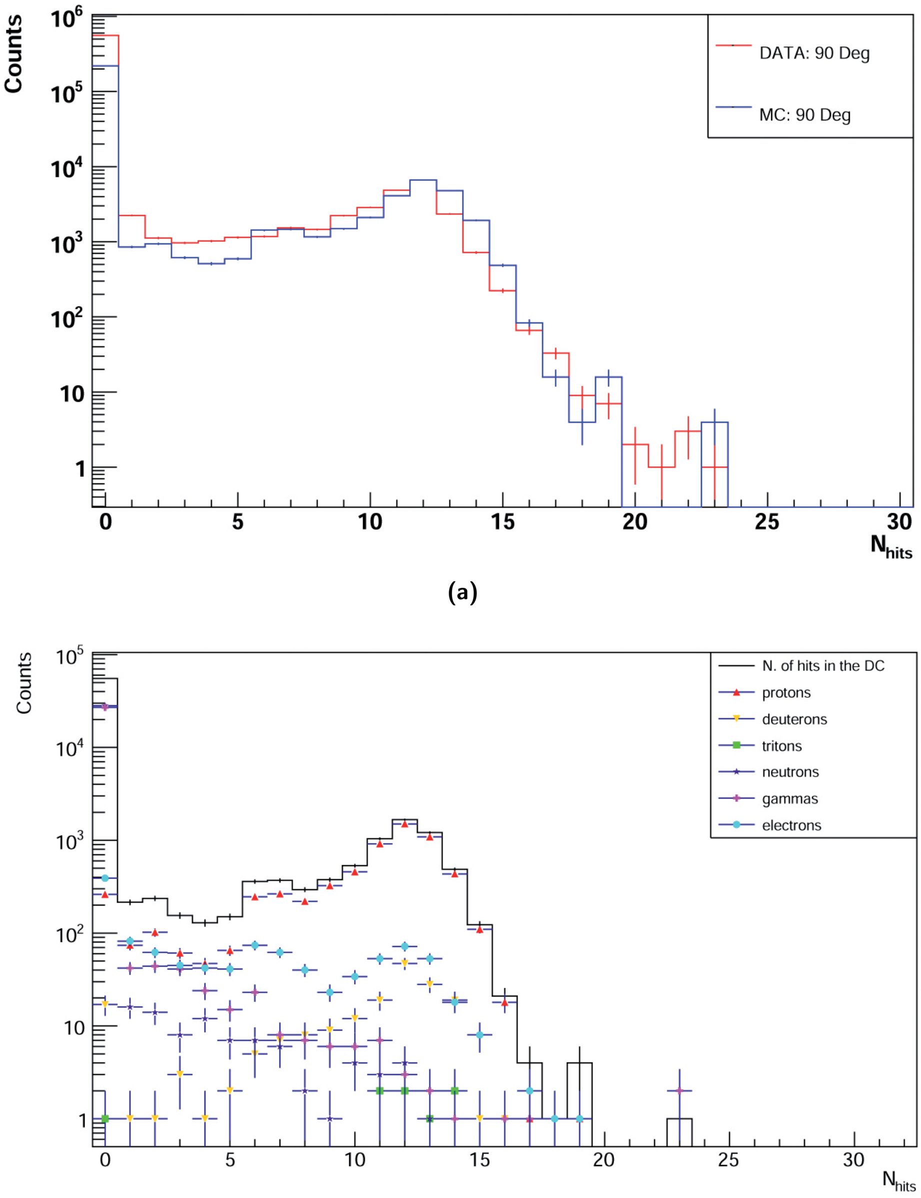

(a)

(b)

Figure 4.16: (a) Data (red solid line) and MC (blue dashed line) distributions of the number of cells hit in the drift chamber (N_{hits}), for events detected by the LYSO crystals ($E_{\text{lyso}} > 1\,\text{MeV}$) in the 90° configuration with a $300\,\text{MeV}\,\text{u}^{-1}$ oxygen beam. (b) MC distribution of the number of cells hit in the drift chamber (solid line), for events detected by the LYSO crystals in the 90° configuration with a $300\,\text{MeV}\,\text{u}^{-1}$ oxygen beam. Individual contributions from protons (up triangles), deuterons (down triangles), tritons (squares), neutrons (stars), gammas (crosses) and electrons (circles) are shown.

due to the absence of a detailed Monte Carlo simulation of the electronics cross-talk and of the beam halo, which may induce particle production.

Figure 4.16b shows the contributions of all the secondary particles to the simulated

N_{hits} distribution (solid black line). This Figure gives an immediate idea on how the different secondary particles interact with the DC: protons are the main contributors to the N_{hits} distribution in the whole range, showing a peak in the $N_{\text{hits}} = 12$ bin; photons and neutrons counts have mainly $N_{\text{hits}} < 7$, while the contribution from electrons is almost constant up to 12. A small presence from deuterons and tritons is also visible. Following the previous consideration, events in which the reconstructed tracks satisfy the $N_{\text{hits}} \geq 8$ requirement have been selected for the analysis of secondary charged particles.

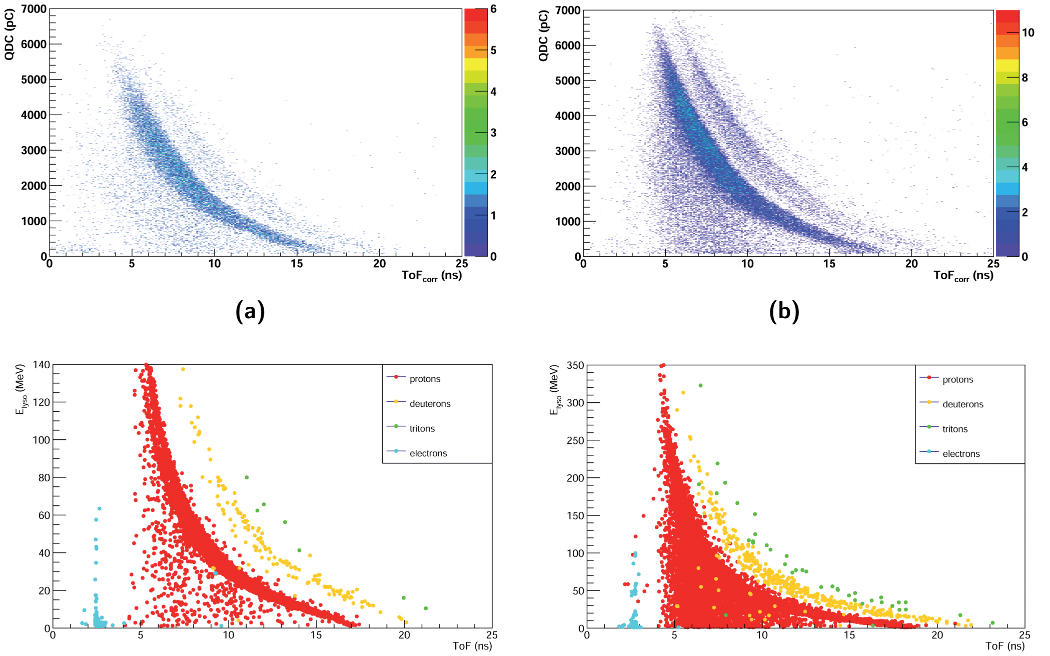

(a) (b)

(c) (d)

Figure 4.17: Top: two-dimensional distributions of the QDC as a function of the corrected ToF for selected particles ($N_{\text{hits}} \geq 8$). Configurations at 90° (a) and 60° (b) for an oxygen beam of 300 MeV u^{-1}. Bottom: two dimensional Monte Carlo histograms of the energy deposited in the LYSO as a function of the ToF for selected particles ($N_{\text{hits}} \geq 8$). Configurations at 90° (c) and 60° (d) for an oxygen beam of 300 MeV u^{-1}. The different secondary particles populations are represented with different colours.

4.3.1 Selection of secondary charged particles

In Figures 4.17a and 4.17b, the plots of the two-dimensional distribution of QDC as a function of the corrected ToF for selected particles ($N_{\text{hits}} \geq 8$) are shown for runs with oxygen beams of 300 MeV u^{-1}, in both the angular configurations (90° – 60°). In order to discriminate the different regions of signal visible in Figures 4.17a and 4.17b, experimental results have been compared with the MC simulation. Figures 4.17c and 4.17d show the two-dimensional Monte Carlo histograms of the energy

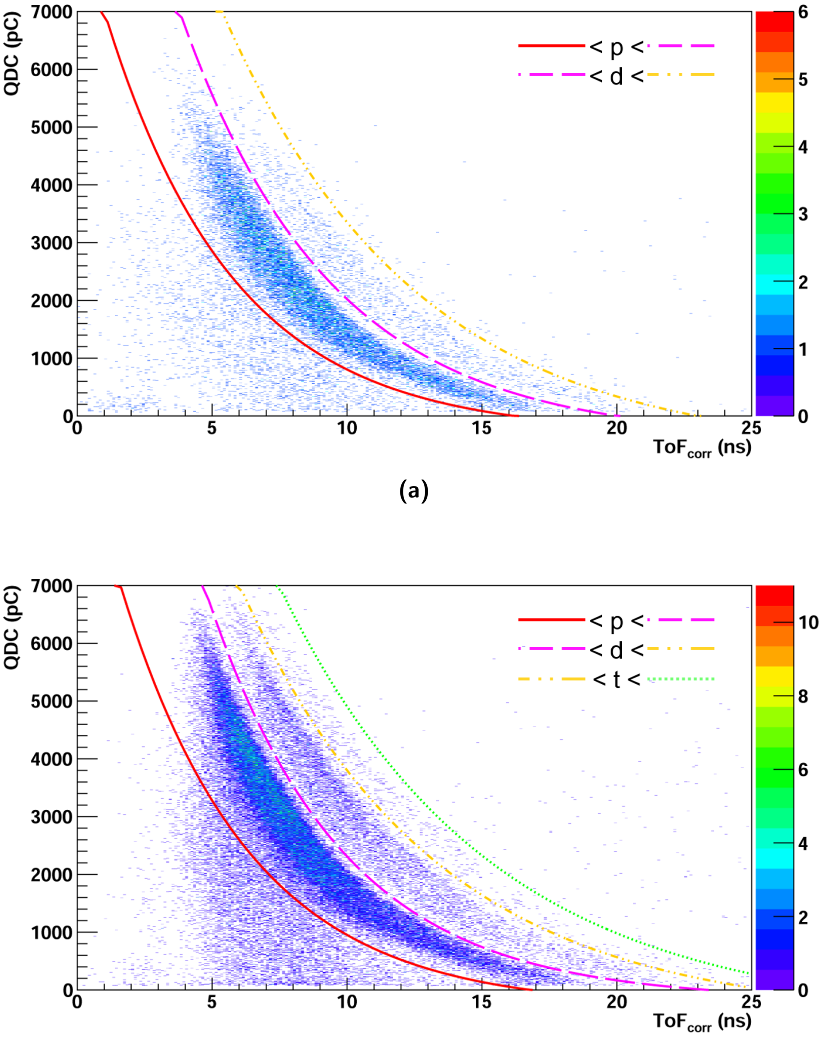

Figure 4.18: Two-dimensional histograms of the QDC as a function of the corrected ToF for selected particles ($N_{\text{hits}} \geq 8$). Configurations at 90° (a) and 60° (b) for an oxygen beam of 300 MeV u^{-1}. The curves for p/d/t selection are superimposed, as listed in the legend.

measured by the LYSO as a function of the ToF. A small amount of electrons can be find in the low-energy region, centred on a ToF value of ~ 2.5 ns. For higher ToFs, two distinct bands can be observed for protons and deuterons, being the one correspondent to protons the most populated. Furthermore, in the 60° configuration a third region corresponding to tritons can be fairly distinguished.

Following the previous considerations on Monte Carlo data, different particle identification functions have been determined, in order to discriminate among the measured charged secondary products. In Figure 4.18, these selection curves are shown, superimposed to the two-dimensional histograms of QDC as a function of ToF.

Details on the proton selection

Comparing the Monte Carlo and experimental data shown in Figure 4.17, someone may observe that protons and other secondary charged particles are not uniquely distributed in well localised bands, but some points diffuse towards lower values of QDC (or E_{lyso} for the MC simulation). The amount of these points is almost negligible: protons outside the selection band are $\sim 10\%$ of the selected proton signal. However, a deeper study has been performed on these scattered points, in order to better understand their source and give an explanation for their behaviour. To this end, the high resources of the FLUKA Monte Carlo simulation have been used to reconstruct the history of protons outside the selection band, in order to understand whether they had a different spatial origin or they deposited a different energy in the LYSO. Since all those protons have been proven to come from an interaction of the primary ion beam inside the PMMA target, the second hypothesis has been taken into account. Following this consideration, protons outside the selection band are expected to have reached the LYSO within a reasonable time of flight, having not released all their energy inside the detector due to some energy escape. To prove this hypothesis, the plot of the energy measured in the LYSO (E_{lyso}) as a function of the particle energy when it crossed the LYSO surface ($E_{\text{kin}}^{\text{cross}}$) has been built for the proton populations both in the band and outside it. This plot is shown in Figure 4.19b, where protons in the band (red) and outside it (blue) are depicted together.

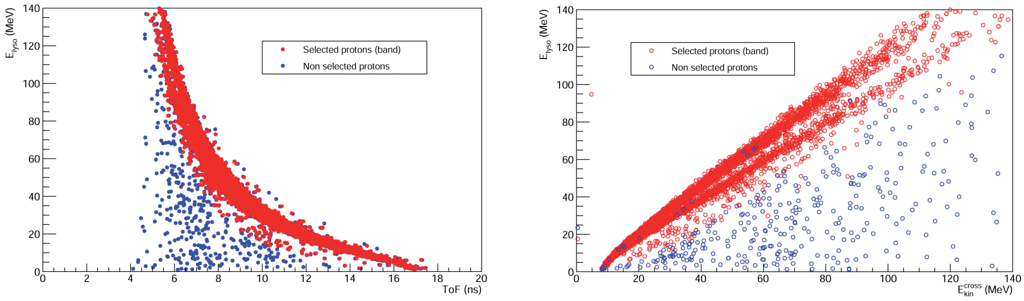

(a) **(b)**

Figure 4.19: (a) Two-dimensional Monte Carlo histogram of the energy deposited in the LYSO by protons as a function of the ToF. Two distinct regions can be observed, corresponding to protons in the selection band (red) and outside it (blue). (b) Plot of the energy measured by the LYSO as a function of the proton energy at the crossing with the detector surface. As expected, selected protons (red) show an almost linear relation, while protons outside the band (blue) are randomly distributed. Configuration at 90° for an oxygen beam of $300\,\text{MeV}\,\text{u}^{-1}$.

As expected, selected protons show a linear relation between E_{lyso} and $E_{\text{kin}}^{\text{cross}}$, while protons outside the band are randomly distributed. The two structures visible in

Figure 4.19b are due to the different LYSO responses, as discussed in Section 4.1.2. Therefore, protons measured outside the selection band have a suitable ToF value and are, in principle, usable for the purpose of the analysis. However, the decision of selecting protons only in the band has been driven by the fact that, in the lower QDC and ToF region of experimental data, there might be contaminations due to noise and other particles, such as electrons and neutrons, which are not easy to take into account.

Another important aspect that needs to be considered is that deuterons and tritons are expected to follow the same behaviour described for protons. This means that some deuterons and tritons will necessarily be included in the selections for protons and deuterons respectively, introducing a systematic error in the evaluation of the yields (see Section 4.6.2).

4.4 Kinetic energy spectra

As presented in Section 4.1.2, an energy calibration of the LYSO up to the several tens of MeV reached by the secondary charged particles cannot be achieved, due to non linear contributions of quenching effects. However, the kinetic energy spectra of these particles represent an important information for monitoring purposes, as fragments emerging from the patient's body have to cross several centimetres of tissue in order to be detected. Knowing the mass of the particle type under consideration, kinetic energy spectra can be obtained from the ToF distributions. In Figure 4.20, the experimental time of flight distributions of secondary protons are shown and compared to the Monte Carlo simulation: a good agreement between the experimental ToF and Monte Carlo distributions emerges, also by comparing the distributions parameters summarised in Table 4.4. Knowing the distance d travelled by the particles from the LTS to the LYSO, it is possible to calculate the kinetic energy of each particle as follows:

$$E_{\mathrm{kin}}^{\mathrm{ToF}} = m_{\mathrm{p}}c^2 \left[\left(1 - \left(\frac{d}{\mathrm{ToF} \cdot c} \right)^2 \right)^{-\frac{1}{2}} - 1 \right]. \tag{4.3}$$

In Equation (4.3), $m_{\mathrm{p}}c^2 = 938.272\,\mathrm{MeV}$ is the proton rest mass, $c = 29.98\,\mathrm{cm\,ns^{-1}}$ is the velocity of light and d is the LTS-LYSO distance, which is equal to 73.5 cm and 77.97 cm in the 90° and 60° configurations respectively.

The kinetic energy spectra obtained with the formula just described, are plotted in Figure 4.21, while Table 4.5 summarises their distribution parameters. As for time of flight distributions, experimental and Monte Carlo kinetic energy spectra

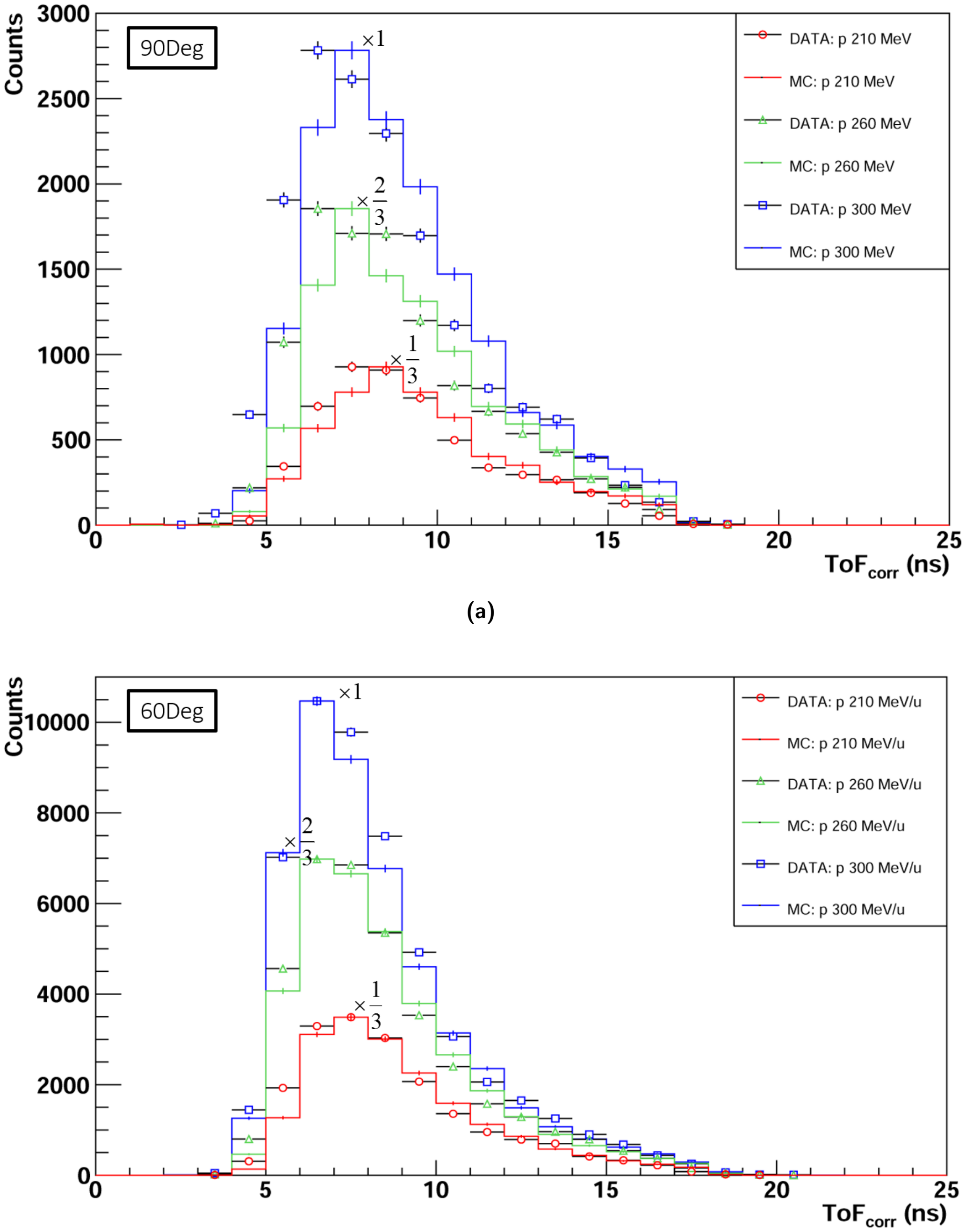

(a)

(b)

Figure 4.20: Time of flight distributions of secondary protons detected at 90° (a) and 60° (b), emitted by oxygen beams of different energies impinging on PMMA. Experimental data (points) are compared with Monte Carlo distributions (solid lines), whose peaks have been normalised to the peaks of the correspondent experimental distributions. Finally, the red and green curves respectively have been arbitrarily scaled to 1/3 and 2/3 of the 300 MeV u^{-1} maximum peak, in order to simplify their visualisation.

Table 4.4: Summary of the time of flight distribution parameters, corresponding to the distributions in Figure 4.20.

Energy (MeV/u)	90°			
	Experimental		Monte Carlo	
	Mean (ns)	RMS (ns)	Mean (ns)	RMS (ns)
210	9.31 ± 0.04	2.66 ± 0.03	9.64 ± 0.06	2.73 ± 0.04
260	8.84 ± 0.05	2.70 ± 0.03	9.29 ± 0.05	2.66 ± 0.03
300	8.55 ± 0.02	2.71 ± 0.02	9.07 ± 0.04	2.66 ± 0.03
Energy (MeV/u)	60°			
	Experimental		Monte Carlo	
	Mean (ns)	RMS (ns)	Mean (ns)	RMS (ns)
210	8.75± 0.02	2.70 ± 0.02	9.01 ± 0.02	2.67 ± 0.01
260	8.47 ± 0.02	2.67 ± 0.01	8.59 ± 0.01	2.64 ± 0.01
300	8.29 ± 0.01	2.61 ± 0.01	8.28 ± 0.02	2.62 ± 0.01

Table 4.5: Summary of the kinetic energy distribution parameters, corresponding to the distributions in Figure 4.21.

Energy (MeV/u)	90°			
	Experimental		Monte Carlo	
	Mean (MeV)	RMS (MeV)	Mean (MeV)	RMS (MeV)
210	44.5 ± 0.4	26.5 ± 0.3	41.2 ± 0.5	28.1 ± 0.3
260	51.8 ± 0.6	33.2 ± 0.4	44.3 ± 0.6	27.9 ± 0.4
300	57.6 ± 0.3	41.0 ± 0.2	47.4 ± 0.3	30.3 ± 0.2
Energy (MeV/u)	60°			
	Experimental		Monte Carlo	
	Mean (MeV)	RMS (MeV)	Mean (MeV)	RMS (MeV)
210	59.4 ± 0.3	36.4 ± 0.2	53.7 ± 0.3	32.4 ± 0.2
260	64.2 ± 0.3	39.1 ± 0.2	60.6 ± 0.3	36.1 ± 0.2
300	67.0 ± 0.2	40.7 ± 0.1	66.5 ± 0.2	39.8 ± 0.1

appear to be in good agreement, aspect that is fundamental in order to validate the selection method applied (see Section 4.3). The energy range of secondary charged particles plays a major role when considering a range-monitoring approach based on their detection. Indeed, only the very high tails of the kinetic energy spectra of these secondaries would emerge from a deep seated tumour, reducing the secondary protons signal sample. In Table 4.6 the percentage of protons with kinetic energies exceeding 40, 60, 80 and 100 MeV are listed.

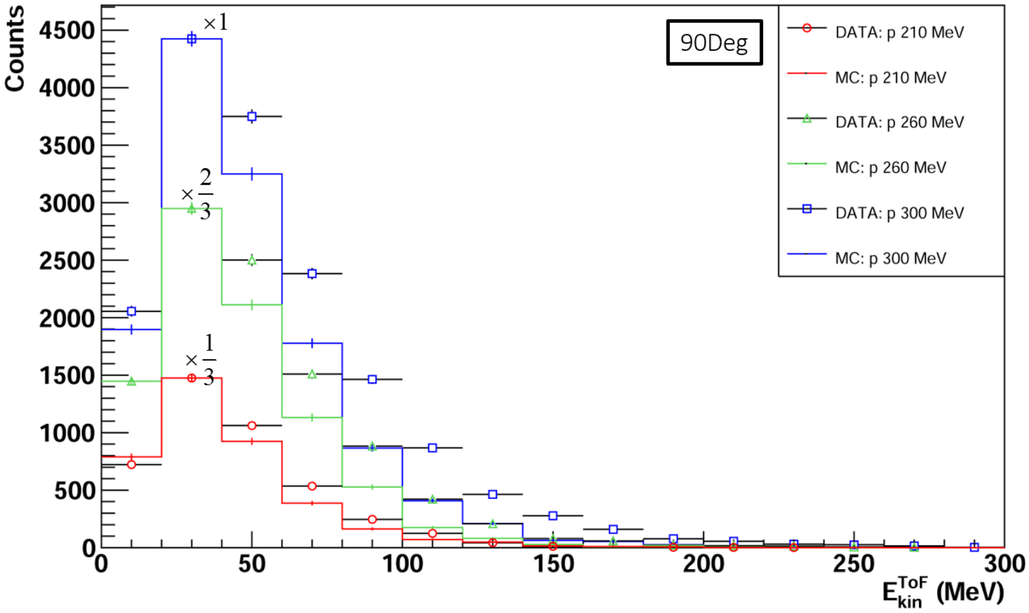

(a)

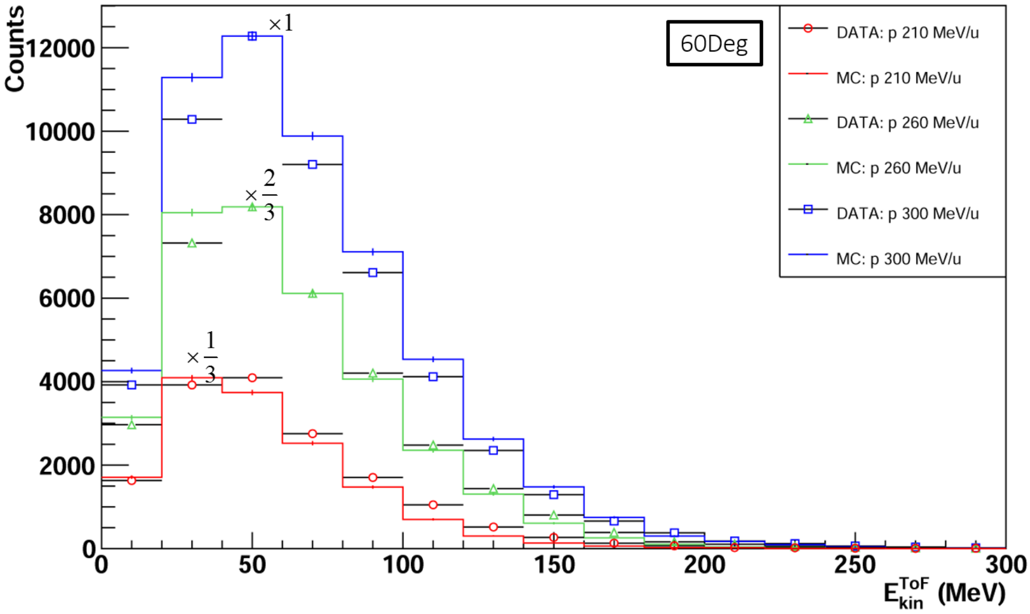

(b)

Figure 4.21: Kinetic energy spectra of secondary protons detected at 90° (a) and 60° (b), emitted by oxygen beams of different energies impinging on PMMA. Experimental data (points) are compared with Monte Carlo simulated distributions (solid lines), whose peaks have been normalised to the peaks of the correspondent experimental distributions. Finally, the red and green curves respectively have been arbitrarily scaled to 1/3 and 2/3 of the 300 MeV u^{-1} maximum peak, in order to simplify their visualisation.

Table 4.6: Percentages of secondary protons with kinetic energies E_p exceeding 40, 60, 80 and 100 MeV).

Energy (MeV/u)	90°			
	$E_\mathrm{p} > 40$ MeV	$E_\mathrm{p} > 60$ MeV	$E_\mathrm{p} > 80$ MeV	$E_\mathrm{p} > 100$ MeV
210	47%	23%	10%	4%
260	57%	32%	17%	8%
300	60%	36%	22%	13%
Energy (MeV/u)	**60°**			
	$E_\mathrm{p} > 40$ MeV	$E_\mathrm{p} > 60$ MeV	$E_\mathrm{p} > 80$ MeV	$E_\mathrm{p} > 100$ MeV
210	66%	40%	24%	13%
260	70%	46%	28%	16%
300	72%	49%	31%	18%

As will be discussed in detail in Section 4.6, the knowledge of kinetic energy spectra, together with the knowledge of longitudinal emission distributions, are fundamental for the calculation of secondary proton yields at production. Indeed, this quantity is of particular interest for the purpose of monitoring in hadrontherapy, since the knowledge of the number of secondary protons produced by an ion beam in a defined material determines the required detector characteristics and the resolution achievable in the reconstruction of the Bragg peak position.

4.5 Spatial emission distributions

The spatial emission distributions of secondary charged particles can be exploited to monitor the range of the primary ion beam inside the target, as will be described in Section 4.7. To this end, the production region of secondary charged particles can be studied extrapolating backwards the tracks reconstructed by the drift chamber to the PMMA position on the (z,y) plane (see Figure 3.4). The extrapolated coordinates, which in the following will be referred to as y_PMMA and z_PMMA, provide the projection of the secondary particles emission point along the primary beam path (z_PMMA, longitudinal emission distribution) and along the vertical direction (y_PMMA, transverse emission distribution).

Figure 4.22 shows the two-dimensional distribution of y_PMMA as a function of z_PMMA for a 300 MeV u^{-1} oxygen ion beam penetrating inside the PMMA target. The dashed lines indicate the beam entrance position (red) and the Bragg peak position (green). The PMMA exit face is at 1 cm.

The measured transverse profiles, shown in Figure 4.23, represent a picture of the Gaussian beams in the vertical direction. The shape of these distributions is affected

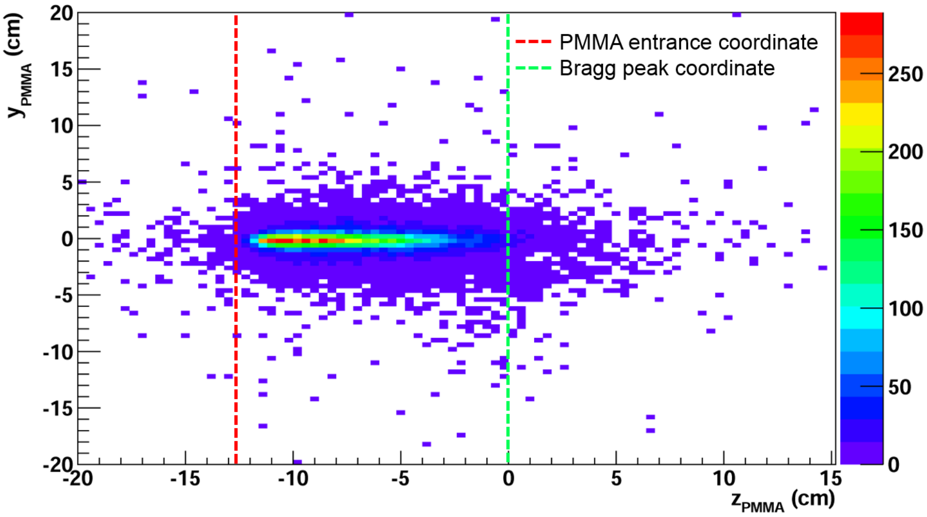

Figure 4.22: Distribution of the emission points (z_{PMMA},y_{PMMA}) of the secondary charged particles for a 300 MeV u^{-1} oxygen beam in the 90° configuration. The vertical dashed line indicate the beam entrance position in the target (red) and the expected Bragg peak position (green).

both by the multiple Coulomb scattering and by the lateral beam spread due to nuclear interactions, which are responsible for the double Gaussian structure visible in Figure 4.23 and schematically represented in Figure 4.24. Furthermore, a high contribution to the width of these transverse emission distributions is given by tertiary protons, which emerge from the reactions of secondary products with the target, and are not directly generated by the primary beam interactions. Due to all these physical processes, the RMS of the reconstructed beam profile is much larger than the nominal beam spot size (see Table 4.1), aspect that is taken into account also when modelling the lateral spread of the dose in clinical practice.

The physical processes previously described become very relevant also when considering the measured longitudinal profiles of secondary charged particles exiting from the PMMA, whose reconstruction can be heavily affected by multiple Coulomb scattering. As might be deduced from Figure 4.25, there is a relation between the shape of the reconstructed longitudinal emission distributions and the Bragg peak position, which in principle makes the use of secondary charged particles feasible for monitoring purposes. Therefore, the precise reconstruction of these distributions is fundamental, in order to provide a good determination of the Bragg peak position inside the patient during the treatment. This topic will be treated in deeper detail in Section 4.7, while in the next Section the procedure followed to determine secondary protons yields and the obtained results will be described.

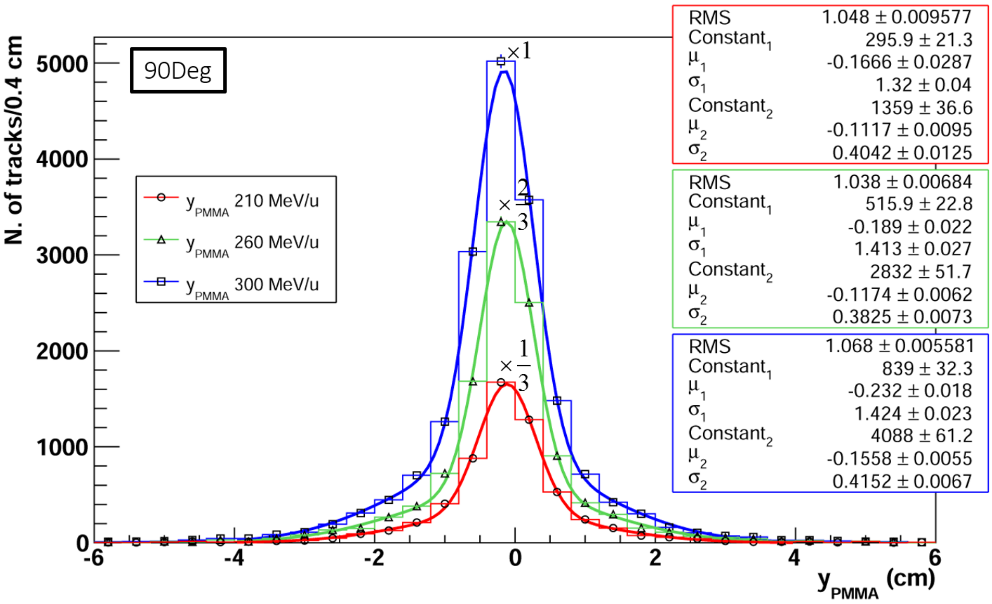

(a)

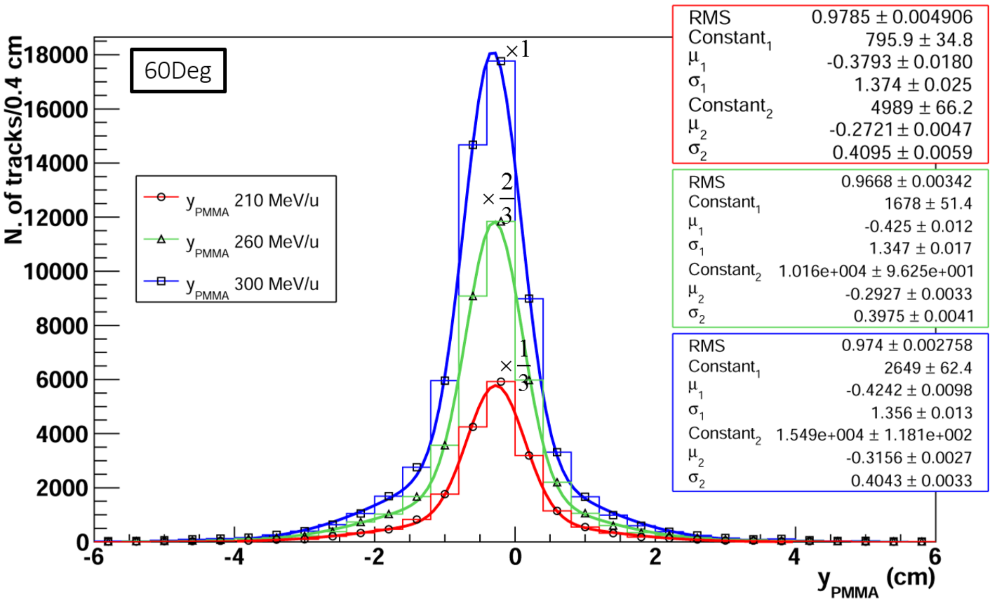

(b)

Figure 4.23: Transverse emission distributions (y_{PMMA}) of secondary charged particles for the different primary oxygen beam energies. (a) 90° configuration. (b) 60° configuration. The y_{PMMA} distributions have been fitted with double Gaussian functions, whose parameters can be seen in the box. Finally, the red and green curves respectively have been arbitrarily scaled to 1/3 and 2/3 of the 300 MeV u^{-1} maximum peak, in order to simplify their visualisation.

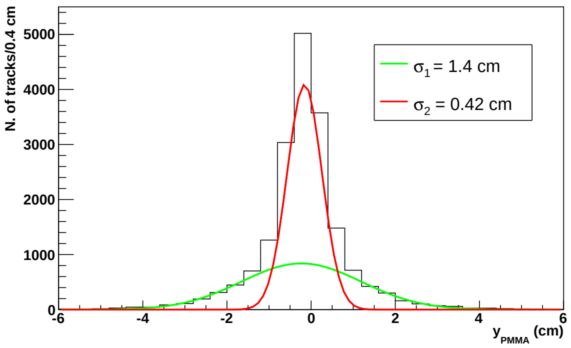

Figure 4.24: Schematic picture of the two Gaussian contributions to the transverse emission distribution. Example with an oxygen beam of 300 MeV u^{-1} in the 90° configuration.

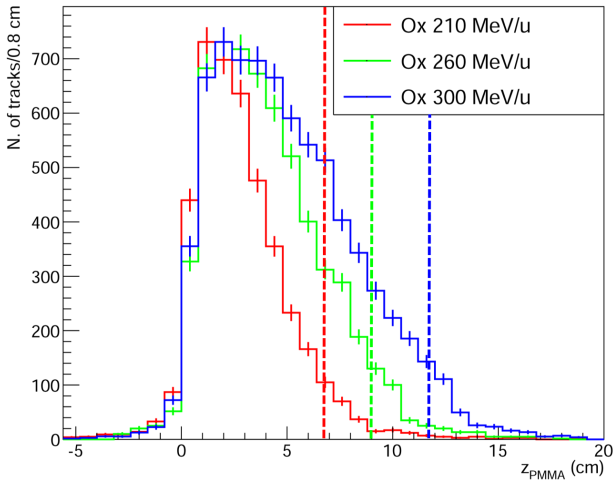

Figure 4.25: Longitudinal emission distributions (z_{PMMA}) of secondary charged particles for the different primary oxygen beam energies in the 90° configuration. The dashed lines indicate the expected Bragg peak positions. The curves have been arbitrarily normalised and shifted, in order to simplify their visualisation. The reconstructed longitudinal emission distributions start growing approximately in correspondence to the beam entrance position inside the PMMA (which has been set arbitrarily on zero for simplicity), reach a maximum after a few centimetres and then decrease again, with a width that depends on the Bragg peak position.

4.6 Secondary proton yields at production

The yield of secondary protons produced by the interaction of the oxygen beam projectiles with the PMMA target, averaged on the total solid angle and integrated over the full target length, has been computed according to the following equation:

$$\Phi_{\mathrm{p}} = \frac{1}{4\pi}\left[\frac{N_{\mathrm{p}}}{N_{\mathrm{O}} \cdot \epsilon_{\mathrm{DT}} \cdot \epsilon_{\mathrm{TOT}} \cdot \epsilon_{\mathrm{SEL}}}\right]^{60^\circ,90^\circ} \tag{4.4}$$

where N_{O} is the total number of primary oxygen ions impinging on the PMMA target, N_p is the number of secondary protons measured by the LYSO, ϵ_DT is the data acquisition dead time efficiency (see Section 3.2.5) and ϵ_SEL is the proton selection efficiency. ϵ_TOT includes the detector and geometrical efficiencies, and can be interpret as the product $\epsilon_\mathrm{DC} \cdot \epsilon_\mathrm{DET} \cdot \epsilon_\mathrm{geo}$, where: ϵ_DC is the drift chamber efficiency in the reconstruction of the tracks, ϵ_DET is the overall detection efficiency, including the LYSO, the DC and the LTS, and finally ϵ_geo is the geometrical efficiency including the detector solid angle.

Among the factors presented in Equation (4.4), N_O and ϵ_DT are computed by means of the VME scaler associated to the SC, as presented in Section 3.2.5, N_p is determined thanks to the selection cuts described in Section 4.3, while ϵ_SEL and ϵ_TOT are unknown quantities that have to be evaluated. The selection efficiency ϵ_SEL has been computed using the FLUKA Monte Carlo simulation described in Section 4.2.2. A method analogous to the one described in Section 4.3.1 has been applied to the two-dimensional MC distributions of the energy E_lyso measured in the LYSO as a function of the ToF, defining the two protons selections curves shown in Figure 4.26. Since the y-axis of the two-dimensional distributions is different between Monte Carlo and experimental data, it was impossible to apply exactly the same cuts previously described (see Figure 4.18). However, two reasonable curves have been determined, which can be safely used for the evaluation of the proton selection efficiency. Knowing the total number of secondary protons measured by the LYSO in the Monte Carlo simulation ($N_\mathrm{p}^\mathrm{tot}$), the proton selection efficiency ϵ_SEL has been computed according to:

$$\epsilon_\mathrm{SEL} = \frac{N_\mathrm{p}^\mathrm{sel}}{N_\mathrm{p}^\mathrm{tot}} \tag{4.5}$$

where $N_\mathrm{p}^\mathrm{sel}$ is the number of protons included between the selection curves shown in Figure 4.26. The obtained ϵ_SEL values are summarised in Table 4.7, for the different energies and angular configurations.

Table 4.7: Computed values of the proton selection efficiency ϵ_SEL.

	90°		
Energy	210 MeV/u	260 MeV/u	300 MeV/u
$\epsilon_\mathrm{SEL}(\times 10^{-1})$	9.37 ± 0.05	9.21 ± 0.05	9.29 ± 0.04
	60°		
Energy	210 MeV/u	260 MeV/u	300 MeV/u
$\epsilon_\mathrm{SEL}(\times 10^{-1})$	9.15 ± 0.02	9.04 ± 0.02	8.94 ± 0.02

In order to compute the total efficiency ϵ_TOT, a dedicated high-statistics FLUKA

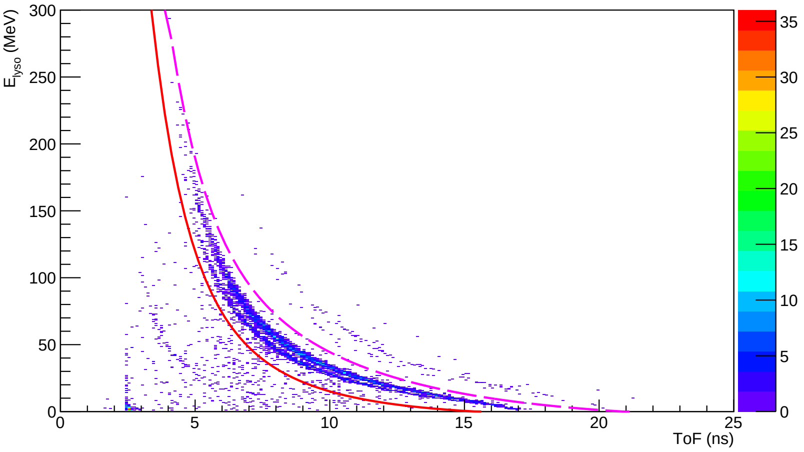

(a)

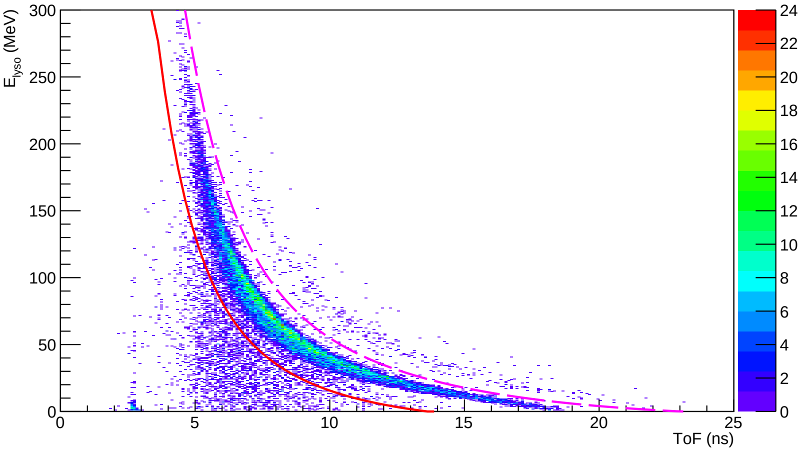

(b)

Figure 4.26: Two-dimensional MC distributions of the energy measured in the LYSO as a function of ToF for selected particles ($N_{\text{hits}} \geq 8$). Configurations at 90° (a) and 60° (b) for an oxygen beam of $300\,\text{MeV}\,\text{u}^{-1}$. The curves for p selection are superimposed.

Monte Carlo simulation has been developed, to be used also for the analysis of the data sets measured with ^{12}C and ^{4}He ion beams, which are not subject of this thesis. In the next Section, the MC simulation and the method followed to compute the total efficiency will be described in detail.

4.6.1 Total efficiency

In many areas of experimental particle and nuclear physics, the efficiencies of the detectors used to record the particles are evaluated by Monte Carlo simulations, which usually include a generator for the production of well known events and a detailed simulation of the experimental apparatus. The same approach has been adopted for the analysis presented in this thesis, with the development of a dedicated high-statistics FLUKA MC simulation for the evaluation of the total proton detection and geometrical efficiency. In this simulation, the same experimental set-up described in Section 4.2.2 has been implemented, the source of the simulated events being the major difference. Since the aim of this simulation is to evaluate the performance of the whole system of detectors in response to secondary incident protons, these particles have been directly generated within a PMMA cylinder of radius 2.5 cm and length equal to 12.65 cm. The axis of the PMMA cylinder has been aligned with the z-axis of the reference frame, and placed in the z range $[-11.65, 1]$cm, as was the PMMA target during the experimental data acquisition with a $300\,\mathrm{MeV\,u^{-1}}$ oxygen beam. Protons have been generated with a continuous energy spectrum in the $[10, 250]$MeV energy range, uniform longitudinal emission distribution from -11.65 cm to 1 cm, Gaussian profile with sigma $\sigma_{\mathrm{prod}} = 0.4\,\mathrm{cm}$ in both the (y, z) and (z, x) planes and emitted in a cone of angular semi-aperture $\theta_{\mathrm{prod}} = 20^\circ$ in the direction of the LYSO position in the 90° angular configuration. The decision of developing a dedicated simulation, rather than exploiting the already existing one, has been driven by considerations of different nature: first of all, the simulation with the protons source does not depend on the specific ion beam type or on the primary beam energy, since the simulated data sample can be easily cut in order to adapt to the various PMMA target lengths. Therefore the generated Monte Carlo output can be used to evaluate the total proton detection efficiency for all the different experimental data acquisitions, heavily reducing the MC computational times. Secondly, in order to obtain the high statistics (3×10^9 protons) necessary for efficiency calculations, the full simulation presented in Section 4.2.2 would require ten times more generated primary events, which are not viable due to long computational times. Given the output of the dedicated simulation, the produced Monte Carlo data have been run through the standard event reconstruction and analysis software, and compared with the generated events in order to evaluate the efficiency. From the statistical point of view, this procedure can be simplified by the comparison of two histograms: histogram A, plotting the distribution of the quantities of interest as generated by the simulation, and histogram B plotting the distribution of the same quantities as they appear after the reconstruction and selection criteria. Intuitively, the best estimate for the unknown true efficiency for each bin can be computed as

$$\epsilon_{\mathrm{i}} = \frac{k_{\mathrm{i}}}{n_{\mathrm{i}}} \tag{4.6}$$

where k_{i} is the number of entries in bin i of histogram B and n_{i} is the number of entries in bin i of histogram A.

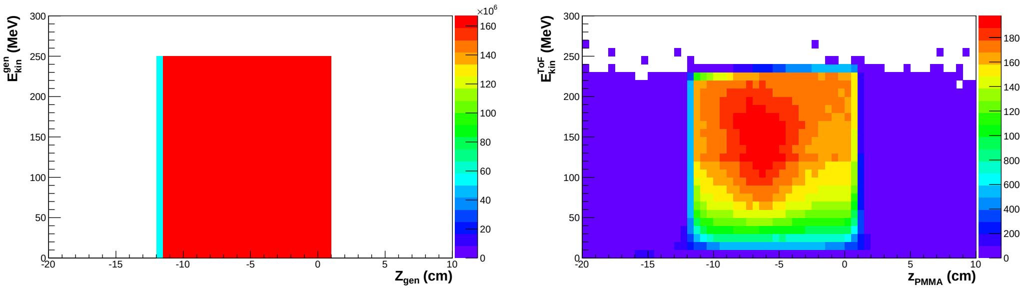

(a) **(b)**

Figure 4.27: (a) Two-dimensional histogram of the kinetic energy at generation ($E_{\text{kin}}^{\text{gen}}$) as a function of the longitudinal emission distribution at generation (z_{gen}). Since protons are generated with a continuous energy spectrum and uniform longitudinal emission distribution, the histogram is flat apart from the first bin in z_{gen}, which has been scaled in order to take into account the true initial coordinate of generation ($-11.65\,\text{cm}$). (b) Two-dimensional histogram of the kinetic energy evaluated from ToF ($E_{\text{kin}}^{\text{ToF}}$) as a function of the reconstructed longitudinal emission distribution z_{PMMA}. As can be seen, some particles are reconstructed outside the generation range.

The total proton detection efficiency for the experimental set-up considered in this work (see Figure 3.4) will generally depend on the energy and coordinate of production of secondary protons emitted in the PMMA. Therefore, the histogram A will be the two-dimensional distribution of the kinetic energy $E_{\text{kin}}^{\text{gen}}$ as a function of the coordinate of generation z_{gen} (see Figure 4.27a); the histogram B will be the two-dimensional distribution of the energy evaluated from ToF, $E_{\text{kin}}^{\text{ToF}}$, as a function of the reconstructed longitudinal coordinate z_{PMMA} (see Figure 4.27b).

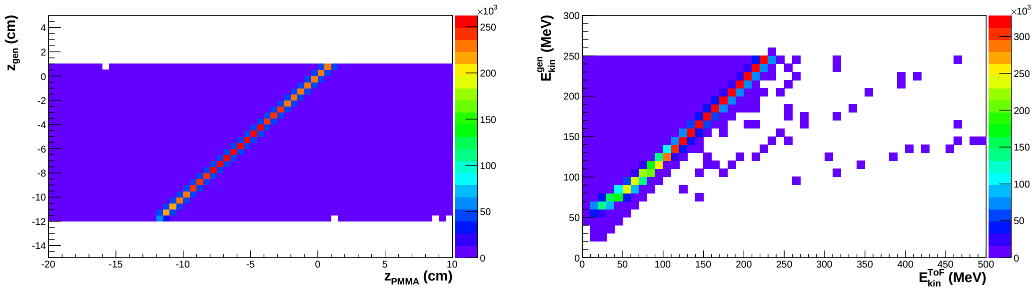

(a) **(b)**

Figure 4.28: (a) Two-dimensional histogram of the longitudinal emission coordinate at generation (z_{gen}) as a function of the reconstructed one (z_{PMMA}). A linear relation exists between the two variables. (b) Two-dimensional histogram of the kinetic energy at generation ($E_{\text{kin}}^{\text{gen}}$) as a function of the energy evaluated from ToF ($E_{\text{kin}}^{\text{ToF}}$). The linearity between the two variables is proven.

As can be observed in Figure 4.27b, some particles are reconstructed outside the generation range, and are therefore excluded from the calculation. Furthermore, a binning equal to 0.5 cm in z and 10 MeV in E_{kin} has been chosen to easily apply the correction to data. Since with this choice the first bin in z starts from -12.00 cm and not from -11.65 cm, the entries in the first bin have been conveniently scaled, as appears also from Figure 4.27a. In order to evaluate the bin per bin efficiency with the formula in Equation (4.6), a one to one relation must hold between variables at generation and the reconstructed ones for each bin. The linearity has been checked by means of the distributions shown if Figure 4.28, which clearly prove the existence of a linear relation between reconstructed and generated variables.

Following these preliminary considerations, the bin per bin efficiency has been computed from the MC simulation, dividing the number of entries in each bean of the histogram in Figure 4.27b by the number of generated protons in that bin, plotted in Figure 4.27a. The outcome of this calculation is shown in Figure 4.29 for both the 90° and 60° configurations.

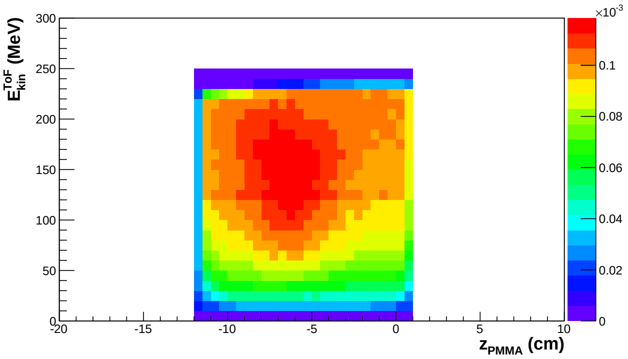

(a)

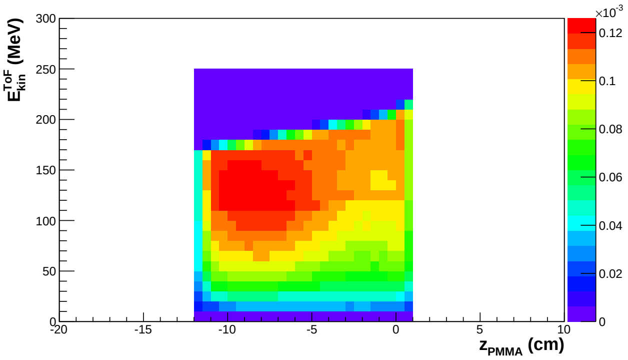

(b)

Figure 4.29: Efficiency matrices for the (a) 90° and (b) 60° configurations: the color scale represents the value of the efficiency in each bin, as a function of the energy evaluated from ToF ($E_{\mathrm{kin}}^{\mathrm{ToF}}$) and of the reconstructed longitudinal emission distribution (z_{PMMA}).

The efficiency error has been calculated following the guidance of *Ullrich et al.* [77], considering a probability density function which slightly differs from the standard binomial probability, given by the following:

$$P(\epsilon_\mathrm{i}; k_\mathrm{i}, n_\mathrm{i}) = \frac{(n_\mathrm{i}+1)!}{k_\mathrm{i}!(n_\mathrm{i}-k_\mathrm{i})!}\epsilon^{k_\mathrm{i}}(1-\epsilon_\mathrm{i})^{n_\mathrm{i}-k_\mathrm{i}}. \tag{4.7}$$

Indeed, the standard approach is based on the knowledge that the application of a cut can be considered as a binomial process with a probability of success ϵ_i and variance $\sigma^2(\epsilon_\mathrm{i}) = \left[\epsilon_\mathrm{i}\,(1-\epsilon_\mathrm{i})\right]/n_\mathrm{i}$. However, it leads to absurd results in the limiting cases:

1. in the case $k_\mathrm{i} = 0$ an unphysical zero error is obtained;

2. in the other limit, $k_\mathrm{i} = n_\mathrm{i}$ the formula again yields to a zero error.

The previous considerations violate reasonable expectations, since the calculation claims for perfect certainty in the measure of the zero efficiency. This problem can be overcome considering the probability density function in Equation (4.7), which leads to the following result for the variance:

$$\begin{aligned}\sigma^2(\epsilon_\mathrm{i}) &= \int_0^1 \epsilon_\mathrm{i}^2 P(\epsilon_\mathrm{i}; k_\mathrm{i}, n_\mathrm{i})\,\mathrm{d}\epsilon_\mathrm{i} - \overline{\epsilon_\mathrm{i}}^2 \\ &= \frac{(k_\mathrm{i}+1)(k_\mathrm{i}+2)}{(n_\mathrm{i}+2)(n_\mathrm{i}+3)} - \frac{(k_\mathrm{i}+1)^2}{(n_\mathrm{i}+2)^2}.\end{aligned} \tag{4.8}$$

The variance computed in Equation 4.8 behaves correctly in the two extreme cases, for $k_\mathrm{i} = 0$ and $k_\mathrm{i} = n_\mathrm{i}$, being $\sigma^2(\epsilon_\mathrm{i})|_{k_\mathrm{i}=0,n_\mathrm{i}} > 0$. Further details about the method applied for the efficiency error calculation are reported in reference [77].

4.6.2 Evaluation of proton yields

In order to calculate proton yields at production, the efficiency matrices shown in Figure 4.29 have been applied to the two-dimensional experimental distributions of the kinetic energy evaluated from ToF as a function of the reconstructed longitudinal emission distribution, shown in Figure 4.30 for the 90° configuration. Therefore, Equation (4.4), presented at the beginning of Section 4.6, has been adapted as follows:

$$\Phi_\mathrm{p} = \frac{1}{4\pi}\left[\left(\sum_\mathrm{i}\frac{N_\mathrm{p}^\mathrm{i}}{\epsilon_\mathrm{TOT}^\mathrm{i}}\right)\frac{1}{N_\mathrm{O}\cdot\epsilon_\mathrm{DT}\cdot\epsilon_\mathrm{SEL}}\right]^{60^\circ,90^\circ} \tag{4.9}$$

where N_p^i and $\epsilon_\mathrm{TOT}^\mathrm{i}$ are, respectively, the number of detected protons and the total proton efficiency of each bin of the $E_\mathrm{kin}^\mathrm{ToF}$ as a function of z_PMMA two-dimensional histogram.

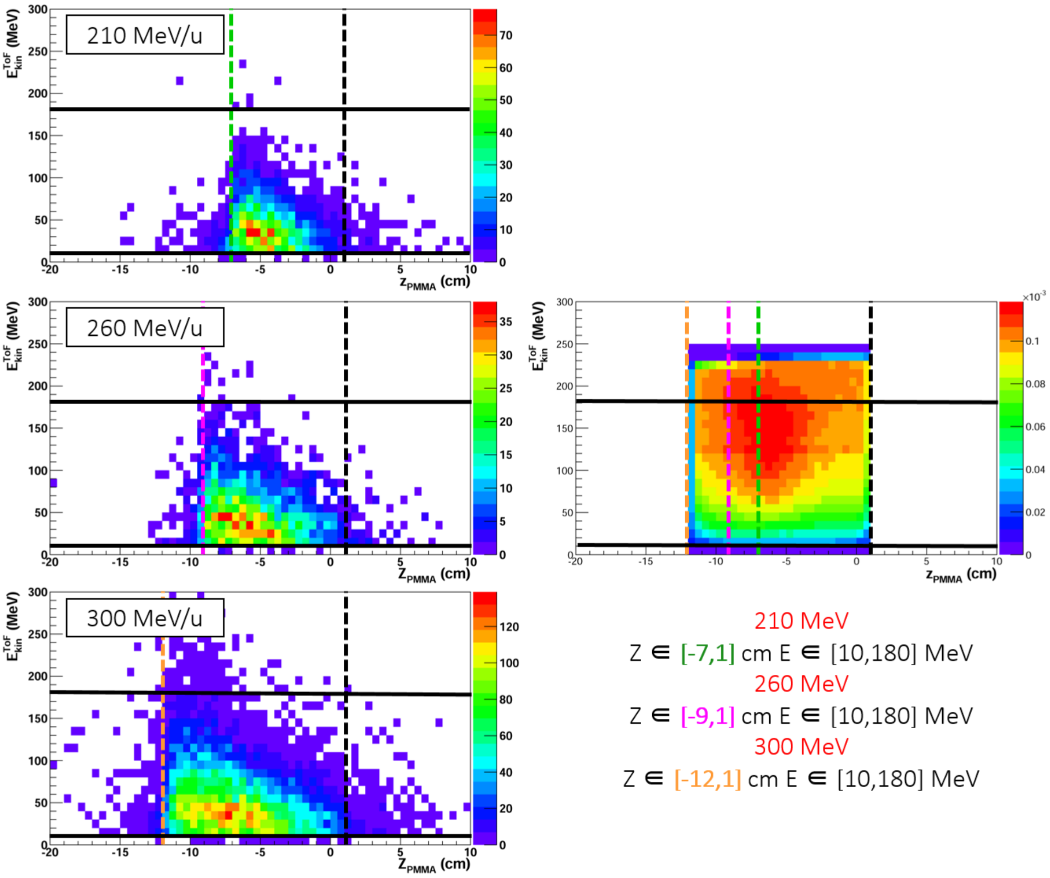

Figure 4.30: Left: Two-dimensional histograms of $E_{\mathrm{kin}}^{\mathrm{ToF}}$ as a function of z_{PMMA} for the different beam energies in the 90° angular configuration. Right: Efficiency matrix to be applied on data. The solid lines correspond to the cuts on the energy range, while the dashed lines correspond to the cuts on z_{PMMA} depending on the primary beam energy.

As shown in Figure 4.30, the calculation of yields has been performed in a restricted energy range in order to avoid the problems arising from very low statistics in some bins of the experimental data histograms. Therefore, the values obtained for the yields are to be considered as preliminary, and further studies are necessary in order to improve the efficiency calculation method and to overcome biased results due to edge effects. Furthermore, depending on the energy of the primary oxygen beam, the efficiency matrix has been cut along z in order to adapt it to the actual PMMA dimensions, as can be seen in Figure 4.30. The same procedure has been applied for the 60° configuration. The mean efficiency values obtained after the cuts for the different energies and angular configurations are listed in Table 4.8.

Table 4.9 collects the production yields of protons (Φ_{p}) produced by oxygen beams of different energies in the angular configurations at 90° and 60°, with a kinetic energy $10\,\mathrm{MeV} \leq E_{\mathrm{kin}}^{\mathrm{ToF}} \leq 180\,\mathrm{MeV}$, integrated over the full target size and averaged

Table 4.8: Computed mean values of the proton efficiency ϵ_{TOT}. The errors associated to the efficiency have been evaluated from Equation 4.8.

	90°		
Energy	210 MeV/u	260 MeV/u	300 MeV/u
$\epsilon_{\mathrm{TOT}}(\times 10^{-5})$	6.393 ± 0.003	6.648 ± 0.003	6.677 ± 0.001
	60°		
Energy	210 MeV/u	260 MeV/u	300 MeV/u
$\epsilon_{\mathrm{TOT}}(\times 10^{-5})$	7.643 ± 0.002	7.916 ± 0.002	7.628 ± 0.001

in a full 4π solid angle according to Equation (4.9). Experimental yields are also compared to the yields obtained from the full Monte Carlo simulation ($\Phi_{\mathrm{p}}^{\mathrm{MC}}$), which have been evaluated according to the following formula:

$$\Phi_{\mathrm{p}}^{\mathrm{MC}} = \frac{1}{4\pi \cdot N_{\mathrm{O}}^{\mathrm{MC}}} \sum_{\mathrm{i}} \left(\frac{N_{\mathrm{p}}^{\mathrm{i}}}{\epsilon_{\mathrm{TOT}}^{\mathrm{i}}} \right)_{\mathrm{MC}} \tag{4.10}$$

where $N_{\mathrm{O}}^{\mathrm{MC}}$ is the total number of simulated primary oxygen ions and $\left(N_{\mathrm{p}}^{\mathrm{i}}/\epsilon_{\mathrm{TOT}}^{\mathrm{i}}\right)_{\mathrm{MC}}$ is the bin per bin correction of the two-dimensional MC distribution of $E_{\mathrm{kin}}^{\mathrm{ToF}}$ as a function of z_{PMMA} for the efficiency matrix previously calculated.

Table 4.9: Computed preliminary values of production yields of secondary protons and comparison with Monte Carlo results. yields are evaluated in the kinetic energy range $10\,\mathrm{MeV} \leq E_{\mathrm{kin}}^{\mathrm{ToF}} \leq 180\,\mathrm{MeV}$, integrated over the full target size and averaged in a full 4π solid angle.

	90°	
Energy (MeV/u)	$\Phi_{\mathrm{p}}\,(\times 10^{-3}\mathrm{sr}^{-1})$	$\Phi_{\mathrm{p}}^{\mathrm{MC}}\,(\times 10^{-3}\mathrm{sr}^{-1})$
210	3.48 ± 0.07	2.41 ± 0.06
260	6.2 ± 0.1	5.9 ± 0.1
300	12.9 ± 0.1	12.3 ± 0.2
	60°	
Energy (MeV/u)	$\Phi_{\mathrm{p}}\,(\times 10^{-3}\mathrm{sr}^{-1})$	$\Phi_{\mathrm{p}}^{\mathrm{MC}}\,(\times 10^{-3}\mathrm{sr}^{-1})$
210	19.7 ± 0.2	21.8 ± 0.2
260	36.2 ± 0.3	46.9 ± 0.3
300	66.3 ± 0.4	85.1 ± 0.7

As expected, proton yields listed in Table 4.9 increase with increasing energy, while an inverse angular dependence is evident. Experimental and Monte Carlo result are not compatible within 3 standard deviations. However, it must be noticed that the uncertainties associated to the experimental production yields have been computed using standard propagation of statistical errors, without taking into account systematic contributions. Several sources of systematic error contribute to the total uncertainty, which need detailed studies in order to be properly evaluated. Due to lack of time, systematic uncertainties have been not included in this work, and those presented in Table 4.9 are preliminary results. The sources of systematics can be of different nature:

- Particle identification: as briefly discussed at the end of Section 4.3.1, some secondary charged particles deposit only a fraction of their energy inside the LYSO, resulting in a smaller QDC value registered due to energy escape. Therefore, some deuterons and tritons can contaminate the distribution of selected protons, inducing errors both in the evaluation of kinetic energy spectra and in the calculation of yields. This systematic uncertainty can be derived from the MC distribution of E_{lyso} as a function of ToF in Figure 4.26, considering the ratio between not-protons and protons in the selected region.

- Geometric parameters: the measurement of the distances between the different components of the experimental set-up is combined with a systematic uncertainty, which plays a major role in the computation of kinetic energy from ToF and in the reconstruction of protons spatial emission distributions.

- Efficiency evaluation method: as described in Section 4.6.1, the method applied for the evaluation of the efficiency is based on the assumption that a linear relation exists between generated and reconstructed variables, and it is biased by the edge effects. Therefore, only particles reconstructed within the range of generation both in z and E_{kin} have been considered for the computation of yields, leading to a systematic underestimation of the number of produced secondary protons.

- Tertiary protons: from the full Monte Carlo simulation it is known that the interaction of the primary beam with the target leads to the production of neutrons, which interact inside the PMMA generating protons. The Monte Carlo simulation for the evaluation of the efficiency does not take into account tertiary protons generated from neutrons, whose transverse distributions is not contained in the 0.4 cm σ of the Gaussian proton source (see Section 4.5). Those protons, therefore, are not included in the evaluation of the efficiency.

4.7 Longitudinal emission distribution

As briefly introduced in Section 4.5, the longitudinal emission distribution of secondary charged particles can be exploited to monitor the Bragg peak position during a hadrontherapy treatment. The main advantage of using secondary charged particles resides in the fact that they can be easily tracked. In the experiment performed at HIT, this has been done by means of the drift chamber, with the reconstruction algorithm described in Section 3.2.1. In order to identify secondary charged particles, reconstructed tracks with $N_{\mathrm{hits}} \geq 8$, of particles that triggered the LYSO, have been selected. In this Section, the analysis performed on the distributions of the reconstructed tracks in the longitudinal plane, for the particles selected, will be presented. A relationship between the Bragg peak position and the secondary charged particle longitudinal emission profile was found already in the experiment performed with carbon ions at LNS (Laboratori Nazionali del Sud, Catania, Italy) [54]. Furthermore, in the experiment performed at GSI (Gesellschaft für Schwerionenforschung, Darmstadt, Germany) [56], a method for the parametrisation of the emission shape was defined, focusing on the falling edge of the charged particles emission distribution. The best parametrisation of the longitudinal emission distribution was identified to be the following function $f(z_{\mathrm{PMMA}})$:

$$f(z_{\mathrm{PMMA}}) = \mathrm{p0} \cdot \frac{1}{1+\exp\left(\dfrac{z_{\mathrm{PMMA}}-\mathrm{p1}}{\mathrm{p2}}\right)} \cdot \frac{1}{1+\exp\left(-\dfrac{z_{\mathrm{PMMA}}-\mathrm{p3}}{\mathrm{p4}}\right)} + \mathrm{p5}. \quad (4.11)$$

This function, which has been called double Fermi-Dirac function, has been used also in the analysis performed in this work, in order to model the longitudinal profiles obtained with oxygen beams at HIT. The parameters p1 and p3 are related to the falling and rising edge of the longitudinal emission distributions shown in Figure 4.25, while p2 and p4 refer to the falling and rising slopes of the function. Finally, the parameter p5 models a possible flat background contribution and p0 is the normalisation parameter. The results of the fit of the longitudinal emission distributions for the different energies and angular configurations are shown in Figure 4.31.

In the experiment performed at GSI, two quantities characterising the longitudinal emission profile were proposed in order to monitor the Bragg peak position: Δ_{40} and δ_{40} (see Figure 4.32). Δ_{40} is the width of the $f(z_{\mathrm{PMMA}})$ function at the 40% of its maximum, being $z^{\mathrm{l}}_{\mathrm{PMMA}}$ and $z^{\mathrm{r}}_{\mathrm{PMMA}}$ the coordinates of the rising and falling edge respectively; δ_{40} is the distance between $z^{\mathrm{l}}_{\mathrm{PMMA}}$ and the intersection point of the tangent to $f(z_{\mathrm{PMMA}} = z^{\mathrm{r}}_{\mathrm{PMMA}})$ with the z_{PMMA}-axis. Starting from the fit parameters reported in Figure 4.31, the quantities Δ_{40}, δ_{40} and $z^{\mathrm{l}}_{\mathrm{PMMA}}$ have been evaluated for each oxygen beam energy and angular configuration: the results are listed in Table 4.10.

As shown in Figure 4.33, a linear dependence of the parameters previously defined

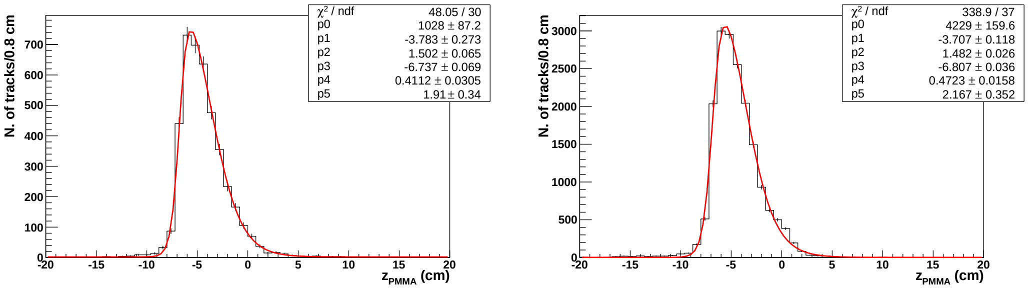

(a) 210 MeV u^{-1}, 90°

(b) 210 MeV u^{-1}, 60°

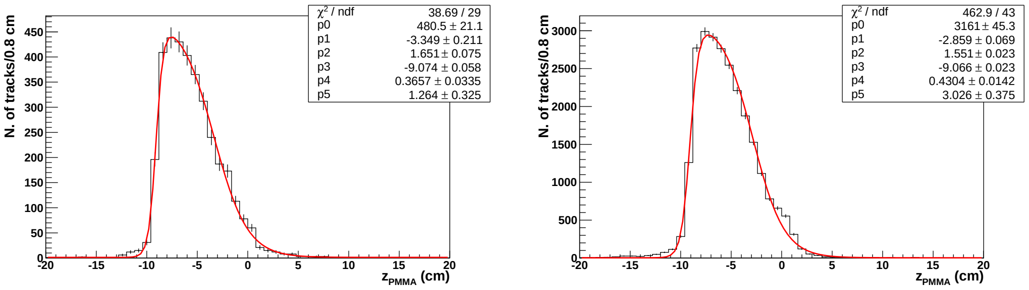

(c) 260 MeV u^{-1}, 90°

(d) 260 MeV u^{-1}, 60°

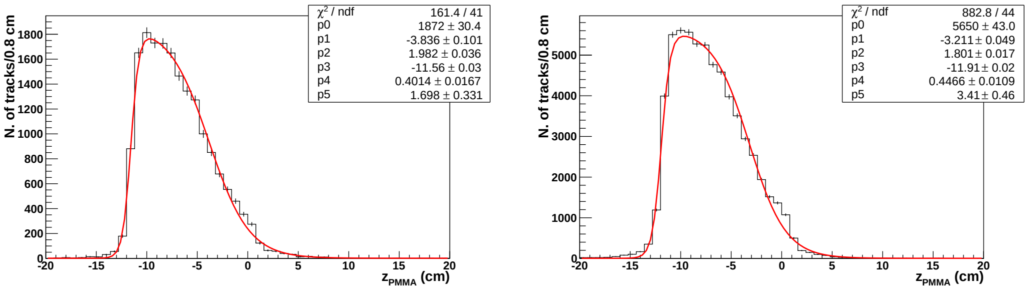

(e) 300 MeV u^{-1}, 90°

(f) 300 MeV u^{-1}, 60°

Figure 4.31: Double Fermi-Dirac fit of the reconstructed longitudinal emission distribution of all the secondary charged particles ($N_{\text{hits}} \geq 8$).

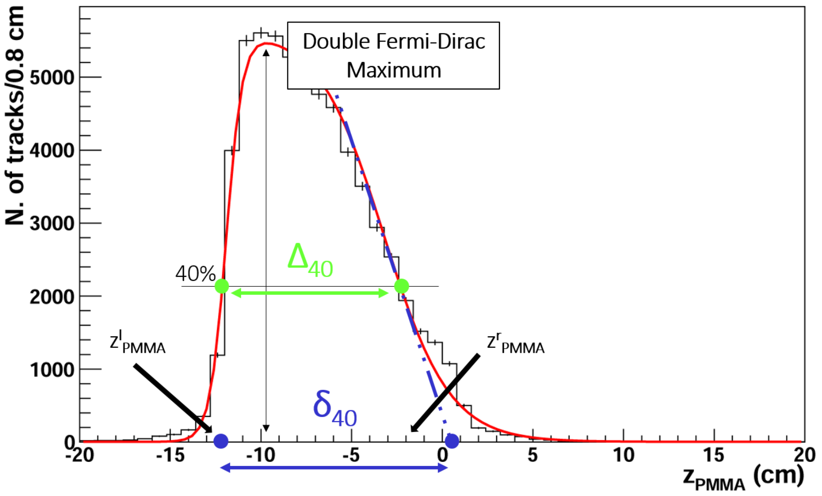

Figure 4.32: Longitudinal emission profile of secondary charged particles reconstructed by the DC. Acquisition with an oxygen beam of 300 MeV u^{-1} in the 90° configuration. The fit function in Equation (4.11) is superimposed, as well as the parameters of interest for the Bragg peak position monitoring.

Table 4.10: Double Fermi-Dirac parameters to be correlated with the Bragg peak position (Δ_{40} and δ_{40}) and the PMMA beam entrance coordinate ($z^{\mathrm{l}}_{\mathrm{PMMA}}$).

	90°		
Energy (MeV/u)	$z^{\mathrm{l}}_{\mathrm{PMMA}}$ (cm)	Δ_{40} (cm)	δ_{40} (cm)
210	-7.04 ± 0.07	4.61 ± 0.20	6.74 ± 0.29
260	-9.26 ± 0.06	6.84 ± 0.21	9.45 ± 0.27
300	-11.8 ± 0.03	8.92 ± 0.10	12.1 ± 0.13
	60°		
Energy (MeV/u)	$z^{\mathrm{l}}_{\mathrm{PMMA}}$ (cm)	Δ_{40} (cm)	δ_{40} (cm)
210	-7.17 ± 0.04	4.79 ± 0.09	6.88 ± 0.12
260	-9.28 ± 0.02	7.23 ± 0.07	9.71 ± 0.09
300	-12.1 ± 0.02	9.73 ± 0.05	12.7 ± 0.06

on the Bragg peak position exists. The obtained relations can be exploited for the real-time monitoring of the beam range in hadrontherapy treatments. The accuracy of the method will generally depend on several elements: multiple scattering suffered by secondary charged particles inside the patient, statistics of the collected sample and fluctuations of the emission process due to nuclear interactions. However, the study of absorption and multiple Coulomb scattering can be performed by means of Monte Carlo simulations. This kind of studies is needed in order to optimise a dedicated monitoring detector and find a valid parametrisation of the relation

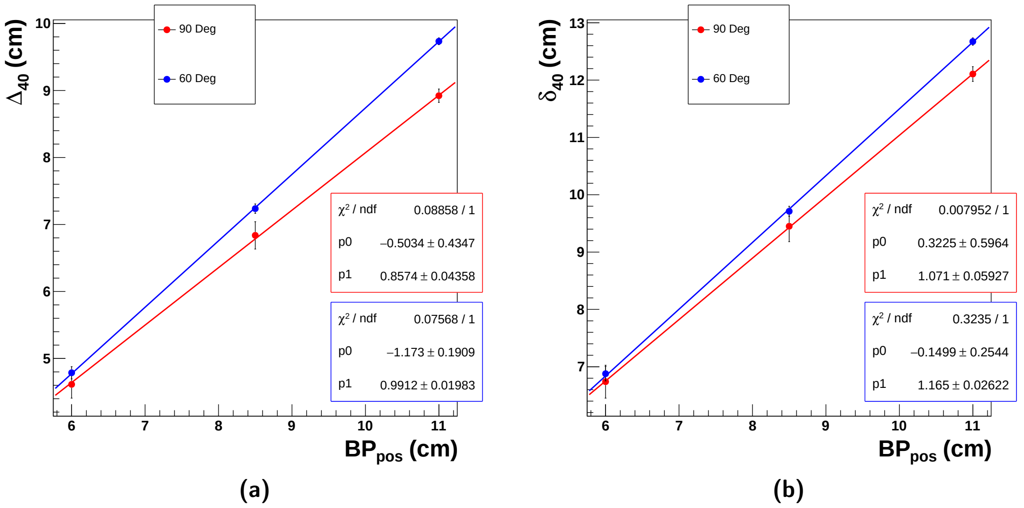

Figure 4.33: (a) Δ_{40} and (b) δ_{40} as a function of the Bragg peak position BP_{pos}, for both the 90° (red) and 60° (blue) configuration. Experimental points are fitted with a linear relation.

between the emission profile parameters (Δ_{40} and δ_{40}) and the Bragg peak position, to be applied in clinical practice.

The contribution of the acquired data sample statistics to the reconstruction resolution of the longitudinal emission distribution parameters was studied during the experiment performed at GSI, comparing the values of Δ_{40} and δ_{40} obtained from small samples of 10^3 reconstructed tracks. With this statistics, a precision in the determination of the longitudinal emission distribution parameters of about 1 mm (90° configuration) and 0.3 mm (60° configuration) was achieved, for 220 MeV u^{-1} ^{12}C ions impinging on the PMMA. The sample dimension of 10^3 was chosen in view of the application of this monitoring technique to a hadrontherapy treatment, considering a single pencil beam reaching the distal part of the tumour with an ion density of the order of 10^8 carbon ions per cm^3. Similar considerations can be done also for the results presented in Table 4.10, starting from the beam parameters listed in Table 4.11, which are necessary to obtain a physical dose of 1 Gy in a cubic $3 \times 3 \times 3\,\text{cm}^3$ Spread Out Bragg Peak (SOBP) beginning at a depth in water of 7 cm, with the HIT synchrotron.

The oxygen ion beam energy of 264.16 MeV u^{-1}, necessary to irradiate the last slice in water at ~ 10 cm of depth, corresponds approximately to the 260 MeV u^{-1} oxygen ion beam energy used to irradiate the PMMA target during the experiment described in this thesis. Making a proportion between the experimental 260 MeV u^{-1} primary oxygen ion beam statistics and the number of primary particles impinging on a slice of $0.2 \times 3 \times 3\,\text{cm}^3$ at a depth of ~ 10 cm in water, a rough evaluation of the expected

Table 4.11: Oxygen ion beam parameters and number of particles necessary to have a physical dose of 1 Gy in a cubic $3 \times 3 \times 3\,\mathrm{cm}^3$ SOBP beginning at a depth in water of 7 cm, with the HIT synchrotron. Syngo TPS calculation (HIT), courtesy of Andrea Mairani.

<table>
<tr><td colspan="2">Beam spacing: $\Delta X, \Delta Y, \Delta Z = 2\,\mathrm{mm}$
15 energy slices from 219.18 to 264.16 $\mathrm{MeV\,u^{-1}}$
Total number of ions: 1.33×10^8</td></tr>
<tr><td>First Slice (at ∼ 7 cm depth)</td><td>Last Slice (at ∼ 10 cm depth)</td></tr>
<tr><td>Energy: 219.81 $\mathrm{MeV\,u^{-1}}$</td><td>Energy: 264.16 $\mathrm{MeV\,u^{-1}}$</td></tr>
<tr><td>$\sigma_{\mathrm{x,y}} = 0.71\,\mathrm{cm}$ (isocentre)</td><td>$\sigma_{\mathrm{x,y}} = 0.67\,\mathrm{cm}$ (isocentre)</td></tr>
<tr><td>4.63×10^6 total particles</td><td>4.70×10^7 total particles</td></tr>
<tr><td>2.06×10^4 particles/beam</td><td>2.09×10^4 particles/beam</td></tr>
</table>

number of secondary charged particles emitted in the last slice of a 1 Gy cubic SOBP can be performed. Thus, an estimate of the precision achievable in the calculation of the Δ_{40} and δ_{40} parameters can be simply obtained, by scaling the parameters errors reported in Table 4.10 with the secondary charged particles statistics. Following this procedure, the precision in the determination of the longitudinal emission distribution parameters (Δ_{40} and δ_{40}) has been evaluated to be ∼ 1 cm in the 90° configuration, and ∼ 3.5 mm in the 60° configuration. Even if these results appear to be worse than those obtained during the GSI experiment, it must be noticed that oxygen ions are expected to be use in clinical practice for hypo-fractionated treatments, which involve physical doses much higher than 1 Gy. In any case, the obtained results suggest that an angle of 60° with respect to the primary beam direction could be the best compromise for the purpose of monitoring ion beams with secondary charged particles during clinical operation.

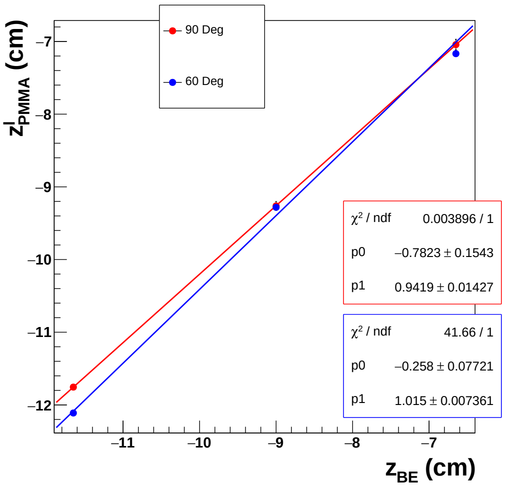

Figure 4.34: z^{1}_{PMMA} as a function of the beam entrance coordinate z_{BE}, for both the 90° (red) and 60° configuration (blue). Experimental point are fit with a linear curve.

Besides the monitoring of the Bragg peak position, longitudinal distribution parameters could be useful also to retrieve informations related to the patient positioning. Indeed, z^1_{PMMA} is correlated to the beam entrance position in the PMMA target z_{BE}, as shown in Figure 4.34. Therefore, by measuring the beam entrance position in the patient, exploiting the emission profile of secondary charged particles, it would be possible to provide a fast feedback on patient mispositioning during the treatment.

One important aspect that must be taken into account, when evaluating the potentialities of secondary charged particles for beam-monitoring purposes, is the deformation of the longitudinal emission distribution shape due to the absorption in the patient tissue. Therefore, a detailed study is currently ongoing, with the aim of defining a method to isolate the absorption effect from the true emission profile as generated by the beam. To this end, FLUKA Monte Carlo simulations calibrated with the data obtained at GSI by *Piersanti et al.* [56] have been developed, from which the attenuation of protons has been obtained as a function of the material crossed. Monte Carlo results, obtained in the case of detection at 90° for a primary ^{12}C ion beam of $220\,\mathrm{MeV\,u^{-1}}$, are shown in Figure 4.35.

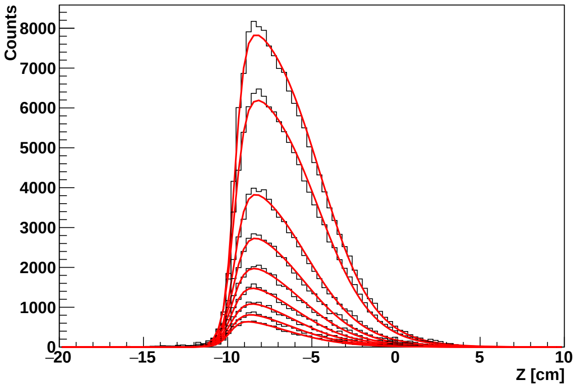

Figure 4.35: Monte Carlo (FLUKA) simulation of the reconstructed longitudinal emission distribution of secondary protons, detected at 90° with respect to the beam direction, and emitted by a 220 MeV ^{12}C ion beam impinging on a cylindrical PMMA target with different radii. Fit with the double Fermi Dirac function defined in Equation (4.11).

Figure 4.35 suggests that look-up tables could be in principle constructed for different beam energies and material thickness, in order to deconvolute the absorption effect from the measured longitudinal emission distributions. To prove this assumption, the distributions shown in Figure 4.35 have been modelled using the double Fermi Dirac function defined in Equation (4.11), while the six distribution parameters have been fitted with simple polynomial functions with respect to the thickness of crossed material. Figure 4.36 shows the results of these fits in the $[2.5, 10]$cm thickness range, where the minimum 2.5 cm corresponds to the PMMA thickness used to collect the data on which the simulation has been trained.

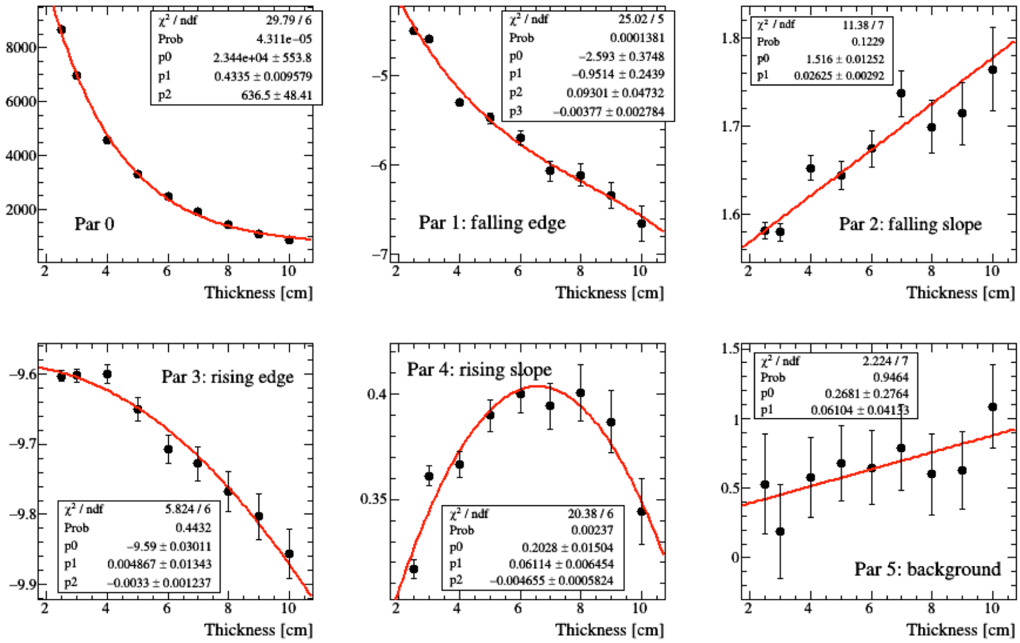

Figure 4.36: Polynomial fit of the double Fermi Dirac parameters with respect to the thickness of crossed material.

Since the double Fermi Dirac parameters depend on the thickness t of crossed material, the emission function in Equation (4.11) can be generalised as a two variables function of z and t:

$$f(z,t) = \mathrm{p}_0(t)\frac{1}{1+\exp\left(\dfrac{z-\mathrm{p}_1(t)}{\mathrm{p}_2(t)}\right)}\frac{1}{1+\exp\left(-\dfrac{z-\mathrm{p}_3(t)}{\mathrm{p}_4(t)}\right)}+\mathrm{p}_5(t). \tag{4.12}$$

where $\mathrm{p_i}(t)$ are the functions depicted in Figure 4.36. Following the previous considerations, a weighting function, independent on the absorption effect, can be defined as:

$$w(z,t) = \frac{f(z,t_0)}{f(z,t)} \tag{4.13}$$

where t_0 is the minimum reference thickness corresponding to 2.5 cm.
This procedure has been applied to the system shown in Figure 4.37, where a ^{12}C ion beam propagates in a PMMA sphere of 10 cm radius (density $\rho = 1.2\,\mathrm{g\,cm^{-3}}$), containing a smaller sphere of density $\rho_o = 0.6\,\mathrm{g\,cm^{-3}}$ with radius equal to 3 cm. The simulated detector, placed at a distance of 40 cm from the sphere center, is the INSIDE Dose Profiler described at the end of Chapter 2.

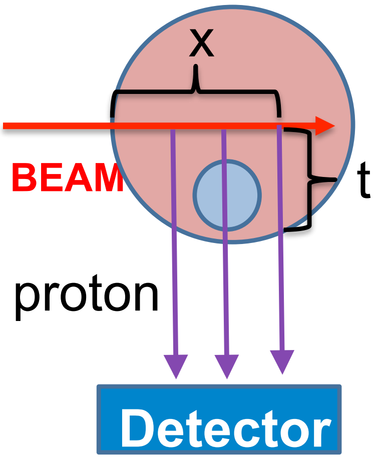

Figure 4.37: Simulation set-up for a proof of concept of the absorption effect deconvolution method.

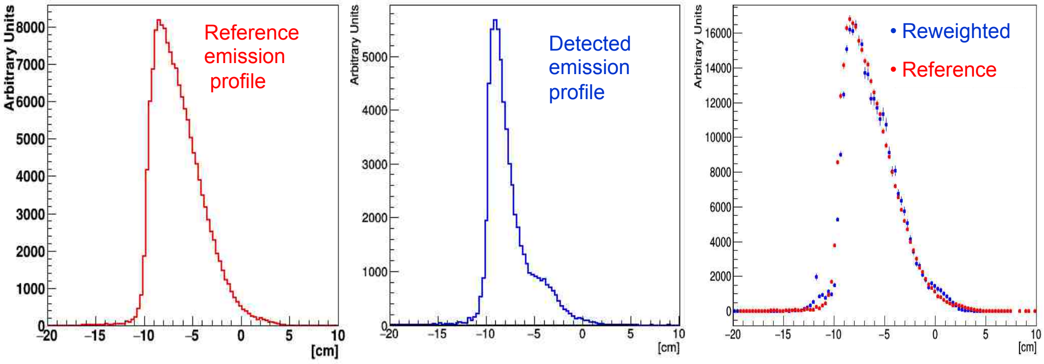

Figure 4.38: Left: MC longitudinal emission distribution of secondary charged particles as produced by the beam. Middle: MC longitudinal emission distribution as reconstructed by the detector. Right: the reconstructed longitudinal emission distribution corrected for the weighting factor (blue) is compared to the reference emission profile (red). Simulation performed with the set-up described in Figure 4.37.

Figure 4.38 reports the results obtained for the reconstruction of the longitudinal emission distributions, corrected for the weighting factor in Equation (4.13). In the left panel, the MC longitudinal emission distribution as produced by the beam is depicted, while the emitted secondary charged particles profile as reconstructed by the detector is shown in the central panel. From this last figure, the distortion in the emission shape, due to the material absorption effect, and its possible outcomes on the correct evaluation of the Bragg peak position are evident. The results of the deconvolution procedure are shown in the right panel, where the re-weighted reconstructed longitudinal emission profile is superimposed to the generated one. This results indicate the possibility of extracting the original secondary charged particles longitudinal emission distributions, if a detailed map of the material crossed by the detected particles is known. However, it must be remarked that this knowledge would imply the use of an improved software system, capable to associate to each reconstructed track the correspondent composition and thickness of material crossed, exploiting the CT informations.

Conclusions

Hadrontherapy is an emerging technique in cancer treatment, which is proving to be a valid alternative to conventional photon radiotherapy for an increasing number of tumours. By the end of 2014, more than 137 000 patients had been treated with hadrontherapy, carried out mostly with protons (86%) and carbon ions (11%), and a continuous increase in the number of patients treated with hadrontherapy was registered in the past decade. Nowadays, the possibility of extending the therapeutic spectrum of clinical ions appears to be the new challenge of hadrontherapy, as it would lead to personalised and radiation-quality optimised cancer treatments. In this frame, oxygen ions play a major role, since they are the perfect candidates for targeting tumour hypoxia. The oxygenation level of cancer cells is known to be a critical limiting factor for conventional radiation therapy, as hypoxic tumours appear to be radioresistant to low LET radiation. On the other side, the cell killing capability of high-LET radiations, such as oxygen ions, is less dependent on the oxygenation status. This suggests that they might be used, in combination with photons and lower LET ions, for the irradiation of restricted volumes were hypoxic cells are present. In view of the possibility of implementing radiation-quality optimised treatments in clinics, experimental data on new ions are needed, in order to consistently describe their physical and biological properties to a high enough level of accuracy.

Apart from the higher biological effectiveness of light ions, the main physical advantage of using charged hadrons in radiation therapy is based on their finite range in tissues, placed at a given depth depending on the primary beam energy and target composition. However, in clinical practice many factors contribute to range uncertainties, posing serious issues and constraints both on the beam delivery and quality assurance. While the primary beam parameters can be easily verified, the final dose distribution within the patient is much harder to quantify, calling for precise dose monitoring techniques capable of giving a fast and effective treatment quality feedback. All the existing range-monitoring techniques are based on the detection of secondary particles emitted after the primary ion beam interaction with the target: photons from e^+e^- annihilation, prompt gammas and charged particles. The latest, in particular, appear to be very promising for range monitoring purposes, since they can be easily tracked and their longitudinal emission distribution is correlated with Bragg peak position inside the target. From a geometrical point of view, the precision in the range reconstruction depends on the detection angle (θ) with respect to the beam axis, and reaches its maximum when the detector is placed at $\theta = 90°$. On the other side, the yield of secondary charged particles decreases with increasing θ, limiting the statistics and therefore the achievable resolution.

This thesis documents the analysis performed on secondary charged particles produced in the interaction of oxygen beams at different energies with a PMMA target, in view of the future application of this monitoring technique in a clinical environment. The work presented in this thesis aims at giving a value for the obtainable secondary charged particles production yields at large detection angles (90° and 60°), as well as at evaluating the precision achievable with this monitoring approach. In spite of the large detection angles, results show that the number of protons and other fragments is high enough to allow the reconstruction of the secondary charged particles emission profiles. Furthermore, a high percentage of protons ($\sim 60\%$) is emitted with kinetic energy higher than 40 MeV after 2.5 cm of PMMA, meaning that they could still traverse some centimetres of tissue without being absorbed. Considering for example a tumour placed in the middle of the head, the thickness of material to be crossed might be of the order of $\sim 7\,\mathrm{cm}$, which means that secondary protons should be emitted with energies greater than $\approx 100\,\mathrm{MeV}$. Following these considerations, the results obtained for kinetic energy spectra confirm the possibility of detecting secondary charged particles in clinical practice, with a high enough statistics for beam-monitoring. The preliminary results obtained for the proton production yields, are in agreement with the previous considerations. However, further studies are required in order to assess the systematic uncertainties associated with these measurements.

A clear correlation between the charged particles emission profile and the Bragg peak position has been observed. Therefore, two parameters, Δ_{40} and δ_{40}, characterising the charged particle longitudinal emission distribution have been proposed in order to monitor the maximum of the dose released. A linear relation between such parameters and the position of the Bragg peak in the energy range considered exists. The precision achievable in the reconstruction of these parameters depends heavily on the detected secondary charged particles statistics. However, results suggest that a configuration at an angle lower than 90°, down to about 60°, should be preferred in view of the application of this monitoring technique into clinics. Finally, the existence of a linear relation between the rising edge of the charged fragments emission distribution and the beam entrance position inside the target has been proven, which might be used as a reference variable for patient positioning verifications.

The results obtained from the measurement described in this thesis fully support the feasibility of a novel real-time monitoring technique based on the detection of secondary charged particles. With this technique, an accuracy of about $1-2\,\mathrm{mm}$ in the determination of the distal part of the hadrontherapy treatment is expected to be achieved in the next future. At present, dedicated detectors are under development, in order to test the application of this beam-monitoring approach in the clinical operation.

Riassunto

La radioterapia oncologica è una disciplina clinica che sfrutta le radiazioni ionizzanti, quali fotoni, elettroni, protoni, ioni leggeri e neutroni, per il trattamento di patologie neoplastiche. Secondo le statistiche dell'Organizzazione Mondiale della Sanità (WHO - World Health Organization) [1], i tumori rappresentano la principale causa di morte nei paesi ad alto reddito, secondi solo alle malattie del sistema cardiocircolatorio. D'altra parte, i dati epidemiologici divulgati dall'Agenzia Internazionale per la Ricerca sul Cancro (IARC - International Agency for Research on Cancer) [2] evidenziano una costante riduzione del tasso di mortalità da tumori negli ultimi anni, dato che riflette il progressivo avanzamento nella diagnosi e cura di molte patologie oncologiche. Tra le metodiche terapeutiche disponibili per la cura dei tumori, la radioterapia è sicuramente la tecnica che ha conosciuto i maggiori sviluppi e le più radicali innovazioni tecnologiche, grazie anche allo sviluppo di sistemi di definizione dell'area di trattamento e di rilascio della radiazione sempre più precisi. Ad oggi, circa i 2/3 dei pazienti cui è stato diagnosticato un tumore ricevono trattamenti radioterapici con fini sia curativi che palliativi [3], spesso in associazione con altre tecniche e per lo più condotti mediante l'uso di fotoni o elettroni. Tuttavia, la rapida evoluzione tecnologica sperimentata dalla radioterapia oncologica negli ultimi vent'anni ha portato anche alla progressiva affermazione di una tecnica alternativa, basata sull'uso di adroni carichi: l'adroterapia.

L'adroterapia è una tecnica emergente nel campo della terapia oncologica, che sfrutta adroni carichi accelerati, quali protoni e ioni leggeri, per il trattamento di alcuni tumori solidi. In particolare, l'adroterapia si pone come indicazione ideale per quei tumori in cui la radioterapia convenzionale non dà vantaggi significativi: i tumori radio-resistenti e quelli localizzati vicino ad organi a rischio. Con l'adroterapia, infatti, è possibile trattare l'area tumorale con precisione millimetrica, sfruttando il meccanismo di deposito dell'energia in profondità caratteristico dell'interazione di protoni ed altri ioni con la materia. Gli adroni carichi presentano la caratteristica di rilasciare gran parte della loro energia alla fine del loro percorso nei tessuti, in corrispondenza di quello che viene chiamato il picco di Bragg. Poiché la posizione di questo picco dipende dall'energia iniziale della particella incidente e dalla com-

posizione dei tessuti attraversati, è possibile posizionare il massimo del deposito di energia in corrispondenza del tumore, minimizzando al contempo eventuali danni a tessuti sani ed organi a rischio circostanti.

Negli ultimi dieci anni, il crescente interesse dimostrato dalla comunità medica, nei confronti degli eccellenti risultati clinici ottenuti con l'adroterapia, ha portato alla costruzione e installazione di acceleratori dedicati in numerosi centri ospedalieri di tutto il mondo. Tra le particelle cariche più usate, spiccano sicuramente i protoni, seguiti in minor misura dagli ioni carbonio. Recentemente, tuttavia, una fiorente discussione scientifica è nata riguardo alla possibilità di estendere lo spettro degli ioni utilizzabili a fini terapeutici, con l'obiettivo di ottimizzare le potenzialità cliniche dell'adroterapia. Rispetto ai protoni, infatti, gli ioni leggeri ($Z \leq 8$) sono caratterizzati da una maggiore efficacia radio-biologica, strettamente legata alla maggiore densità di ionizzazioni indotte a mano a mano che vengono frenati nella materia. Essi, dunque, sono più efficaci nell'indurre lesioni dirette al DNA delle cellule tumorali, aumentando marcatamente l'efficacia della radiazione nel provocare la morte cellulare. D'altra parte, rispetto ai protoni, gli ioni leggeri presentano anche uno svantaggio: all'aumentare della massa della particella incidente, aumenta il grado di frammentazione all'interno del paziente. Le collisioni dello ione proiettile con i nuclei del bersaglio, infatti, possono portare alla disgregazione del primo, con la produzione di particelle molto energetiche e di massa inferiore. Tipicamente, queste particelle viaggiano per un tratto più lungo nella materia rispetto allo ione che le ha generate, inducendo un deposito di dose, cioè di energia per unità di massa, anche oltre il picco di Bragg. Per trarre vantaggio dalla maggiore efficacia biologica degli ioni leggeri senza incorrere nei rischi legati ad un deposito di dose al di fuori dell'area tumorale, è stata avanzata la proposta di utilizzare questi ioni in trattamenti combinati con altri tipi di radiazione. É questo, per esempio, il caso degli ioni di ossigeno, che a livello sperimentale si sono dimostrati particolarmente efficaci nella cura di tumori poco ossigenati e resistenti alla radioterapia convenzionale. In questo contesto, gli ioni di ossigeno potrebbero essere utilizzati in trattamenti combinati con fotoni, protoni o altri ioni, al fine di irraggiare solo quelle zone del tumore caratterizzate da carenza di ossigeno. Numerosi studi devono essere tuttavia realizzati, affinché l'introduzione di trattamenti ottimizzati con diversi tipi di radiazione divengano applicabili nella pratica clinica. In particolare, vari esperimenti dovrebbero essere condotti sui nuovi ioni di interesse terapeutico, al fine di raccogliere dati fisici e biologici sufficienti, per poterli testare sui pazienti. L'esperimento di cui questa tesi fa parte, risponde parzialmente a questa esigenza.

La grandissima selettività e conformità al volume tumorale raggiungibili con i trattamenti adroterapici, richiedono altissimi standard di precisione nel posizionamento del paziente e nel sistema di rilascio della dose. Mentre i parametri del fascio di ioni primari possono essere facilmente verificati esternamente al paziente durante il trattamento, la distribuzione finale di dose all'interno del paziente risulta molto più difficile da quantificare e monitorare. Poiché un piccolo errore nel posizionamento del paziente o nella determinazione della posizione del picco di Bragg può inficiare la qualità del trattamento e indurre severi danni a tessuti e organi sani, appare evidente l'importanza di introdurre sistemi di monitoraggio real-time nelle sale di trattamento. Ad oggi, le tecniche proposte per monitorare la posizione del picco di Bragg durante il trattamento si basano sulla rivelazione di diversi tipi di particelle secondarie. Queste particelle, derivanti dalle interazioni nucleari del fascio primario con i nuclei del bersaglio, possono essere di diversi tipi: fotoni prodotti dall'annichilazione e^+e^- a seguito di decadimento β^+; fotoni veloci da diseccitazione nucleare; particelle cariche, per lo più protoni e altri isotopi dell'idrogeno, prodotte dalla frammentazione sia del nucleo incidente che del nucleo bersaglio. Queste ultime, in particolare, sono le particelle di interesse per questo lavoro di tesi, che si pone l'obiettivo di studiare l'emissione di frammenti carichi da parte di fasci di ossigeno, incidenti su un bersaglio di polimetilmetacrilato (PMMA) tessuto equivalente.

L'esperimento in cui si inserisce questo progetto di tesi è stato condotto presso la sala sperimentale del "Heidelberg Ion Therapy Center" (HIT), in Germania, con l'obiettivo di studiare le diverse tecniche di monitoraggio di un trattamento adroterapico e, contemporaneamente, valutare le caratteristiche di diversi tipi di ioni. A questo proposito, si è irraggiato un fantoccio di PMMA con fasci di elio, carbonio e ossigeno a diverse energie, con l'intento di rivelare tutte le particelle secondarie emesse a seguito dell'interazione degli ioni primari con il bersaglio. Questo lavoro di tesi, in particolare, è stato volto all'analisi delle particelle cariche secondarie emesse da fasci di ossigeno con le seguenti energie: $210\,\mathrm{MeV\,u^{-1}}$, $260\,\mathrm{MeV\,u^{-1}}$ e $300\,\mathrm{MeV\,u^{-1}}$.

Tra le diverse tecniche di monitoraggio, la misura di frammenti carichi presenta numerosi vantaggi, legati alla facilità con cui queste particelle possono essere rivelate e tracciate. Il profilo di emissione longitudinale di queste particelle, infatti, è direttamente collegato alla deposizione di energia da parte del fascio primario nel bersaglio di PMMA, e dunque alla posizione del picco di Bragg. Da un punto di vista geometrico, la precisione raggiungibile nella ricostruzione di questi profili dipende dalla posizione angolare di rivelazione (θ) rispetto alla direzione del fascio primario, e raggiunge il suo massimo in corrispondenza di $\theta = 90°$. D'altra parte, il numero di particelle cariche secondarie emesse diminuisce all'aumentare di θ, riducendo la statistica e dunque la risoluzione ottenibile nella determinazione della posizione del picco di Bragg. In vista di una possibile applicazione di questa tecnica di monitoraggio in ambiente clinico, nell'esperimento condotto a HIT le particelle cariche secondarie sono state rivelate in due diverse configurazioni angolari: a 90° e 60° rispetto alla direzione del fascio di ioni. Per la misura di queste particelle si è utilizzato un sistema di rivelatori composto da due elementi fondamentali: una camera a deriva per tracciare le particelle cariche, seguita da un cristallo di LYSO ($Lu_{1.8}Y_{0.2}SiO_5(Ce)$ - ortosilicato di lutezio e ittrio drogato con cesio) per fermarle e misurarne l'energia. L'obiettivo dell'analisi condotta in questo lavoro di tesi è stato sia quello di valutare il flusso di particelle cariche secondarie prodotte, sia quello di determinare la precisione ottenibile nella ricostruzione dei profili di emissione longitudinali, correlati con la posizione del picco di Bragg.

Nonostante la rivelazione a grandi angoli, dall'analisi svolta in questa tesi è emerso come il numero di frammenti carichi misurato sia sufficiente per permettere la ricostruzione dei profili di emissione longitudinali. Inoltre, come si è evidenziato dallo studio delle distribuzioni di energia cinetica dei protoni secondari, gran parte di queste particelle sono state emesse con energia sufficiente per attraversare diversi centimetri di tessuto senza essere assorbite. I risultati così ottenuti confermano la possibilità di rivelare particelle cariche secondarie anche durante la pratica clinica. I valori preliminari ottenuti per il flusso di protoni in produzione si sono mostrati in accordo con le precedenti considerazioni; ulteriori studi, tuttavia, devono essere realizzati per determinare le incertezze sistematiche associate a queste misure.
Una chiara correlazione è emersa tra il profilo di emissione longitudinale delle particelle cariche secondarie e la posizione del picco di Bragg. Analizzando la forma del profilo di emissione longitudinale, è stato possibile estrarre due parametri, Δ_{40} e δ_{40}, da poter confrontare con la posizione del picco di Bragg al variare dell'energia del fascio primario. Dal confronto di queste quantità, è emersa una chiara relazione lineare nel range di energia considerato. Poiché la precisione raggiungibile nella determinazione dei parametri Δ_{40} e δ_{40} dipende fortemente dal numero di particelle cariche secondarie misurato, i risultati migliori si sono ottenuti con i rivelatori posizionati a 60° rispetto alla direzione del fascio.

I risultati ottenuti in questo lavoro di tesi confermano la possibilità di sfruttare l'emissione di particelle cariche secondarie per monitorare la posizione del picco di Bragg durante il trattamento adroterapico. É emerso, inoltre, come una rivelazione in un intervallo angolare tra i 90° e i 60° rispetto al fascio primario, sia da preferirsi in vista di un'applicazione di questa tecnica nella pratica clinica. Rivelatori ad hoc, da testare in applicazione clinica per questo tipo di approccio al monitoraggio del fascio, sono attualmente in fase di sviluppo, con i quali si prevede di arrivare ad una risoluzione di $1-2\,\mathrm{mm}$ nella localizzazione della parte distale del trattamento.

Bibliography

[1] B. W. Stewart & C. P. Wild. *World Cancer Report 2014*. IARC (International Agency for Research on Cancer) Nonserial Publication, 2014.

[2] GLOBOCAN 2012: Estimated Cancer Incidence, Mortality and Prevalence Worldwide in 2012. URL `http://globocan.iarc.fr/Pages/fact_sheets_cancer.aspx`

[3] Statistics about Radiation Therapy.
URL `http://www.rtanswers.org/statistics/aboutradiationtherapy/`

[4] RadiologyInfo.org. *Intensity-Modulated Radiation Therapy (IMRT)*. Radiological Society of North America, Inc., 2016.
URL `http://www.radiologyinfo.org/en/pdf/imrt.pdf`

[5] R. Orecchia et al. *Particle Beam Therapy (Hadrontherapy): Basis for Interest and Clinical Experience.* European Journal of Cancer, 34(4): 459-468, 1998.

[6] Robert R. Wilson. *Radiological Use of Fast Protons.* Radiology, 47(2): 487-491, 1946.

[7] NuPECC Report. *Nuclear Physics for Medicine: Hadrontherapy.* 2014.

[8] German Cancer Reserch Center site: Biological Models.
URL `https://www.dkfz.de/en/medphys/appl_med_rad_physics/Biological_models.html`

[9] Emmanouil Fokas et al. *Ion beam radiobiology and cancer: Time to update ourselves.* Biochimica et Biophysica Acta, 1796: 216-229, 2009.

[10] C. Leroy & P. Rancoita. *Principles of Radiation Interaction in Matter and Detection*, Chapter 2. Singapore: World Scientific Publishing Co. Pte. Ltd., 2004.

[11] G. F. Knoll. *Radiation Detection and Measurement*, Chapter 2. New York: John Wiley & Sons, Inc., 2000.

[12] W. R. Leo. *Techniques for Nuclear and Particle Physics Experiments: A How-To Approach*, Chapter 2. New York, Berlin, Heidelberg: Springer-Verlag, 1994.

[13] J. Jackson. *Classical Electrodynamics*, Chapter 13. New York: John Wiley & Sons, Inc., 1999

[14] H. Bethe et al. *Passage of radiations through matter.* Experimental Nuclear Physics, Vol. 1, 1953.

[15] H. W. Barkas. *Nuclear Research Emulsions.* New York: Academic Press, Vol. 1, 1973.

[16] M. Testa. *Physical measurements for ion range verification in charged particle therapy.* PhD thesis, Université Claude Bernard - Lyon 1, 2010.

[17] J. F. Ziegler. *SRIM-2003.* Nuclear Instruments and Methods in Physics Research Section B: Beam Interactions with Materials and Atoms, 219: 1027-1036, 2004.

[18] O. Jäkel. *Radiotherapy with protons and ion beams.* AIP Conference Proceedings, 1231(1): 3-40, 2010.

[19] P. V. Vavilov. *Ionization losses of high energy heavy particles.* Soviet Physics JETP, 5(4): 749-751, 1957.

[20] N. Bohr. *On the Theory of the Decrease of Velocity of Moving Electrified Particles on passing through Matter.* Philosophical Magazine 25: 10, 1913.

[21] Do In Seb. *Range Straggling of Charged Particles in Various Substances.* Soviet Physics JETP, 18(2): 540-541, 1964.

[22] D. Schardt et al. *Heavy-ion tumor therapy: Physical and radiobiological benefits.* Reviews of Modern Physics, 82: 383-425, 2010.

[23] B. B. Rossi. *High-energy Particles.* New York: Prentice-Hall physics series, 1952.

[24] V. L. Highland. *Some practical remarks on multiple scattering.* Nuclear Instruments and Methods, 129(2): 497-499, 1975.

[25] A. C. Kraan. *Range verification methods in particle therapy: underlying physics and Monte Carlo modelling.* Frontiers in Oncology, 5(150), 2015.

[26] A. Ferrari & P. R. Sala. *The Physics of High Energy Reactions.* Proceedings the Workshop on Nuclear Reaction Data and Nuclear Reactors Physics, Design and Safety, ICTP-Trieste, 1996.

[27] R. Serber. *Nuclear Reactions at High Energies.* Physical Review, 72(11): 1114-1115, 1947.

[28] J. D. Bowman et al. *Abrasion and Ablation of heavy ions* (unpublished). LBL Report No. LBL-2908, University of California, 1973.

[29] K. Gunzert-Marx et al. *Secondary beam fragments produced by* 200 MeV u^{-1} ^{12}C *ions in water and their dose contributions in carbon ion radiotherapy.* New Journal of Physics, 10(7): 075003, 2008.

[30] M. Joiner & A. Van der Kogel. *Basic Clinical Radiobiology.* Chapter 1-2. London: Hodder Arnold, 2009.

[31] U. Amaldi et al. *Radiotherapy with beams of carbon ions.* Reports on Progress in Physics, 68(8): 1861, 2005.

[32] E. J. Hall & A. J. Giaccia *Radiobiology for the Radiologist.* Chapter 3. Philadelphia: Lippincott Williams & Wilkins, 2006.

[33] D. Mihailescu et al. *Biophysical models in hadrontherapy.* Journal of Advanced Research in Physics, 3(1): 011210, 2012.

[34] T. Elsässer et al. *Quantification of the relative biological effectiveness for ion beam radiotherapy: direct experimental comparison of proton and carbon ion beams and a novel approach for treatment planning.* International Journal of Radiation Oncology· Biology · Physics, 78(4): 1177-1183, 2010.

[35] F. Tommasino et al. *New Ions for Therapy.* International Journal of Particle Therapy, 2015.

[36] P. Crespo. *Optimization of In-Beam Positron Emission Tomography for Monitoring Heavy Ion Tumor Therapy.* PhD thesis, Technische Universitä Darmstadt, 2005.

[37] M. Jermann. *Particle Therapy Statistics in 2014.* International Journal of Particle Therapy, 2(1): 50-54, 2015.

[38] N.Bassler et al. *LET-painting increases tumour control probability in hypoxic tumours.* Acta Oncologica, 53(1): 25-32, 2013.

[39] Particle Therapy Facilities in Operation.
URL `http://www.ptcog.ch/index.php/facilities-in-operation`.

[40] Treatable tumours - Hatrontherapy Indications.
URL `http://fondazionecnao.it/en/what-do-we-do/treatable-tumors`.

[41] A. Knopf et al. *In vivo proton range verification: a review.* Physics in Medicine and Biology, 58: R131-R160, 2013.

[42] R. Faccini et al. *Dose Monitoring in Particle Therapy.* Modern Physics Letters A 30: 1540023, 2015.

[43] H. Paganetti. *Range uncertainties in proton therapy and the role of Monte Carlo simulations.* Physics in Medicine and Biology, 57(11): R99-R117, 2012.

[44] B. Schaffner et al. *The precision of proton range calculations in proton radiotherapy treatment planning: experimental verification of the relation between CT-HU and proton stopping power.* Physics in Medicine and Biology, 43(6): 1579-1592, 1998.

[45] R. A. Pownser & E. R. Pownser. *Essential Nuclear Medicine Physics.* Chapter 8. Malden, Oxford, Victoria: Blackwell Publishing Ltd, 2006.

[46] W. Enghardt et al. *Dose quantification from in-beam positron emission tomography.* Radiotherapy and Oncology, 73(2): S96-S98, 2004.

[47] A. C. Kraan et al. *Online monitoring for proton therapy: A real-time procedure using a planar PET system.* Nuclear Instruments and Methods in Physics Research A, 786: 120-126, 2015.

[48] C. H. Min et al. *Prompt gamma measurements for locating the dose fallof region in the proton therapy.* Applied Physics Letters, 89(18): 183517, 2006.

[49] E. Testa et al. *Monitoring the Bragg peak location of* $73\,\mathrm{MeV}/u$ *carbon ion beams by means of prompt gamma-ray measurements.* Applied Physics Letter, 93(9): 093506, 2008.

[50] C. Golnik et al. *Range assessment in particle therapy based on prompt* $\gamma-ray$ *timing measurements.* Physics in Medicine and Biology, 59: 5399-5422, 2014.

[51] C. Richter et al. *First clinical application of a prompt gamma based in vivo proton range verification system.* Radiotherapy and Oncology, 2016.

[52] U. Amaldi et al. *Advanced quality assurance for CNAO.* Nuclear Instruments and Methods in Physics Research A, 617: 248-249, 2010.

[53] P. Henriquet et al. *Interaction vertex imaging (IVI) for carbon ion therapy monitoring: a feasibility study.* Physics in Medicine and Biology, 57: 4655-4669, 2012.

[54] C. Agodi et al. *Charged particle's flux measurement from PMMA irradiated by* 80 MeV/u *carbon ion beam.* Physics in Medicine and Biology, 57(18): 5667, 2012.

[55] C. Agodi et al. *Corrigendum: Charged particle's flux measurement from PMMA irradiated by* 80 MeV/u *carbon ion beam.* Physics in Medicine and Biology, 59(23): 7563, 2014.

[56] L. Piersanti et al. *Measurement of charged particle's yields from PMMA irradiated by a* 220 MeV/u ^{12}C *beam.* Physics in Medicine and Biology, 59(7): 1857, 2014.

[57] E. Fiorina et al. *An integrated system for the online monitoring of particle therapy treatment accuracy.* ACTA PHYSICA POLONICA A127: I465, 2015.

[58] UniversitätsKlinikum Heidelber: Accelerator facility. URL `https://www.klinikum.uni-heidelberg.de/Accelerator-facility.117968.0.html?&L=1`.

[59] Information Brochure HIT, Heidelberg University Hospital. English version 2012. URL `https://www.klinikum.uni-heidelberg.de/fileadmin/hit/dokumente/121019KV_SS_HITImage_engl_web_ID17763.pdf`

[60] K. Parodi et al. *Monte Carlo simulations to support start-up and treatment planning of scanned proton and carbon ion therapy at a synchrotron-based facility.* Physics in Medicine and Biology, 57(12): 3759, 2012.

[61] S. E. Combs et al. *Particle therapy at the Heidelberg Ion Therapy Center (HIT) - Integrated research-driven university-hospital-based radiation oncology service in Heidelberg, Germany.* Radiotherapy and Oncology, 95: 41-44, 2010.

[62] Th. Haberer et al. *The Heidelberg Ion Therapy Center.* Radiotherapy and Oncology, 73, Supplement 2(0): S186-S190, 2004.

[63] C. Agodi et al. *Precise measurement of prompt photon emission from* 80 MeV/u *carbon ion beam irradiation.* Journal of Instrumentation 7(3): P03001, 2012.

[64] I. Mattei. *A novel* on-line *dose monitoring technique tailored for Particle Therapy.* PhD thesis, Università di Roma Tre, 2015.

[65] W. R. Leo. *Techniques for Nuclear and Particle Physics Experiments: A How-To Approach*, Chapter 6. New York, Berlin, Heidelberg: Springer-Verlag, 1994.

[66] Z. Abou-Haidar et al. *Performance of upstream interaction region detectors for the FIRST experiment at GSI.* Journal of Instrumentation, 7: P02006, 2012.

[67] G. F. Knoll. *Radiation Detection and Measurement*, Chapter 8. New York: John Wiley & Sons, Inc., 2000.

[68] E. Testa et al. *Dose profile monitoring with carbon ions by means of prompt-gamma measurements.* Nuclear Instruments and Methods in Physics Research Section B: Beam Interactions with Materials and Atoms, 267(6): 993-996, 2009.

[69] A. Ferrari et al. *Fluka: a multi particle transport code.* Tech. Rep. CERN-2005-10, INFN/TC05/11, 2005.

[70] G. Battistoni et al. *Overview of the Fluka code.* Annals of Nuclear Energy, 82: 10-18, 2015.

[71] F. Bellini et al. *Extended calibration range for prompt photon emission in ion beam irradiation.* Nuclear Instruments and Methods in Physics Research, A 745C: 114-118, 2014.

[72] M. Cavinato et al. *Boltzmann master equation theory of angular distributions in heavy-ion reactions.* Nuclear Physics A 643: 15-29, 1998.

[73] M. Cavinato et al. *Monte Carlo calculations of havy ion cross-sections based on the Boltzmann Master equation theory.* Nuclear Physics A 679: 753-764, 2001.

[74] H. Sorge et al. *Relativistic quantum molecular dynamics approach to nuclear collisions at ultrarelativistic energies.* Nuclear Physics A 498: 567-576, 1989.

[75] H. Sorge et al. *Poincaré invariant hamiltonian dynamics: modelling multi-hadronic interactions in a phase space approach.* Annals of Physics, 192(2): 266-306, 1989.

[76] *FLUKA Beginner's Course: FLUKA Manual and Basic Input.* 17th Fluka Course, Munich, Germany, 9-13 November 2015.

[77] T. Ullrich et al. *Treatment of Errors in Efficiency Calculations.* Brookhaven National Laboratory, 2008.

Ringraziamenti

Desidero ringraziare il mio relatore, Professor Giuseppe Battistoni, per avermi dato la possibilità di lavorare con lui e con il suo gruppo a Milano. Gli sono immensamente grata per la fiducia dimostratami, senza la quale non mi sarei mai potuta imbarcare nell'avventura di questa tesi. Lo ringrazio per la sua accoglienza e per il modo in cui mi ha fatta sentire a mio agio. La sua guida e l'attenzione con cui mi ha seguita in ogni passaggio di questo lavoro sono state un prezioso supporto, affinché io potessi raggiungere questo importante obiettivo.

Un sentito grazie va alla Dottoressa Ilaria Mattei, correlatrice di questa tesi. L'entusiasmo e la passione con cui affronta il lavoro e la vita sono travolgenti. La ringrazio per la dedizione con cui mi ha seguito e per la pazienza con cui mi è stata accanto. La sua vicinanza è stata uno stimolo a migliorare e ad affrontare senza paura le difficoltà. Infine la ringrazio per il modo in cui mi è stata amica, per l'affetto con cui mi chiama bimba e perché grazie a lei, nonostante l'ambiente nuovo, non mi sono sentita sola.

Un grazie di cuore a Silvia, Serena e Mauro, che mi hanno accompagnato nella mia parentesi milanese. La loro amicizia e il loro continuo incoraggiamento e sostegno mi hanno fatto sentire parte integrante del gruppo. Li ringrazio per la loro presenza e per tutti i momenti condivisi insieme: hanno contribuito a rendere lo svolgimento della tesi una piacevole esperienza.

Ringrazio inoltre il Professor Vincenzo Patera e tutto il gruppo di Roma. Nonostante il poco tempo trascorso assieme, la loro vivacità è stata per me di grande stimolo. Li ringrazio per l'interesse con cui hanno seguito lo svolgersi del lavoro e per il supporto fornitomi nei momenti di difficoltà.

Il percorso di studi svolto presso l'Università di Trieste è stato appassionante ed intenso: desidero quindi volgere un pensiero di gratitudine anche a tutti i docenti che ho conosciuto in questi anni. In particolare, ringrazio i Professori Renata Longo e Gianrossano Giannini per la premura e l'appoggio con cui mi hanno sostenuta nella scelta che ha portato alla realizzazione di questa tesi. Oltre a loro ringrazio il Professor Francesco Longo, sono grata per i loro preziosi consigli per l'attenzione *con cui mi hanno ascoltata. Sono stati dei punti di riferimento per il mio percorso universitario e spero lo saranno anche in futuro.*

Intendo inoltre esprimere la mia gratitudine alla Dottoressa Silvana Palmiero, per la professionalità, l'impegno e la disponibilità con cui ha gestito le pratiche necessarie per l'avvio ed il compimento di questo progetto di tesi.

Ringrazio di cuore la mia famiglia, in particolare i miei genitori, che mi hanno sempre sostenuta in tutte le mie scelte. Li ringrazio per i loro insegnamenti, per lo sguardo che mi hanno aperto sul mondo: sono stati il mio riferimento e la mia guida. Un grazie speciale a mio papà, mia spalla e mio confidente. In lui ho trovato la forza di affrontare con determinazione ogni ostacolo e la serenità per non mollare mai. Grazie a mia mamma, perché è il mio orgoglio e il mio modello. Lei mi ha formato come persona e come donna, trasmettendomi i valori della sensibilità e del rispetto. Grazie anche a mio fratello, Silvio, mia controparte e mio complice. Nonostante la sua irruenza, mi dimostra continuamente il suo affetto, riportandomi sempre il sorriso.

Un dolce pensiero va a mi abuela Lucila, di cui sento tremendamente la mancanza. Sarebbe stata orgogliosa di questo traguardo.

Grazie a Edoardo, per l'amore che mi dimostra e per la grinta con cui mi sostiene in ogni decisione. Nonostante le iniziali difficoltà, non ha mai smesso di spronarmi a seguire i miei desideri nella scelta dell'argomento di tesi, e per questo gli sono riconoscente. A lui va tutto il mio amore e la gratitudine di averlo al mio fianco.

Grazie, infine, a tutti i miei amici. Nonostante la distanza mi sono sempre stati vicino, aiutandomi ad affrontare con gioia e tenacia anche l'ultimo tratto del mio percorso universitario.